NASA Technical Memorandum 103926

The Three-Dimensional Evolution of a Plane Mixing Layer Part 2. Pairing and Transition to Turbulence

Robert D. Moser and Michael M. Rogers

December 1992

National Aeronautics and Space Administration

NASA Technical Memorandum 103926

The Three-Dimensional Evolution of a Plane Mixing Layer Part 2. Pairing and Transition to Turbulence

Robert D. Moser and Michael M. Rogers, Ames Research Center, Moffett Field, California

December 1992

National Aeronautics and
Space Administration

Ames Research Center
Moffett Field, California 94035-1000

CONTENTS

SUMMARY

The evolution of three-dimensional temporally evolving plane mixing layers through as many as three pairings has been simulated numerically. Initial conditions for all simulations consisted of a few low-wavenumber disturbances, usually derived from linear stability theory, in addition to the mean velocity. Three-dimensional perturbations were used with amplitudes ranging from infinitesimal to large enough to trigger a rapid transition to turbulence. Pairing is found both to inhibit the growth of infinitesimal three-dimensional disturbances and to trigger the transition to turbulence in highly three-dimensional flows. The mechanisms responsible for the growth of three-dimensionality as well as the initial phases of the transition to turbulence are described. The transition to turbulence is accompanied by the formation of thin sheets of spanwise vorticity, which undergo a secondary roll-up. Transition also produces an increase in the degree of scalar mixing, in agreement with experimental observations of mixing transition.

Simulations were also conducted to investigate changes in spanwise length scale that may occur in response to the change in streamwise length scale during a pairing. The linear mechanism for this process was found to be very slow, requiring roughly three pairings to complete a doubling of the spanwise scale. Stronger three-dimensionality can produce more rapid scale changes but is also likely to trigger transition to turbulence. No evidence was found for a change from an organized array of rib vortices at one spanwise scale to a similar array at a larger spanwise scale.

1 INTRODUCTION

Free shear layers are of great technological importance because they occur in many practical devices, especially those involving chemical reactions. However, a thorough understanding of the hydrodynamics of free shear flows is a prerequisite to understanding the physical processes involved in such chemically reacting systems. In Rogers and Moser (1991) (hereafter referred to as Part 1) and in this paper, we attempt to develop such an understanding in the case of the simplest free shear flow, the plane mixing layer. Although this flow has been extensively studied by analytical, numerical, and experimental means, many questions remain unanswered. In particular, not enough is known about the development of three-dimensionality and the transition to turbulence. Here numerically simulated, temporally evolving free shear layers that undergo up to three pairings of the primary Kelvin-Helmholtz rollers are examined to study these issues.

1.1 Pairing

Brown and Roshko (1971, 1974) observed that their experimental plane mixing layers developed and maintained a remarkable degree of spanwise coherence. Their flow visualizations indicated that even a turbulent mixing layer is dominated by the presence of quasi-two-dimensional, large-scale spanwise rollers that span the entire experimental test section. This observation is counter to the classical picture of fully turbulent flows, and its general validity was questioned. Chandrsuda et al. (1978) argued that, in engineering applications, the presence of strong free-stream disturbances or turbulent splitter-plate boundary layers would make the layer more incoherent. They presented smoke visualizations that seemed to indicate a helical structure, perhaps the result of localized pairing of the Kelvin-Helmholtz

rollers. Further investigations by others, however, supported the conclusion that the mixing layer is largely two-dimensional, even when strong disturbances are present. Wygnanski et al. (1979) examined the evolution of several strongly perturbed mixing layers. They concluded that strong free-stream turbulence and turbulent splitter-plate boundary layers do not destroy the two-dimensional character of the layer. They predicted that the apparently three-dimensional flow of Chandrsuda et al. would actually become more two-dimensional further downstream. The dominance of the two-dimensional structures persists even in experiments in which the splitter-plate geometry is modified (e.g., Breidenthal, 1980; and Lasheras, Cho, and Maxworthy, 1986).

The results of Winant and Browand (1974) suggest that the primary growth in layer thickness occurs through pairing of the two-dimensional structures, at least at the relatively low Reynolds numbers of their experiments. This pairing process consists of the corotation and eventual amalgamation of adjacent spanwise vortices and was found to occur several times during the downstream evolution of the layer. Pairing has since been observed in a variety of experimental and numerical studies of mixing layers, including in the experiments of Dimotakis and Brown (1976) at much higher Reynolds numbers. However, not all investigators agree that pairing is primarily responsible for the layer growth. Hernan and Jimenez (1982) concluded that most of the layer growth occurred during the period between pairings. In addition, an alternate mechanism for vortex amalgamation has been found. This mechanism, similar to that predicted by Moore and Saffman (1975), is referred to as "tearing" or "shredding" and is characterized by the tearing apart of a spanwise vortex by its neighboring vortices. Experiments in which forcing is used (Yang and Karlsson, 1991) and numerical simulations (e.g., Riley and Metcalfe, 1980) have shown that this tearing occurs for a narrow range of relative phasings of the fundamental and subharmonic disturbances. Such tearings are infrequent and occur slowly compared to the more usual pairing amalgamation (Hernan and Jimenez, 1982). Pairing interactions can also involve more than two spanwise vortices, with "triplings" occurring about as often as tearings (Hernan and Jimenez, 1982). Both triplings and quadruplings were observed by Brown and Roshko (1974), and by using forcing at various frequencies, pairing interactions involving up to ten vortices have been observed (Ho and Huang, 1982).

1.2 Three-Dimensionality

Flow visualizations of mixing layers have revealed the presence of streamwise vortex structures in the braid regions between successive spanwise rollers (Brown and Roshko, 1974; Konrad, 1976; Bernal, 1981; Breidenthal, 1981; Jimenez, 1983). End views through the braid region of the kind shown in Bernal and Roshko (1986) indicate that these are counterrotating pairs of streamwise vortices and that they span the braid region between the low-speed side of one spanwise vortex and the high-speed side of its downstream neighbor. These vortices are associated with a "wiggle," or corrugation, of the spanwise vortices (Breidenthal, 1981). During the early evolution of the layer, not all these streamwise vortices are found in counterrotating pairs; their initial locations are related to small upstream disturbances (Jimenez, 1983; Lasheras, Cho, and Maxworthy, 1986). However, like-sign neighbors soon pair, resulting in a "stable configuration" of counterrotating vortices of similar strength (Lasheras, Cho, and Maxworthy, 1986; Bell and Mehta, 1989). The early evolution of these "rib" vortices during the initial Kelvin-Helmholtz roll-up of the mixing layer was the primary focus of Part 1.

The spanwise scale of the streamwise vortices is highly variable. Stability calculations by Pierrehumbert and Widnall (1982) show that the most amplified spanwise wavelength associated with a periodic array of Stuart (1967) vortices is about two-thirds of the fundamental disturbance wavelength, but that disturbances with considerably longer and shorter wavelengths have nearly the same growth rate. Corcos and Lin (1984) confirmed this insensitivity to spanwise scale for the more realistic case of an evolving two-dimensional base flow. Lasheras and Choi (1988) found no appreciable difference in growth rate for disturbances between one-fifth and three times the fundamental wavelength in their experiments using serrated splitter-plate trailing edges. Despite this broad range of possible spanwise wavelengths, most "naturally evolving" mixing layers seem to have a characteristic spanwise scale that is close to that predicted by Pierrehumbert and Widnall (1982).

There is, however, a considerable difference of opinion regarding changes in spanwise scale that may occur as a result of the streamwise scale changes that take place during pairings. Flow visualizations by Bernal and Roshko (1986) indicate that their spacing remains constant through several pairings until the completion of the so-called "mixing transition." A three-dimensional reconstruction of a pairing event by Jimenez, Cogollos, and Bernal (1985) indicates that the number of streamwise vortices is halved after a pairing. Jimenez (1983) postulated a mechanism for this scale change in which neighboring ribs annihilate each other, leaving ribs at twice the original spanwise scale but with the same circulation as before. Similarly, Huang and Ho (1990) find in their experiments that the preferred spanwise scale doubles after both the first and second pairings.

1.3 Mixing Transition

At a certain point in the evolution of the mixing layer, the amount of mixing that occurs within the layer increases substantially, particularly for high Schmidt numbers (Konrad, 1976; Breidenthal, 1981). This has been termed the "mixing transition" and is associated with the formation of small-scale eddies, or turbulence. Koochesfahani and Dimotakis (1986) used laser-induced fluorescence (LIF) to visualize the structure within the layer both before and after the transition. The increased flow complexity after the transition is readily apparent, as is the significant increase in amount of mixed fluid. In their experiment, this transition occurred between Reynolds numbers of 5600 and 17,000, where this Reynolds number is based on the velocity difference and the local visual thickness of the layer.

Huang and Ho (1990) correlate transition with the occurrence of pairings rather than with local Reynolds number. By scaling the downstream distance with the ratio $\Delta U/\overline{U}$ and the fundamental disturbance wavelength λ_x, they collapse data for various velocity ratios and find that transition in their experiments is largely completed by the second pairing. In flows at lower Reynolds numbers, this transition may be delayed until later pairings take place. The data of Huang and Ho (1990) are consistent with observations of Winant and Browand (1974), who noted a "considerable increase in smaller scale fluctuations at about the time of the second pairing."

Several investigators have speculated that the onset of mixing transition is related to the presence of the streamwise vortices discussed above. Lin and Corcos (1984) suggest that it was the "collapse" of the streamwise vorticity into compact, streamwise vortices of the type visualized in experiments that was responsible for at least the onset of mixing transition. On the other hand, Lasheras, Cho, and Maxworthy (1986) felt that a higher-order instability was required to explain the marked increase in

mixing associated with the mixing transition. In recent numerical simulations, Moser and Rogers (1991) identified a mechanism by which pairing initiates a transition to turbulence.

1.4 Unanswered Questions

Although the pairing of three-dimensional mixing layers has been studied by many researchers, there are many important, unanswered questions. Those addressed by the current study are described below. The results of Rogers and Moser (1991) suggest that if oversaturation is prevented, as is the case in pairing mixing layers, then the instability responsible for the growth of three-dimensionality may be different from the "translative" instability described by Pierrehumbert and Widnall (1982) and discussed further by Corcos and Lin (1984). The long-term growth of three-dimensionality through several pairings has not been investigated, and the character of the three-dimensional instability has not been determined. Further, previous studies have not addressed the way in which such an instability might ultimately lead to a transition to turbulence. Neither the mechanism by which spanwise scale changes (section 1.2) might occur nor the set of conditions under which they would occur has been examined. Finally, the helical pairing discussed by Chandrsuda et al. (1978) and Pierrehumbert and Widnall (1982) has not been carefully studied.

In this study, we use direct numerical simulations of mixing layers to address these issues because they allow precise definition of the initial (or inlet) conditions and provide a complete description of the velocity and vorticity fields at any time. For a variety of reasons, previous numerical simulations (see section 1.3 of Part 1 for a brief discussion of previous simulations) were unable to address the issues discussed here. Most significantly, none of the previous computations has approached the scale or Reynolds number of the three-dimensional multiple-pairing cases presented here (visual-thickness Reynolds numbers up to 10,000 have been simulated). The combination of higher Reynolds numbers and multiple pairings permits us to simulate a "naturally occurring" transition to turbulence, whereas other researchers have used random fluctuations in their initial conditions to produce a "turbulent" layer. Our method permits comparison with, and analysis of, the small-scale transition observed in experiments begun from laminar splitter-plate boundary layers.

Some of the discussion in the following sections relies on results from the first portion of this study (Part 1), which deals with the roll-up of three-dimensional mixing layers. A review of the necessary material appears in the Appendix. Also, a brief description of the small-scale transition discussed here appeared in Moser and Rogers (1991).

In section 2, background information on the numerical simulations used in this study is presented. Linear stability of the pairing two-dimensional mixing layer is discussed in section 4, and nonlinear evolutions of flows undergoing one and two pairings are presented in sections 5 and 6, respectively. Spanwise-scale-change mechanisms are discussed in section 7, and the characteristics of the post-transitional "turbulent" flows are described in section 8. Finally, helical pairing is discussed in section 9 and a summary is given in section 10.

Much of this work was begun in collaboration with visiting scientists at the 1988 Center for Turbulence Research Summer School Program. In particular, we are grateful for discussions with Professors C.-M. Ho, F. Hussain, and J. Riley. In addition, we have benefited from comparisons

with the spatially developing mixing-layer work of Dr. J. Buell, the compressible-shear-layer work of Prof. S. K. Lele, and from Prof. E. Broadwell's vast experience with experimental mixing layers. Helpful comments provided by Dr. N. Mansour and Prof. S. K. Lele on a draft of this paper are also appreciated. Some of the computations were performed on the NAS supercomputers at NASA Ames Research Center.

2 PRELIMINARIES

The primary tool used in this study is direct numerical simulation of the time-developing mixing layer. The time-developing mixing layer may be thought of as an approximation to the evolution of a single set of flow structures as they are convected downstream in the more common spatially developing layer. The roles of time and the streamwise spatial direction are thus reversed. As the velocity ratio of the spatial layer approaches one, this approximation becomes exact (Buell, Moser, and Rogers, 1992). Also, comparisons of spatially and temporally evolving simulations indicate that the same dynamical mechanisms occur in both cases for velocity ratios even as low as 0.2 (Buell et al., 1992). It is thus expected that results presented here will be relevant to spatially developing mixing layers. A time-developing formulation was used in this study because its computational simplicity permits the simulation of higher Reynolds numbers and smaller scales. Although only an approximation to a spatially developing mixing layer, the temporally evolving layer is also of interest as a good model of geophysical mixing layers that form in the absence of a splitter plate (Turner, 1973) as well as of the stratified tilting-tank experiments of Thorpe (1968, 1971, 1973, 1985).

All the simulations described here were initialized with simple, "clean" initial conditions (see section 2.2). It is expected that a thorough understanding of the vortex dynamics of such "clean" flows will enable one to understand the development of mixing layers in the more general case of uncontrolled disturbances. These flows may be considered to be "deterministic models" of the development of mixing layers, in the same sense as flows considered in the work of Corcos and Sherman (1984), Corcos and Lin (1984), and Lin and Corcos (1984). The initial conditions were chosen to have relatively short spanwise wavelengths to reproduce the "standard" structures of ribs and rollers, rather than long-spanwise-wavelength phenomena such as dislocations (Browand and Troutt, 1980, 1985) and slow spanwise variations of the mean profile (Rogers et al., 1988).

2.1 The Governing Equations and Numerical Considerations

The simulations reported here were performed by solving the vorticity equation derived from the incompressible Navier-Stokes equations:

$$\frac{\partial \boldsymbol{\omega}}{\partial t} + \nabla \times (\boldsymbol{\omega} \times \mathbf{U}) = \frac{1}{Re_0} \nabla^2 \boldsymbol{\omega} \tag{1}$$

where $\mathbf{U}(x, y, z, t)$ is the velocity vector (with components u, v, and w), and $\boldsymbol{\omega} \equiv \nabla \times \mathbf{U}$ is the vorticity vector. Here, U (the half velocity difference) and δ_ω^0 (the initial vorticity thickness of the layer, see equation 4) have been used to nondimensionalize the equations and form the Reynolds number $Re_0 = U\delta_\omega^0/\nu$ (ν is the kinematic viscosity). This nondimensionalization is used throughout this paper.

In addition, the evolution of a passive scalar T is computed using the scalar equation

$$\frac{\partial T}{\partial t} + \mathbf{U} \cdot \nabla T = \frac{1}{Pe_0} \nabla^2 T \tag{2}$$

where the Peclet number is given by $Pe_0 = Re_0 Sc$ and the Schmidt number is $Sc = \nu/\gamma$ (γ being the molecular diffusivity of the scalar).

Equations (1) and (2) are solved using periodic boundary conditions with periods L_x and L_z in the streamwise (x) and spanwise (z) spatial directions.[1] In the cross-stream (y) direction, ω and $T - \overline{T}$ ($\overline{T}$ being the average mean scalar profile) go to zero as $y \to \pm\infty$. The x- and z-dependence of the independent variables are represented by finite Fourier series, and the y-dependence is represented by a polynomial expansion in the mapped variable $\eta = \tanh(y/y_0)$, where y_0 is a mapping parameter (usually set to be on the order of the final layer thickness). In addition, the y-dependence of the velocity $\mathbf{U}$ is represented using special expansion functions that exactly represent the slow decay of velocity perturbations far from the layer. The computational method was developed specifically for the simulation of three-dimensional free shear layers. It is a spectral Galerkin method and exhibits "infinite-order" accuracy of the spatial discretization. A detailed description of the method can be found in Spalart, Moser, and Rogers (1991). The equations were advanced in time using a compact, third-order Runge-Kutta scheme of the form proposed by Wray (personal communication, see Spalart, Moser, and Rogers, 1991, for details). The Galerkin quadratures involving the nonlinear terms are computed using Gauss quadrature with sufficient points to eliminate aliasing errors. As many as $192 \times 212 \times 128$ Fourier/Jacobi modes (see Spalart et al., 1991) and 380 hours on a Cray Y-MP were required to simulate the turbulent flows described in section 8 (e.g., TURB2P).

2.2 Specification of Initial Conditions

The self-similar solution for the streamwise velocity profile of the laminar, temporally evolving plane mixing layer is a viscously spreading error function. Thus, an error function,

$$\overline{U} = U \mathrm{erf}(\sqrt{\pi} y/\delta_\omega^0) \tag{3}$$

is used for the initial mean streamwise velocity profile in the simulations discussed here. Note that this profile has a vorticity thickness

$$\delta_\omega \equiv \frac{2U}{(\partial \overline{U}/\partial y)|_{\max}} \tag{4}$$

of δ_ω^0. The initial mean passive scalar profile is given by

$$\overline{T} = \frac{1}{2}(1 + \mathrm{erf}(\sqrt{\pi} y/\delta_\omega^0)) \tag{5}$$

The magnitude of the scalar is arbitrary because equation (2) is linear in T.

In addition to the mean velocity, simple perturbations are included in the initial conditions. These perturbations include just one or a few of the x- and z-Fourier modes of the representation. Streamwise

[1] Note that spanwise periodicity precludes the possibility of studying end-wall effects (i.e., side-wall boundary layers, etc.).

and spanwise fundamental wavelengths (λ_x and λ_z) are chosen as the most unstable wavelengths from linear theory ($\lambda_x = 2.32\pi$, see Monkewitz and Huerre (1982); and $\lambda_z = 0.6\lambda_x$, see section 4.2), and perturbations with these wavelengths and their subharmonics are used in the initial conditions. To accommodate these perturbations, the computational domain must be an integer multiple of the wavelengths in the x- and z-directions. Thus, in general, $L_x = N\lambda_x$ and $L_z = M\lambda_z$. N and M are as large as 8 for cases reported here, to accommodate the subharmonic disturbances.

To specify the initial conditions and facilitate discussion throughout this paper, it is necessary to refer to specific wavenumbers; they will be referred to in ordered pairs

$$(\alpha, \beta) = \left(\frac{k_x \lambda_x}{2\pi}, \frac{k_z \lambda_z}{2\pi} \right) \tag{6}$$

where k_x and k_z are the x and z wavenumbers, respectively. Thus the fundamental modes discussed above have α and/or β equal to one. In general the simulations include wavenumbers with $\alpha = \pm j/N$ for $j = 0, 1, 2, \ldots (N_x - 2)/2$ and $\beta = \pm l/M$ for $l = 0, 1, 2, \ldots (N_z - 2)/2$, where N_x and N_z are the (even) number of Fourier modes in the x- and z-directions, respectively. Note that, because the quantities under consideration are real, the Fourier coefficients of the (α, β) and the $(-\alpha, -\beta)$ modes are complex conjugates (denoted by †). Thus only modes with $\alpha \geq 0$ are considered here.

The amplitude of a given Fourier mode (of an initial perturbation or in the evolved field) can be measured by the integrated (in y) rms velocity of the mode. Thus we define

$$A_{\alpha\beta} = \begin{cases} \sqrt{\int_{-\infty}^{+\infty} 2\hat{u}_i(\alpha,\beta)\hat{u}_i^\dagger(\alpha,\beta)\, dy} & \text{if } \alpha = 0 \text{ or } \beta = 0; \\ \sqrt{\int_{-\infty}^{+\infty} 2[\hat{u}_i(\alpha,\beta)\hat{u}_i^\dagger(\alpha,\beta) + \hat{u}_i(\alpha,-\beta)\hat{u}_i^\dagger(\alpha,-\beta)]\, dy} & \text{otherwise} \end{cases} \tag{7}$$

Here $\hat{u}_i(\alpha, \beta)$ is the (α, β) Fourier coefficient of the velocity component u_i. Note that $A_{\alpha\beta}$ is only defined for nonnegative α and β since it includes the contributions of all the $(\pm\alpha, \pm\beta)$ modes. The amplitude associated with all modes with a particular spanwise wavenumber and the amplitude of all three-dimensional Fourier modes ($\beta \neq 0$) are also of interest. They are denoted by $A_{s\beta}$ and A_{3D}, respectively,[2] and are defined

$$A_{s\beta} = \sqrt{\sum_{J=0}^{N_x/2-1} (A_{J\beta})^2} \tag{8}$$

$$A_{3D} = \sqrt{\sum_{J=1}^{N_z/2-1} (A_{sJ})^2} \tag{9}$$

Note that, as a special case, A_{s0} is the amplitude associated with all two-dimensional modes. Throughout this paper, $A_{\alpha\beta}$, $A_{s\beta}$, and A_{3D} are quoted normalized by $U\sqrt{\delta_\omega^0}$. A superscript 0 (e.g., $A_{\alpha\beta}^0$) will be used to denote the amplitude at $t = 0$, and a superscript $*$ will indicate the amplitude normalized by its value at $t = 0$ (e.g., $A_{\alpha\beta}^* = A_{\alpha\beta}/A_{\alpha\beta}^0$).

[2]The subscript s signifies a sum over streamwise wavenumbers α.

All the simulations reported here were initialized with two-dimensional spanwise vorticity perturbations, which lead to the Kelvin-Helmholtz roll-up and subsequent pairings of the mixing layer. The spanwise vorticity perturbation has the form

$$\omega_z = \sum_{\alpha=1,\frac{1}{2},\frac{1}{4}\ldots} A^0_{\alpha 0}\, \mathcal{R}\left(f_\alpha(y) e^{i(k_x x - \phi_{\alpha 0})}\right) \tag{10}$$

where $\mathcal{R}$ signifies the real part of a complex argument. In most cases the complex functions $f_\alpha(y)$ are the stability eigenfunctions for the vorticity, determined from the Orr-Sommerfeld equation for that wavenumber (referred to as viscous eigenfunction, or VE). Each eigenfunction is normalized such that its integrated energy is one, its real part is symmetric in y (and positive at $y = 0$), and its imaginary part is antisymmetric. In some cases $f_\alpha(y)$ was chosen to be a Gaussian ($f_\alpha(y) = c_\alpha e^{-\pi y^2}$, where c_α is a normalization constant chosen such that the integrated energy in the $(\alpha, 0)$ mode is unity when $A_{\alpha 0}$ is one), which is referred to as an ω-Gaussian initial condition (ωG). The phase ϕ_{10} is irrelevant to the evolution of the flow and is set to zero for convenience. The phases $\phi_{\alpha 0}$ of the subharmonics ($\alpha = \frac{1}{2}, \frac{1}{4}$, etc.) relative to the fundamental ($\alpha = 1$) determine whether large-scale amalgamations occur by pairing or tearing (see Riley and Metcalfe, 1980; Monkewitz, 1988). In all cases the optimum pairing phase ($\phi_{\alpha 0} = 0$) was selected. The amplitudes $A^0_{\alpha 0}$ vary depending on α and the case being considered. They are reported for each case in the relevant sections.

As in Part 1, three-dimensionality was usually introduced in the simulations by including initial perturbations in the $(0, \pm\beta)$ modes. These are referred to as streamwise invariant (STI) disturbances. For these modes, only the streamwise vorticity component is made nonzero and the following functional form is used:

$$\omega_x = \sum_{\beta=1,\frac{1}{2}\frac{1}{4}\ldots} A^0_{0\beta}\, g_\beta(y) \sin(k_z z - \phi_{0\beta}) \tag{11}$$

The function $g_\beta(y)$ is either an ωG disturbance ($g_\beta(y) = c_\beta e^{-\pi y^2}$) or is such that the vertical velocity v is a Gaussian (v-Gaussian or vG disturbance, $g_\beta(y) = c_\beta(4y^2 - 2 - k_z^2)e^{-y^2}/k_z$). In either case, c_β is a normalization constant selected such that the integrated energy in the $(0, \beta)$ mode is unity when $A_{0\beta}$ is one. An eigenfunction is not used for this mode because there are no eigenfunctions satisfying the boundary conditions. The phase ϕ_{01} is irrelevant to the flow evolution and for convenience is set to zero. The subharmonic phases *are* important, and the effect of varying them is discussed in section 7.

These initial conditions were selected largely because they lead to structures of the type commonly observed in experimental spatially developing mixing layers (see Part 1). They are also representative of the types of disturbances expected to be present in experimental mixing layers. The two-dimensional roll-up disturbance is likely to arise in an experimental apparatus due to the trailing edge of the splitter plate (see section 4.2 of Ho and Huerre, 1984). Streamwise vortices are also expected, because wind-tunnel imperfections introduce such vortices into the splitter-plate boundary layers (e.g., Jimenez, 1983). In Part 1 it was shown that the flow evolution resulting from the STI disturbances used here is typical of the evolutions resulting from a variety of other three-dimensional disturbances.

The simulations described in section 9 were begun from initial three-dimensional perturbations in oblique Fourier modes rather than in the STI modes described above. Details of the initialization for these flows are given in section 9.

2.3 Flow Symmetries

In some cases, the initial conditions (described by eqs. (10) and (11) in section 2.2) possess two spatial symmetries that are preserved by the Navier-Stokes equations. Whether or not these symmetries exist depends on the spanwise subharmonics and their phases ($\phi_{0\beta}$). One possible symmetry is a z-plane reflection symmetry,

$$\begin{aligned} \omega_i(x,y,z) &= -\omega_i(x,y,-z+2z_s) \quad \text{where } i \text{ denotes } x \text{ or } y \text{ and} \\ \omega_z(x,y,z) &= \omega_z(x,y,-z+2z_s) \end{aligned} \tag{12}$$

where $z = z_s$ is a symmetry plane. If this symmetry exists, there are two such symmetry planes in the domain, located at $z = 0$ and $z = L_z/2$ for the initial condition in equation (11). Note that both ω_x and ω_y are zero in these symmetry planes. The other possible symmetry is a point-reflection symmetry,

$$\omega_i(x,y,z) = \omega_i(-x+2x_s,-y,-z+2z_s) \tag{13}$$

where $(x,y,z) = (x_s,0,z_s)$ is a symmetry point. If this symmetry is present, there are four such symmetry points in the domain, located at $(0,0,\frac{\lambda_z}{4})$, $(0,0,\frac{L_z}{2}+\lambda_z/4)$, $(\frac{L_x}{2},0,\frac{\lambda_z}{4})$, and $(\frac{L_x}{2},0,\frac{L_z}{2}+\lambda_z/4)$ for the values of $\phi_{\alpha 0}$ and $\phi_{0\beta}$ used in equations (10) and (11).

These symmetry planes and points provide well-defined reference locations in the flow. The Kelvin-Helmholtz roller that remains after all pairings are complete is centered at $x = L_x/2$ (for $\phi_{\alpha 0} = 0$), the x-location of two of the symmetry points. The braid regions between the final roller and its periodic images are centered on the other symmetry points at $x = 0$ (and by periodicity at $x = L_x$). The rib vortices that form in the surviving braid region (see Part 1) are centered on the $x = 0$ symmetry points.

The reference locations described above can be used to define three special planes that will be used to view the simulated flow fields (see fig. 1 of Part 1). Two are x–y planes: the between-ribs plane (BP) and the rib plane (RP). The between-ribs planes are coincident with the planes of symmetry at $z = 0$ and $z = L_z/2$ and are always located between a pair of ribs. The rib planes at $z = \lambda_z/4$ and $(L_z/2) + \lambda_z/4$ pass through the ribs (halfway between the BP's when $L_z = \lambda_z$) and contain the symmetry points. Note that the BP is not well defined if the plane symmetry (eq. (12)) is broken and that the RP is not well defined if the point symmetry (eq. (13)) is broken. The other plane used here (the mid-braid plane, or MP) is the z–y plane through the middle of the surviving braid region. Thus for the disturbances used here, the MP is located at $x = 0$ (and $x = L_x$ by periodicity). If the point-reflection symmetry exists, the MP contains two of the symmetry points.

The presence of these symmetries in the flows considered here simplifies the analysis of the simulations by allowing unambiguous definitions of the special planes discussed above as well as other items (e.g., rib circulation and rib vortex lines). Of course, laboratory mixing layers do not possess these symmetries; therefore, flows that break one or both of the symmetries have been simulated to confirm that the insights gained from these idealized symmetric cases are valid in general. Indeed, flows without these symmetries evolve qualitatively as the typical symmetric flows do (see sections 7–9 and Part 1).

3 TWO-DIMENSIONAL PAIRINGS

To determine how a three-dimensional mixing layer departs from its two-dimensional counterpart, it is necessary to consider two-dimensional flows as a basis for comparison. In addition to determining the amount of "three-dimensionality" present in the three-dimensional flows, such simulations also enable one to study important phenomena that are essentially two-dimensional. The Kelvin-Helmholtz roll-up of spanwise vorticity into rollers, the pairing of these rollers, and the depletion of spanwise vorticity from (and subsequent reentry into) the braid region are examples of two-dimensional phenomena that are relevant to three-dimensional flows. Two-dimensional simulations also provide a quick way to determine the effects of varying the two-dimensional parameters (at least while the three-dimensional disturbances are relatively weak). Changes brought about by varying the Reynolds number are described in section 3.2. The effects of varying other two-dimensional parameters (e.g., wavelength and form of the two-dimensional disturbances) are discussed in Part 1. Finally, the two-dimensional flows also serve as the base flows for the three-dimensional, time-dependent linear perturbation analysis presented in section 4. A list of the two-dimensional simulations for which data are presented is given in table 1.

3.1 Time Evolution

Contours of the spanwise vorticity at various times for a two-dimensional, single-pairing case (2D1P) are shown in figure 1. Initially the vorticity rolls up, as described in Part 1. By $t = 11$, the rollers are well developed and are beginning to pair. Both the number of rollers and the number of braid regions are halved by this pairing process, the contents of every other braid region being absorbed into the new paired roller. The surviving braid region continues to be depleted of spanwise vorticity as all the vortical fluid is drawn into the paired roller. As the cores of the original spanwise rollers merge into a new, roughly circular core, spiral arms of weaker spanwise vorticity are ejected from the paired eddy.[3] The tips of these spiral arms develop a characteristic hook shape and are eventually drawn back into the surviving braid region between the paired eddy and its periodic images.

The evolution of the amplitude of the fundamental and subharmonic two-dimensional disturbances in 2D1P is depicted in figure 2. Both modes undergo periods of exponential growth at early times. As in Part 1, the first maximum of A_{10} in time is taken to define the "roll-up time," τ_r. Analogously, the first maximum of the subharmonic amplitude ($A_{\frac{1}{2}0}$) is taken to be the "first pairing time," τ_{p1}, which is 21.5 for this case. It should be noted that the presence of energy in subharmonic modes may alter the energy development of the fundamental mode and thus change τ_r somewhat. It can be seen from figure 1(c) that at τ_{p1} the paired eddy is largely vertical with a short streamwise extent. At this point, the original vortex cores have corotated by about 120°. Note that Ho and Huang (1982) define the pairing location in their spatially developing layer similarly, except that only the u-component is used to determine the mode amplitude. By this definition the pairing time occurs sooner, consistent with Ho and Huang's observation that the vortex cores have rotated by only 90° at the pairing time.

During the pairing, A_{10} undergoes several oscillations. Examination of figures 1(b)–1(d) (times corresponding to the first minimum, second maximum, and second minimum in A_{10}, respectively) reveals that A_{10} is minimum when sharp interfaces in ω_z are largely horizontal and is maximum when

[3]This is required by energy conservation; Martel, Mora, and Jimenez (1989).

Table 1. Parameters of the two-dimensional simulations. Disturbance profiles are VE, $\phi_{\alpha 0} = 0$, $Pr = 1.0$, and $\lambda_x = 1.16(2\pi)$ for all cases. 2D3P was not run long enough to determine τ_{o3}, and four of the last five simulations were not run long enough to determine τ_{o1}.

Simulation	Re_0	A_{10} $\times 10^2$	$A_{\frac{1}{2}0}$ $\times 10^2$	$A_{\frac{1}{4}0}$ $\times 10^2$	$A_{\frac{1}{8}0}$ $\times 10^2$	τ_r	τ_{o0}	τ_{p1}	τ_{s1}	τ_{o1}	τ_{p2}	τ_{s2}	τ_{o2}	τ_{p3}	τ_{s3}
2D0P	250	4.00				13.4	17.5								
2D1P	250	4.00	3.00			11.9		21.5	29.2	46.5					
2D2P	250	4.00	3.00	3.00		11.9		21.5	31.2		46.7	63.9	90.3		
2D3P	250	4.00	3.00	3.00	3.00	11.9		21.5	32.0		47.0	66.7		103.7	139.8
2D1PDEL	250	4.00	1.00			13.1	20.0	26.4	34.4						
2D1P100	100	10.00	5.00			9.4		20.4	28.1						
2D1P250	250	10.00	5.00			9.5		20.1	27.7						
2D1P500	500	10.00	5.00			9.5		20.0	27.7						
2D1P1000	1000	10.00	5.00			9.4		19.9	27.6	46.3					

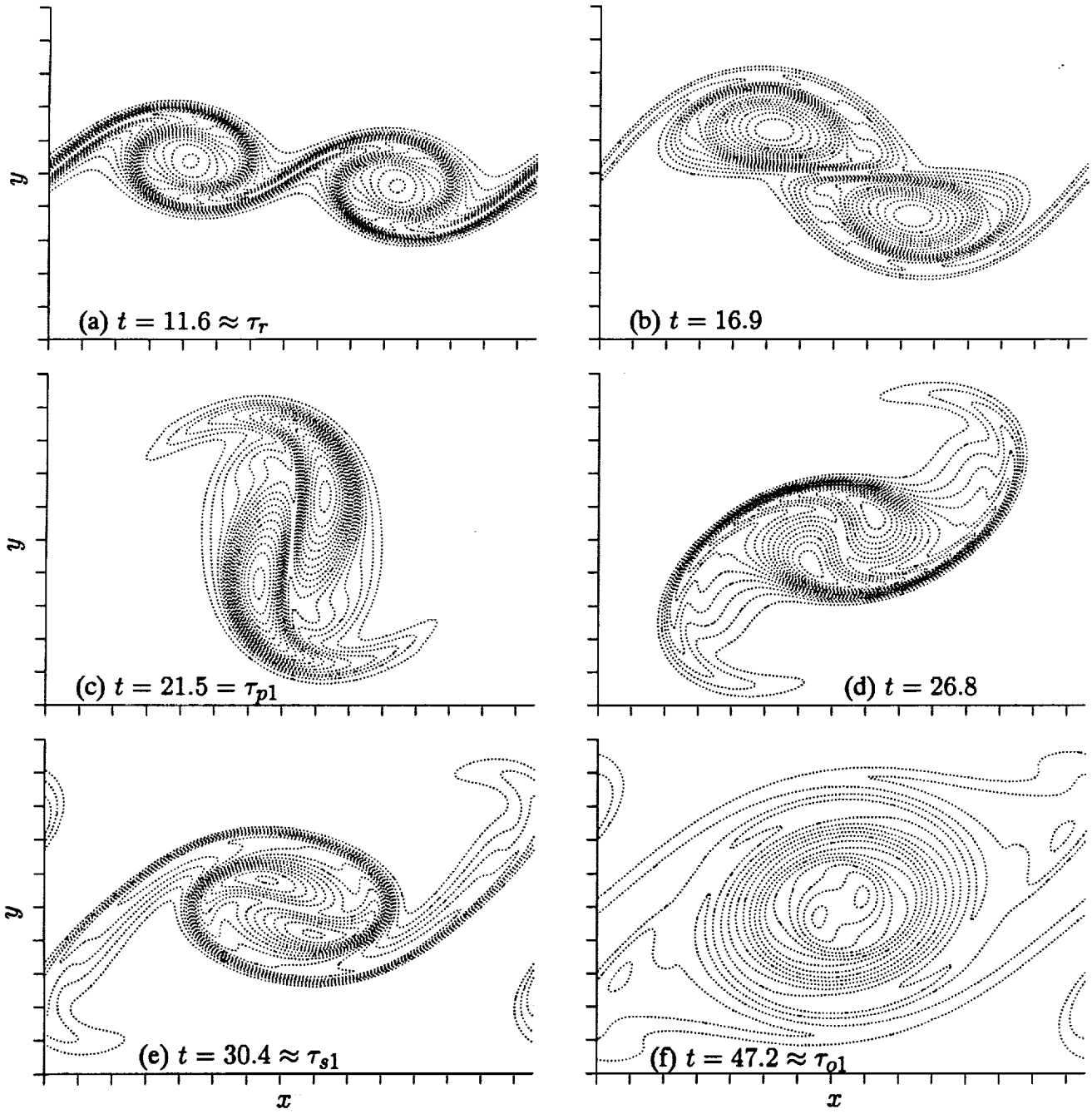

Figure 1. Contours of ω_z from 2D1P. The contour increment is -0.1 (in (f) there is an extra contour at -0.05 to show the elliptical shape of the roller), and the contours are dotted to indicate negative spanwise vorticity. Tic marks are at δ_ω^0 increments.

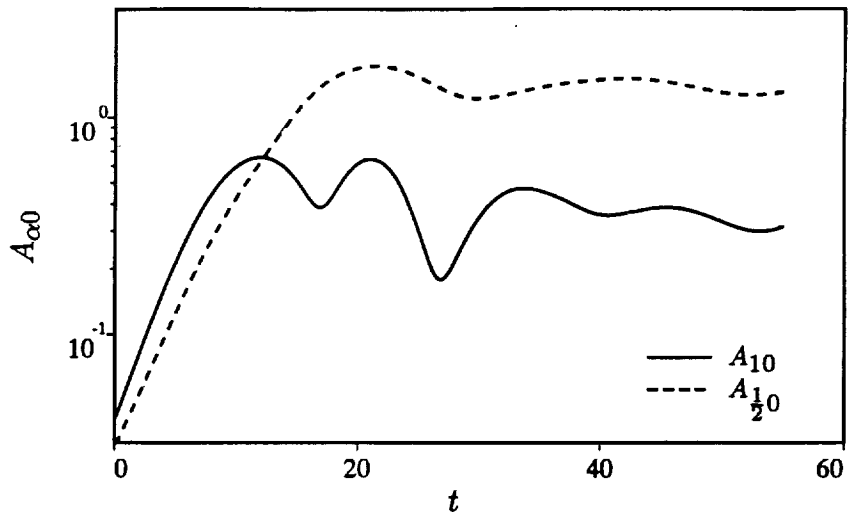

Figure 2. Time development of two-dimensional disturbance amplitudes for 2D1P.

these interfaces are vertical.[4] Thus this oscillation is related to the rotation of the paired rollers and the associated interfaces. In addition, the thickness of the layer (measured by δ_m) has a local maximum near τ_p (see fig. 3(c)) when the vertical extent of the pairing rollers is the largest (see fig. 5).

In the single roll-up cases discussed in Part 1, the roller cores eventually became elliptical, and spanwise vorticity was advected into the braid region (oversaturation). This does not occur after the roll-up in 2D1P because the pairing begins before oversaturation occurs. After the pairing, however, the spiral arms of spanwise vorticity that are ejected from the paired roller are drawn into the braid region and reintroduce spanwise vorticity there. This is evident in the evolution of $-\omega_b$ shown in figure 3(a), where this reentry of spanwise vorticity is marked by a sudden increase in $-\omega_b$. The time at which this reentry occurs is referred to as τ_{s1} (the subscript 1 signifying reentry after the first pairing) and is 29.2 for 2D1P. Note that, before the pairing, $-\omega_b$ becomes very small (0.02 compared to about 2 at $t = 0$). After τ_{s1}, the spanwise vorticity is again drawn out of the braid region until a second reentry occurs (at $t = \tau_{o1} = 46.5$ in this case). As can be seen in figure 1(f), this second reentry occurs when the paired roller becomes elliptical and is then drawn into the braid region. This "oversaturation" is similar to that which occurs after the roll-up in the absence of pairing. The oversaturation time is denoted by τ_{op}, where p is the number of pairings that have occurred prior to the oversaturation.[5]

When more than one pairing is allowed (cases 2D2P and 2D3P), the $-\omega_b$ evolution (fig. 3(a)) indicates that the spanwise vorticity reentry at τ_{o1} does not occur, just as the reentry at τ_{o0} did not occur in 2D1P. However, the reentry at τ_{s1} does occur, despite the occurrence of the subsequent pairings. In fact, no multiple-pairing, two-dimensional initial conditions have been found that lead to the suppression of the reentry at τ_{s1} (or at any τ_s). Thus the entry of the spiral arms into the braid region is apparently an inevitable consequence of pairing, although the timing of this reentry may be affected by subsequent pairings (see fig. 3(a)). Similarly, there are reentries at τ_{s2} and τ_{s3} ($\tau_{s2} \approx 65$, $\tau_{s3} = 139.8$), which

[4]In figures 1(b) and 1(c), the sharp interface is clearly the boundary between the rollers undergoing pairing, while in figure 1(d) it is the "edge" of the roller core.

[5]The nonpairing oversaturation time, which was called τ_o in Part 1, will be called τ_{o0} here to avoid confusion with the postpairing oversaturations.

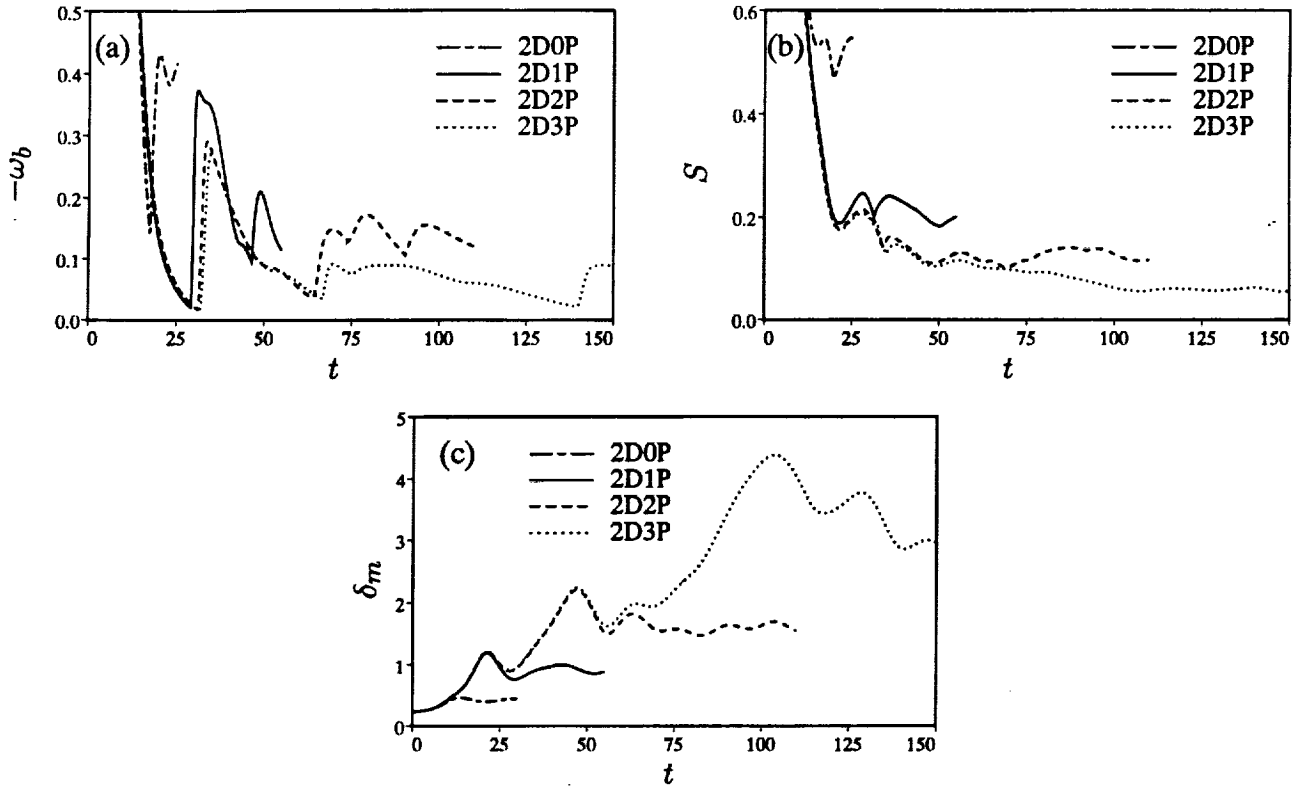

Figure 3. Time development of (a) mid-braid spanwise vorticity, (b) mid-braid strain rate, and (c) momentum thickness for 2D0P, 2D1P, 2D2P, and 2D3P.

occur after the second and third pairings, respectively ($\tau_{p2} \approx 47$, $\tau_{p3} = 103.7$). In 2D2P there is no third pairing, but there is an oversaturation at $\tau_{o2} = 90.3$. Presumably, there would also be a reentry in 2D3P at some time τ_{o3} after τ_{s3}, but this case was not run long enough to observe this. In addition to these major reentries, there are some minor variations in $-\omega_b$ after τ_{s2} and τ_{s3}. These are caused by the internal structure of the spiral arms, which was not present at the first pairing for $Re_0 = 250$.

The occurrence or suppression of an oversaturation before a pairing is dependent on the timing of that pairing. In particular, if a pairing is delayed, then oversaturation can occur before the pairing begins to dominate the evolution. This occurs in 2D1PDEL, in which the initial $A_{\frac{1}{2}0}$ is 0.01 rather than 0.03, as in the standard case. The momentum thickness (δ_m) and mid-braid spanwise vorticity ($-\omega_b$) and strain rate (S) are shown in figure 4 for 2D1P, 2D1PDEL, and 2D0P ($A_{\frac{1}{2}0} = 0$). These quantities indicate that 2D1PDEL follows the nonpairing behavior (2D0P) longer than does 2D1P. In particular, $-\omega_b$ indicates there is a reentry of spanwise vorticity into the braid region at $\tau_{o0} = 20.0$ before the pairing ($\tau_{p1} = 26.4$). This oversaturation is delayed somewhat compared to that of the nonpairing case (2D0P, $\tau_{o0} = 17.5$), and the amount of vorticity reentering the braid region is less. Note that, after the pairing in 2D1PDEL, there is a second reentry of spanwise vorticity corresponding to the spiral arms, and that $\tau_{s1} - \tau_{p1}$ in 2D1PDEL is about the same as in 2D1P (8.0 and 7.7, respectively).

As a pairing proceeds, the dominant (streamwise) length scale of the flow doubles. The thickness of the layer (as measured by δ_m) also doubles, as is apparent in figure 3(c). This has two important consequences. First, since the velocity scale remains the same, the time scale also doubles. For this

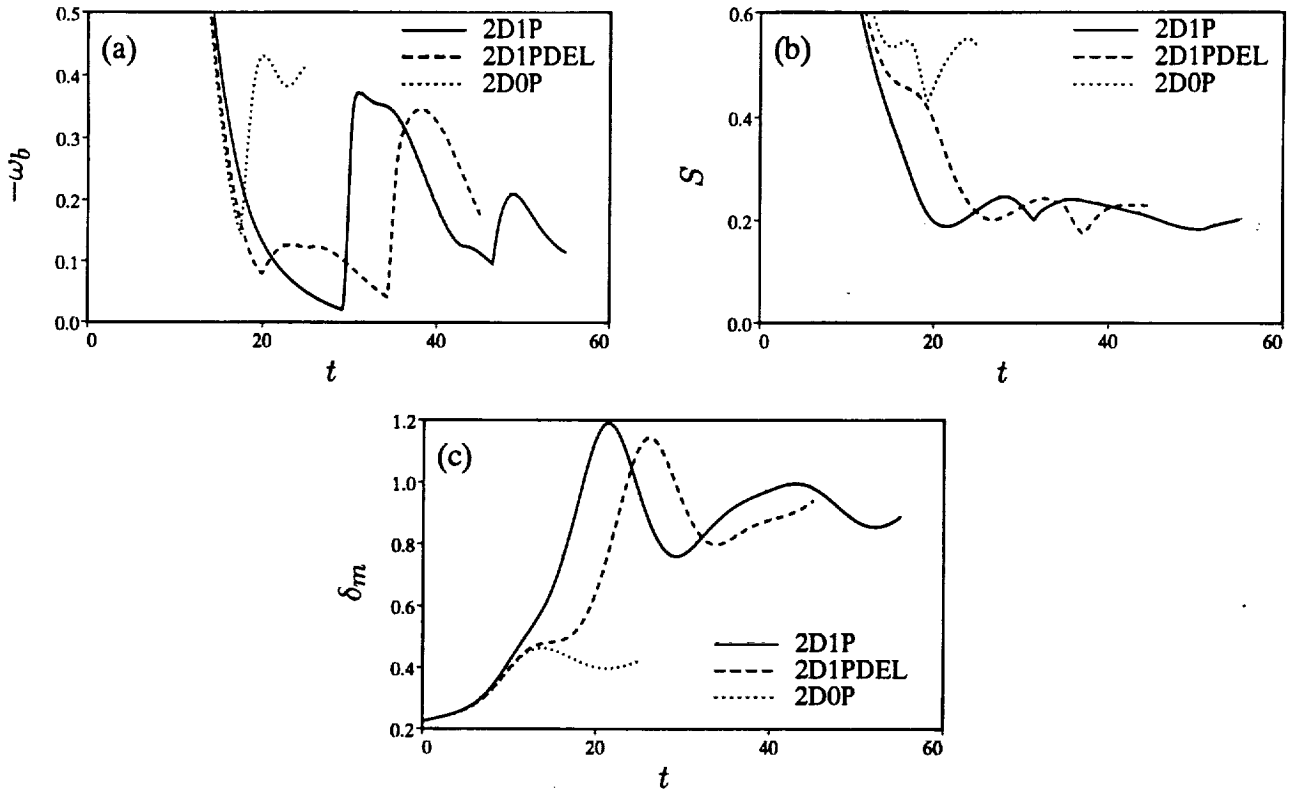

Figure 4. Time development of (a) mid-braid spanwise vorticity, (b) mid-braid strain rate, and (c) momentum thickness.

reason the time between pairings approximately doubles with each pairing (see table 1). The second consequence is that the (surviving) mid-braid strain rate (S) is approximately halved with each pairing. This is illustrated in figure 3(b), where the mid-braid strain-rate evolutions for 2D0P, 2D1P, 2D2P, and 2D3P are plotted. Note that the late-time plateau level of S for 2D1P is about 2.5 times lower than that for 2D0P (0.2 versus 0.5), but that each additional pairing does halve the plateau level (approximately 0.1 for 2D2P and 0.05 for 2D3P).

To allow comparison of the layer vorticity structure after one, two, and three pairings, spanwise vorticity contours from 2D1P, 2D2P, and 2D3P are shown in figure 5 at times near the last τ_p and last τ_s of each case. At each pairing time the pairing rollers are in about the same relative position, indicating that the maximum in $A_{\alpha 0}$ is a consistent measure of the pairing time in these cases. However, there are differences among the pairing structures. With each additional pairing, the vorticity becomes more concentrated relative to the dominant length scale in the flow (i.e., the roller spacing). The reason for this is that with each pairing two rollers are brought together and form a paired roller with vorticity concentrated in an area roughly twice that of the original rollers. However, for the paired roller to be similar to the original rollers, it should have four times the area and half the peak vorticity (since the total circulation is constant). Neither of these is the case. The only mechanism for spreading out the vorticity in this way is viscous diffusion, which at this Reynolds number is too slow to keep pace with the pairings. The resulting structure thus has high vorticity concentrated in a relatively small area, with low-level vorticity filling the rest of the area one would expect to be occupied if the pairings were self-similar. Note that at τ_s, the spiral arms become weaker with each pairing and extend further around

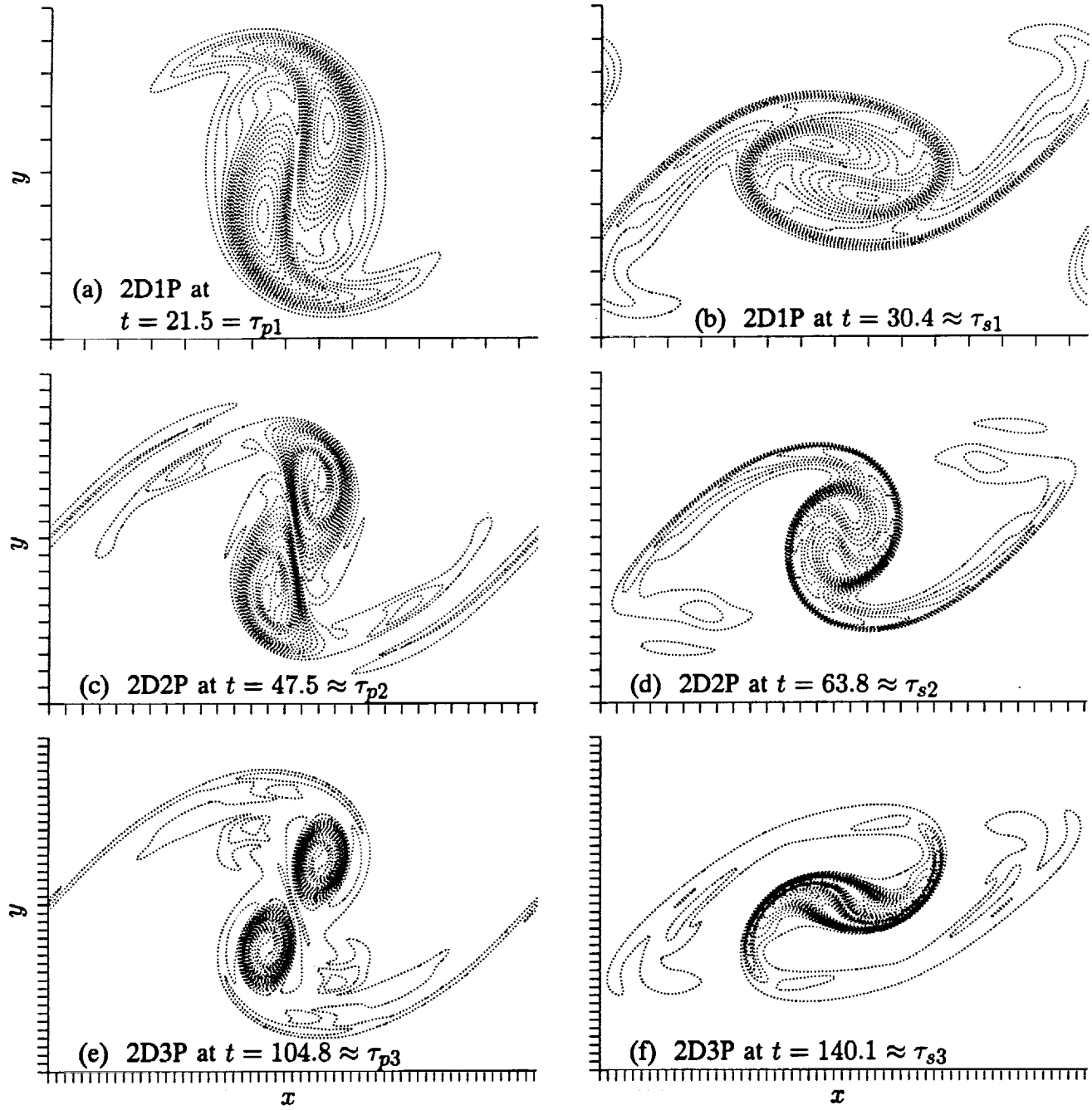

Figure 5. Contours of ω_z. The contour increment is (a,b) -0.10, (c,d) -0.08, and (e,f) -0.06; the contours are dotted to indicate negative spanwise vorticity. Tic marks are at δ_ω^0 increments.

the roller. This is also related to the fact that the concentrated vorticity is in a relatively smaller area. The time scale for rotation of the concentrated core does not increase as fast as does the time scale for the evolution of the spiral arms. Thus the concentrated core turns further over by the time the spiral arms cross the MP. Finally, with each additional pairing, there is more fine structure to the rollers. This is expected, since the effective Reynolds number has increased and since each pairing introduces more fine structure as the rollers move around each other (like kneading bread).

3.2 Reynolds-Number Variation

The effects of Reynolds-number variation were examined by studying four two-dimensional flows with initial Reynolds numbers of 100 (2D1P100), 250 (2D1P250), 500 (2D1P500), and 1000 (2D1P1000). Our primary concern is to determine the minimum Reynolds number that can be used in three-dimensional simulations without incurring unacceptable low-Reynolds-number effects. For historical reasons, the initial A_{10} and $A_{\frac{1}{2}0}$ were different from the standard case discussed in section 3.1 (0.10 and 0.05, respectively, rather than 0.04 and 0.03; see table 1).

The evolution of A_{10} is shown for all four cases in figure 6. The development of the mid-braid spanwise vorticity ($-\omega_b$), the mid-braid strain rate (S), the momentum thickness (δ_m), and the vorticity extrema ($\omega_{z\min}$) is shown in figure 7 for the same four cases. As in Part 1, these quantities indicate a severe low-Reynolds-number effect for $Re_0 = 100$. For $Re_0 = 250$, the effects are much less but still present. The characteristics of these low-Reynolds-number effects are similar to those discussed in Part 1 (see section 3.2 of Part 1 for details). One Reynolds-number effect that was not discussed in Part 1 is the presence, at $Re_0 = 500$ and $Re_0 = 1000$, of second sudden increases in $-\omega_b$ after τ_{s1} (a more subtle second increase is visible for the $Re_0 = 250$ case). This effect is due to internal structure within the spiral arms (see figs. 8(c) and 8(d)), which cannot be sustained at $Re_0 = 100$.

Contours of spanwise vorticity at $t \approx \tau_{s1}$ for the four Reynolds numbers are shown in figure 8. The internal structure of the paired eddy is significantly different for the $Re_0 = 100$ case. It is reduced in vertical extent at τ_{p1} (not shown, but see fig. 7(c)) and lacks the extra lobe of vorticity between the developing spiral arm and the core vorticity. The developed spiral arm (fig. 8(a)) is quite diffuse and shows no evidence of any internal structure. The $Re_0 = 250$ case is qualitatively more like the higher-Reynolds-number cases since it has a well-developed spiral arm (although it does lack some of the internal structure).

The results presented here and in Part 1 suggest that $Re_0 = 250$ is large enough to eliminate the worst low-Reynolds-number effects. An initial Reynolds number of 250 was therefore used for the simulations described in the remainder of this paper. This marginally adequate Reynolds number was used because the pairing simulations are significantly more computationally intensive than the nonpairing simulations in Part 1, where the initial Reynolds number was 500.

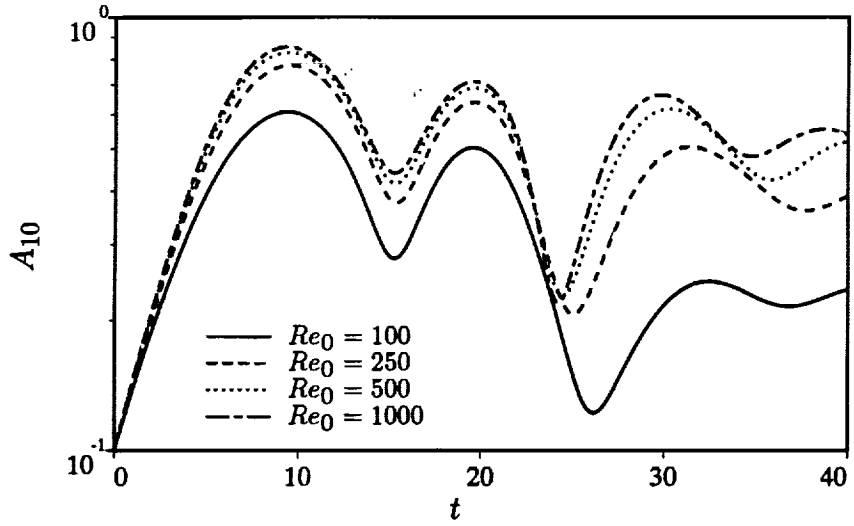

Figure 6. Time development of A_{10} for various Reynolds numbers.

4 EVOLUTION OF INFINITESIMAL THREE-DIMENSIONAL PERTURBATIONS

It was seen in Part 1 that linear analysis of the type performed by Corcos and Lin (1984) provides a good description of the three-dimensional roll-up of a mixing layer. Several similar linear computations in which the base flow undergoes one or more pairings are described in this section. As in Corcos and Lin (1984), we compute the evolution of three-dimensional, infinitesimal perturbations evolving on a two-dimensional mixing layer as it rolls up and pairs. Since the base flow is time-evolving, initial perturbations must be specified (there is no eigenvalue problem). Streamwise invariant (STI) vorticity perturbations with various spanwise wavenumbers are used, as discussed in section 2.2.

4.1 Growth of Three-Dimensional Perturbations

The two measures of the strength of the three-dimensional perturbations used here are the amplitude ($A^*_{3D} = A_{3D}/A^0_{3D}$) and the streamwise circulation in the surviving MP ($\Gamma^*_x = \Gamma_x/\Gamma^0_x$). The evolution of both these quantities for three-dimensional perturbations with $\beta = 1$ (where $\lambda_z = 0.6\lambda_x$) are shown in figure 9. Four cases that undergo 0, 1, 2, or 3 pairings are shown (the two-dimensional base flows are 2D0P, 2D1P, 2D2P, and 2D3P and are described in section 3). Despite the differences in the details of their growth, the magnitudes of A^*_{3D} and Γ^*_x remain similar through three pairings and three orders of magnitude of growth. In particular, the agreement between A^*_{3D} and Γ^*_x after oversaturation is excellent.[6] Also, neither A_{3D} nor Γ^*_x grows smoothly in time. Both quantities exhibit plateaus at each pairing time, with the plateaus for the circulations (solid curves) being particularly long. As explained in Part 1, sudden jumps in the MP circulation are caused by the reentry of spanwise vorticity into the braid region (Part 1, section 4.2.3). In figure 9, there are circulation jumps for each such reentry; that is, for each τ_s (τ_{s1}, τ_{s2}, τ_{s3}, etc.) and for τ_o. The slight variation in the timing of the circulation jumps is due to the variation in τ_s caused by subsequent pairings, as explained in section 3. More significant

[6]Note the flow undergoing three pairings does not reach oversaturation during the time shown.

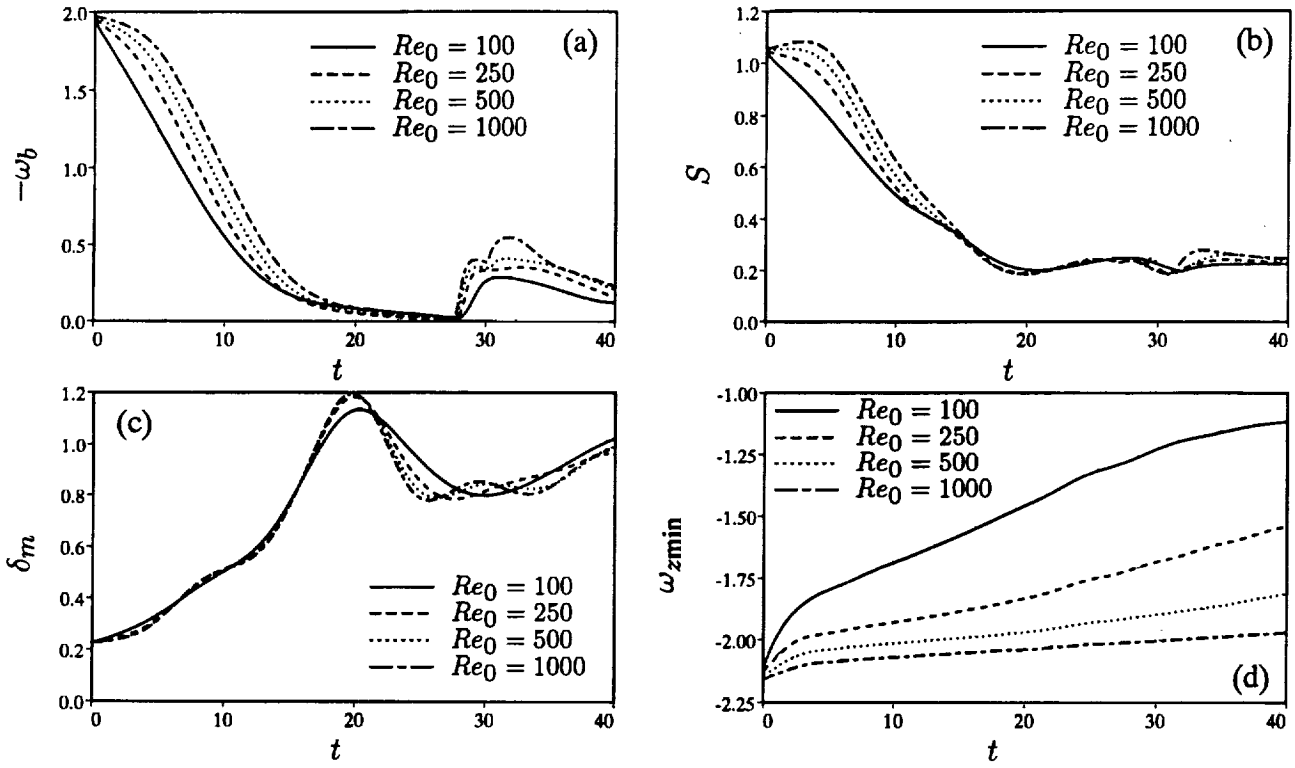

Figure 7. Time development of (a) mid-braid spanwise vorticity, (b) mid-braid strain rate, (c) momentum thickness, and (d) vorticity extrema for various Reynolds numbers.

differences in the Γ_x^* evolutions are apparent after τ_o for each case. Flows undergoing further pairings do not exhibit a growth in Γ_x^* at this point (they are not oversaturated). As with Γ_x^*, there is very little difference in A_{3D}^* (dashed curves) among the cases until about τ_o, well after the last pairing of each case. Thus, by these measures, τ_o is the time when a flow becomes significantly affected by the lack of further pairings.

The circulation jumps that occur prior to later pairings reach the next plateau level quickly. Those that occur after the last pairing of each case are more irregular and protracted. This is because further pairings draw the vorticity in the spiral arms back out of the braid region and therefore shorten the period over which the circulation can increase. It is also apparent in figure 9 that the irregularity in the circulation increase after the final pairing of each simulation increases with the pairing number. This is due to the greater complexity of the perturbation and base flow as the number of pairings increases.

At each level, further pairings result in less three-dimensional energy growth and less circulation growth than that associated with oversaturation, i.e., the A_{3D}^* and Γ_x^* curves for cases with more pairings lie below those with fewer pairings. Thus pairings inhibit the growth of three-dimensionality, although pairings do not actually reduce three-dimensionality. This has been observed both in experiments (Huang and Ho, 1990) and in other numerical simulations (Metcalfe et al., 1987; compare E_Σ in their fig. 17 to the single-pairing A_{3D}^* curve in our fig. 9). Pairing produces this inhibition of three-dimensionality by suppressing the oversaturation of the two-dimensional roller (τ_o), thus preventing the reentry of spanwise vorticity into the surviving braid region. Since spanwise vorticity is then essentially absent

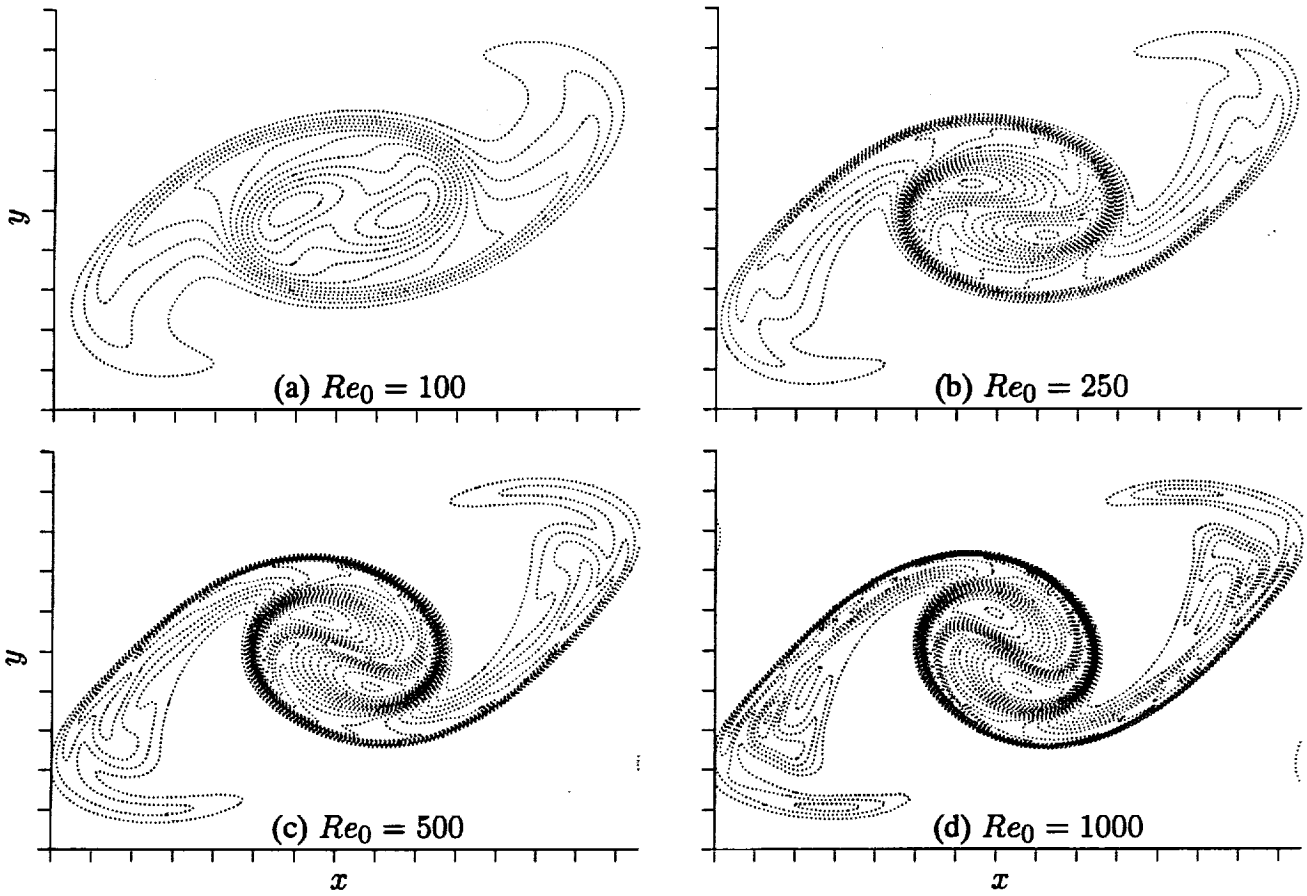

Figure 8. Contours of ω_z at $t = 28.0 \approx \tau_{s1}$. The contour increment is -0.1 and the contours are dotted to indicate negative spanwise vorticity. Tic marks are at δ_ω^0 increments.

from the braid region, the MP or rib circulation cannot grow. This limits the possible growth of three-dimensionality, as discussed below. This growth limitation is only temporary, since spanwise vorticity does ultimately reenter the braid region at τ_s (see section 3).

If pairing is significantly delayed, oversaturation can occur prior to the pairing (section 3.1), resulting in more growth of three-dimensionality. This is illustrated in figure 10, where A_{3D}^* and Γ_x^* are shown for the nonpairing and single-pairing cases (2D0P and 2D1P) as well as the delayed-pairing case (2D1PDEL). Because the pairing is not progressing fast enough to prevent spanwise vorticity from entering the braid region, the circulation increases at around $\tau_{o0} = 20.0$ in the delayed-pairing case (by a factor of 3); there is a corresponding increase in A_{3D}^*. In the delayed-pairing case, the spiral arms form later and the corresponding jump in circulation at τ_s is consequently also delayed. Interestingly, the factor by which the circulation increases at τ_{s1} is about the same in the delayed-pairing and normal-pairing cases. After τ_{o1} (the second oversaturation to occur in the delayed-pairing case) the growth of both A_{3D}^* and Γ_x^* for the pairing cases is qualitatively similar, although the level of these quantities in the delayed-pairing case is higher. The increased three-dimensionality resulting from the first oversaturation (τ_{o0}) in the delayed-pairing case is thus permanently embedded in the flow.

Note that the circulation increase associated with the first oversaturation in the delayed-pairing case begins somewhat before $\tau_{o0} = 20.0$. This is because the minimum in $-\omega_b$ is not a precise measure of

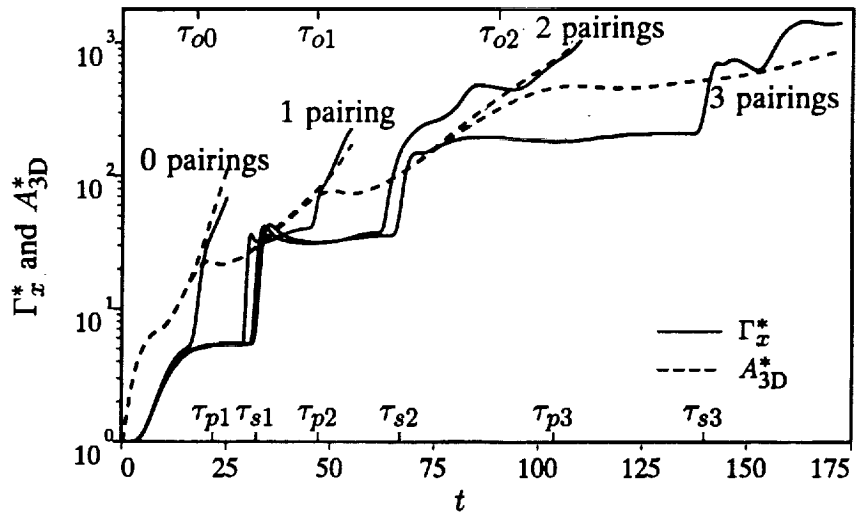

Figure 9. Time development of Γ_x^* and A_{3D}^* of three-dimensional linear perturbations evolving in the presence of a two-dimensional base flow that undergoes 0, 1, 2, or 3 pairings (2D0P, 2D1P, 2D2P, and 2D3P, respectively).

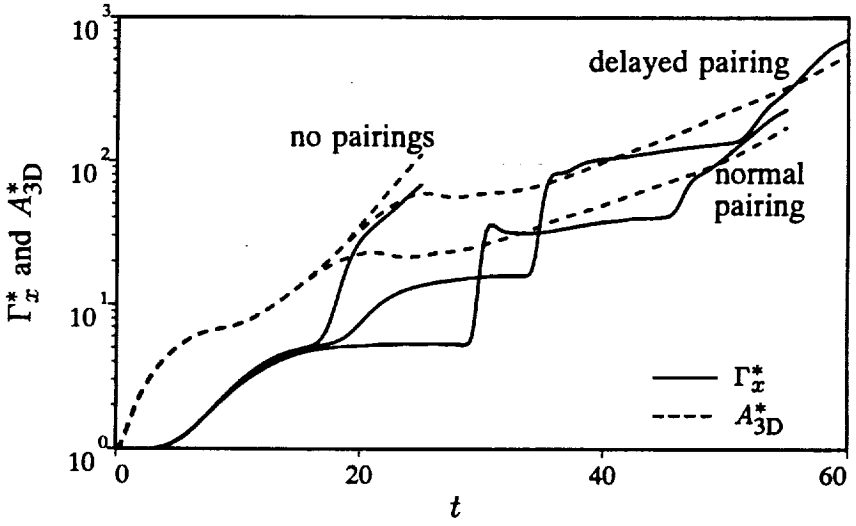

Figure 10. Time development of Γ_x^* and A_{3D}^* of three-dimensional linear perturbations evolving in the presence of a two-dimensional base flow which undergoes no pairings, a delayed pairing, or a normal pairing (2D0P, 2D1PDEL, and 2D1P, respectively).

when new-perturbation spanwise vorticity (required for circulation growth) crosses the MP. Spanwise vorticity that is weaker than that still present in the MP reenters before τ_o. This effect is accentuated in this case because the competition between pairing and oversaturation causes the spanwise vorticity to approach and cross the MP very slowly. This competition also causes the circulation to grow gradually instead of jumping, as in the other reentries.

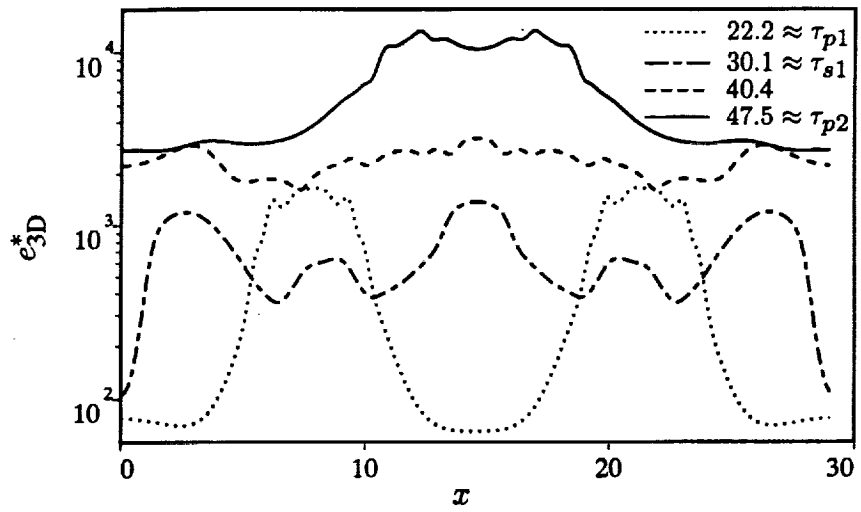

Figure 11. Normalized perturbation energy density e^*_{3D} as a function of x at the four times indicated in the legend for a $\beta = 1$ perturbation evolving on a base flow undergoing two pairings (2D2P).

The evolution of A^*_{3D} can be further studied by examining the three-dimensional disturbance energy density given by

$$e_{3D} = \frac{1}{L_z}\int_{-\infty}^{\infty}\int_0^{L_z} u_i u_i - < u_i >_z < u_i >_z \, dz\, dy \tag{14}$$

where $<>_z$ is the spanwise average. The amplitude A_{3D} is related to the normalized energy density ($e^*_{3D} = e_{3D}/e^0_{3D}$)[7] by

$$A^*_{3D} = \sqrt{\frac{1}{L_x}\int_0^{L_x} e^*_{3D} dx} \tag{15}$$

In figure 11, e^*_{3D} is shown as a function of x for the two-pairing case at several times between the first and second pairings. At τ_{p1}, the energy is concentrated in the cores of the rollers.[8] As the spiral arms enter the braid regions (see section 3), energy is transferred out of the core and into the braid regions, causing the energy in the braid regions to grow. By τ_{s1}, the maximum energy density in the braid region is greater (by a factor of two) than that in the cores. Also note that, at this time, the MP of the braid region to be engulfed in the next pairing ($x = 14.6$) has experienced a large growth, while the surviving MP ($x = 0$ and $x = 4\lambda_x = 29.2$) has not. This is because, at τ_{s1}, the spiral arms have just crossed the surviving MP and energy growth is just starting. The spiral arms enter parts of the braid region and initiate circulation and energy growth before they ultimately reach the surviving MP; this causes A^*_{3D} to leave its plateau and begin growing well before τ_s. Later ($t = 40.4$), the energy continues to grow at all x and becomes roughly uniformly distributed in x. Finally, at the second pairing, the energy has again grown larger in the core than in the braid region.[9] Between $t = 40.4$ and $t = \tau_{p2}$, the energy density is growing only in the roller core, since the spanwise vorticity has again been removed from the braid region. Finally, by τ_{p2}, A^*_{3D} stops growing for a while (during the plateau regions in fig. 9).

[7]Note that because the initial disturbance is STI, e^0_{3D} is independent of x.

[8]At τ_{p1}, the paired rollers are centered at $x = 7.8$ and 21.4. At τ_{p2} the single remaining roller is centered at $x = 14.6$.

[9]Note that the energy is more highly concentrated in the cores at the first pairing than at the second. This is because of the greater complexity of the perturbations at the second pairing (see section 4.3).

At this point e^*_{3D} in the surviving MP is constant, and the only changes occurring in the e^*_{3D} profile consist of a mild redistribution of energy in the roller core. Apparently the roller disturbances come into some sort of temporary "equilibrium" with the braid disturbances, which can no longer grow. The above process is repeated as another spiral-arm reentry and pairing occur.

Another consequence of the growth mechanism discussed above is that the long-term growth of the three-dimensional perturbations in the presence of pairings is algebraic rather than exponential. One way to see this is to consider the circulation evolution. The above discussion suggests that the magnitude of the circulation jump that occurs at each τ_s should be proportional to the circulation just before the jump because the circulation jump is governed by the spanwise vorticity disturbance brought into the MP. The strength of this vorticity disturbance should be proportional to the circulation level since the roller and ribs have "equilibrated." There may also be a weak dependence on the pairing number or other details of the two-dimensional flow. This is supported by the results in figure 9, where the circulation appears to jump by a constant factor at each τ_s. Thus $\Gamma^*_x \sim \Gamma_j^{N_p}$ where N_p is the pairing number and $\Gamma_j \approx 6$ is the factor by which the circulation jumps at each τ_s. On the other hand, the time between jumps should scale approximately as 2^{N_p}, since the length and time scales roughly double at each pairing (section 3.1). Therefore $\Gamma^*_x \sim A^*_{3D} \sim t^{\log_2 \Gamma_j}$. A similar conclusion is reached if one assumes that, since the length and time scales grow linearly with t, the average growth rate (σ) of the perturbations varies like $\sigma \sim 1/t$. On the other hand, the length and time scales would no longer grow linearly if pairing were suppressed. In this case, spanwise vorticity from the oversaturated roller continually occupies the braid region, resulting in continuous circulation growth. The growth is then apparently exponential, in agreement with the results of Pierrehumbert and Widnall (1982), whose model problem (the Stuart vortices) is similar to an array of oversaturated rollers. Since the long-term growth of the three-dimensional perturbations in the presence of pairings is algebraic, the degree of three-dimensionality one ultimately obtains in any finite time depends greatly on the magnitude of the initial (or inlet) disturbances.

4.2 Spanwise Scale Changes

In the linear analysis presented above, only disturbances with $\beta = 1$ were considered. The evolution of infinitesimal perturbations with $\frac{1}{8} \leq \beta \leq 4$ is examined in this section. This allows the determination of the most unstable spanwise wavelength, as well as how this wavelength changes in time. Simulations of such spanwise scale changes in flow with finite-amplitude, three-dimensional disturbances are discussed in section 7.

The three-dimensional disturbance amplitudes of perturbations with various spanwise wavelengths ($\frac{1}{4} \leq \beta \leq 4$) are shown in figure 12. Over most of the time period shown, the largest amplitude is attained by the $\beta = 1$ disturbance. This is why $\lambda_z = 0.6\lambda_x = 0.696(2\pi)$ was chosen for most of the simulations in Part 1 and for all of the cases described in this paper.

The dotted curve ($A^*_{s\frac{3}{4}}$) in figure 12 corresponds to a slightly (33%) longer disturbance wavelength than that of the fundamental (A^*_{s1}). After $t \approx 25$, the growth rate of $A^*_{s\frac{3}{4}}$ exceeds that of A^*_{s1}, causing $A^*_{s\frac{3}{4}}$ to eventually overtake A^*_{s1}. Thus, the preferred spanwise wavelength is increasing slowly as the flow evolves. To better illustrate this, a simulation that undergoes several pairings is considered. The

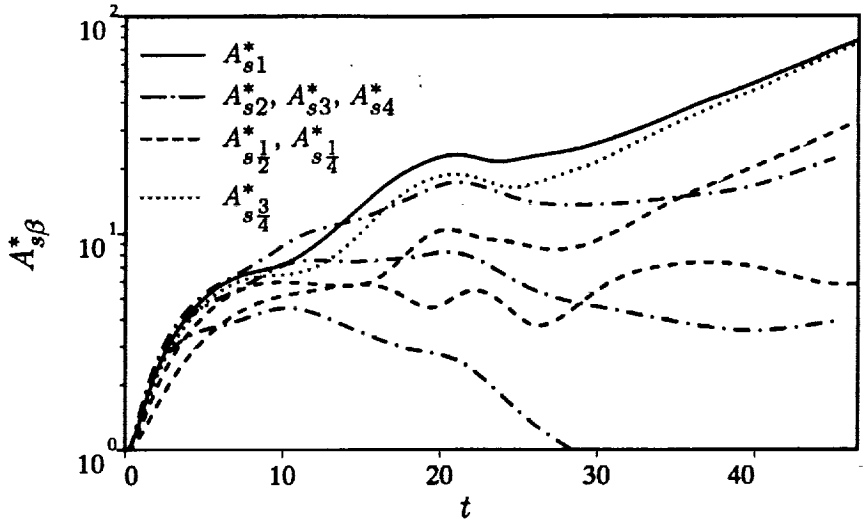

Figure 12. Time development of three-dimensional disturbance amplitudes ($A^*_{s\beta}$) of various spanwise wavelength disturbances until just past $\tau_{o1} = 46.5$ for the single-pairing case 2D1P. Note that the subharmonic $A^*_{s\frac{1}{2}}$ is larger than $As\frac{1}{4}^*$ at both $t = 10$ and $t = 40$ and that the harmonics A^*_{s2}, A^*_{s3}, and A^*_{s4} are in order of decreasing amplitude.

evolutions of the amplitudes of perturbations with various spanwise wavelengths through three pairings of the two-dimensional base flow are shown in figure 13. After the second pairing ($\tau_{p2} = 47.0$), $A^*_{s\frac{3}{4}}$ is larger than A^*_{s1}. After $\tau_{s3} = 140.0$, $A^*_{s\frac{1}{2}}$ also overtakes A^*_{s1}. The first spanwise subharmonic is then more energetic than the fundamental, though both of these disturbances are less energetic than that with $\beta = \frac{3}{4}$. The growth in the dominant spanwise length scale is so slow that a doubling of the scale apparently requires three or four pairings. Thus linear analysis does not support the "self-similar" picture of mixing-layer growth where each pairing is accompanied by a doubling of the characteristic spanwise length scale. As noted in section 3.1, the roller core becomes proportionately smaller after each pairing. The slow scale change described above is therefore consistent with the most unstable spanwise scale being determined by the size of the roller core, rather than by the spacing between rollers.

Disturbances with wavelengths greater than about two and a half times the spacing between spanwise rollers are largely stable. This is apparent in figure 14, where the time development of such long-spanwise-wavelength disturbances is compared to that of fundamental ($\beta = 1$) disturbances in a nonpairing and a two-pairing base flow. A $\beta = \frac{1}{4}$ disturbance evolving in a nonpairing base flow (fig. 14(a)) exhibits no growth of Γ^*_x until τ_o and no growth of $A^*_{s\beta}$ (after the increase associated with the initial buildup of ω_y for $t < 10$; see section 3.1 of Rogers and Moser, 1992) until $t \approx 30$. Similarly, the amplitude $A^*_{s\beta}$ of a $\beta = \frac{1}{8}$ disturbance does not grow (after the initial rise) until after two pairings of the base flow (fig. 14(b)). Note that, for both these disturbances, both Γ^*_x and $A^*_{s\beta}$ ultimately grow together (apparently exponentially) in the oversaturated state, as was the case for $\beta = 1$ disturbances (section 4.1).

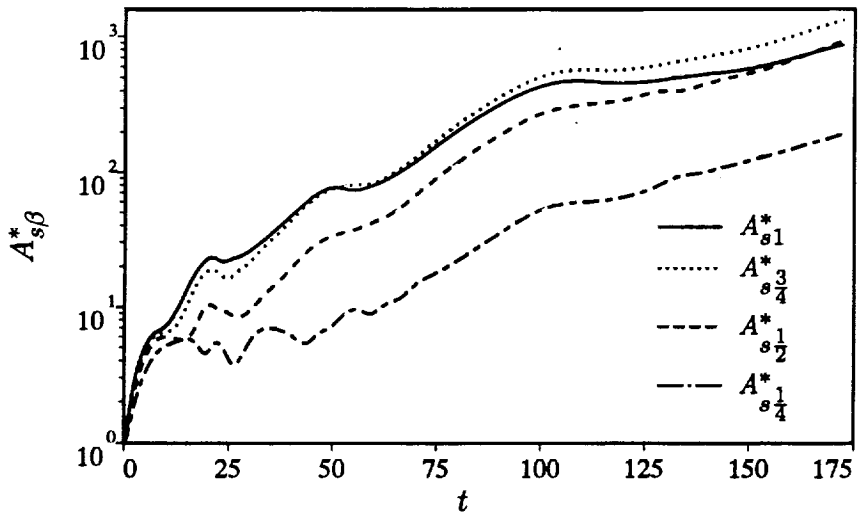

Figure 13. Time development of three-dimensional disturbance amplitudes ($A^*_{s\beta}$) of various spanwise wavelength disturbances through three pairings (2D3P).

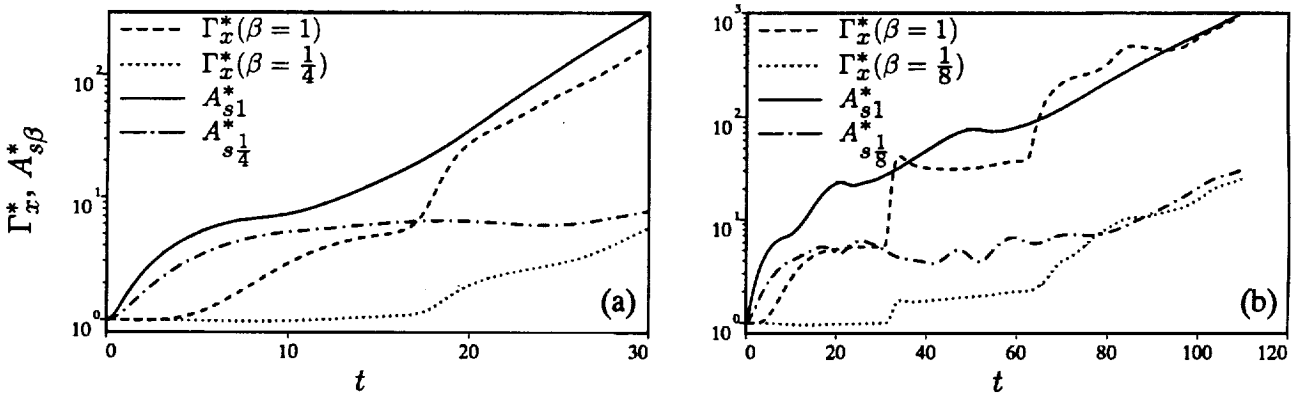

Figure 14. Time development of circulations (Γ^*_x) and three-dimensional disturbance amplitudes ($A^*_{s\beta}$) for various spanwise wavelength disturbances for (a) a case with no pairings (2D0P) and (b) a case with two pairings (2D2P).

4.3 Structure of the Linear Perturbations

The structure of the three-dimensional perturbations is of interest since, as noted in Part 1, similar features are present in fully nonlinear simulations well past the onset of three-dimensional nonlinearity. The $\beta = 1$ perturbation streamwise vorticity at τ_p and τ_s for the first, second, and third pairings is shown in figure 15. At each time, the streamwise vorticity associated with the ribs is clearly visible. However, as spanwise vorticity is brought into the braid region around τ_s, streamwise vorticity perturbations are formed far from the center of the layer in the braid region (fig. 16(b)). They are then brought together by the two-dimensional strain in the braid region. This is occurring in figure 16. In the MP, the pattern of streamwise vorticity resembles five pairs of ribs stacked on top of each other. These distinct regions of streamwise vorticity are eventually pressed together by the strain, allowing viscosity to merge them so that only one region is apparent by the next pairing (fig. 15(c)). This amalgamation of streamwise vorticity occurs by a different mechanism for finite-amplitude disturbances (see Part 1 and

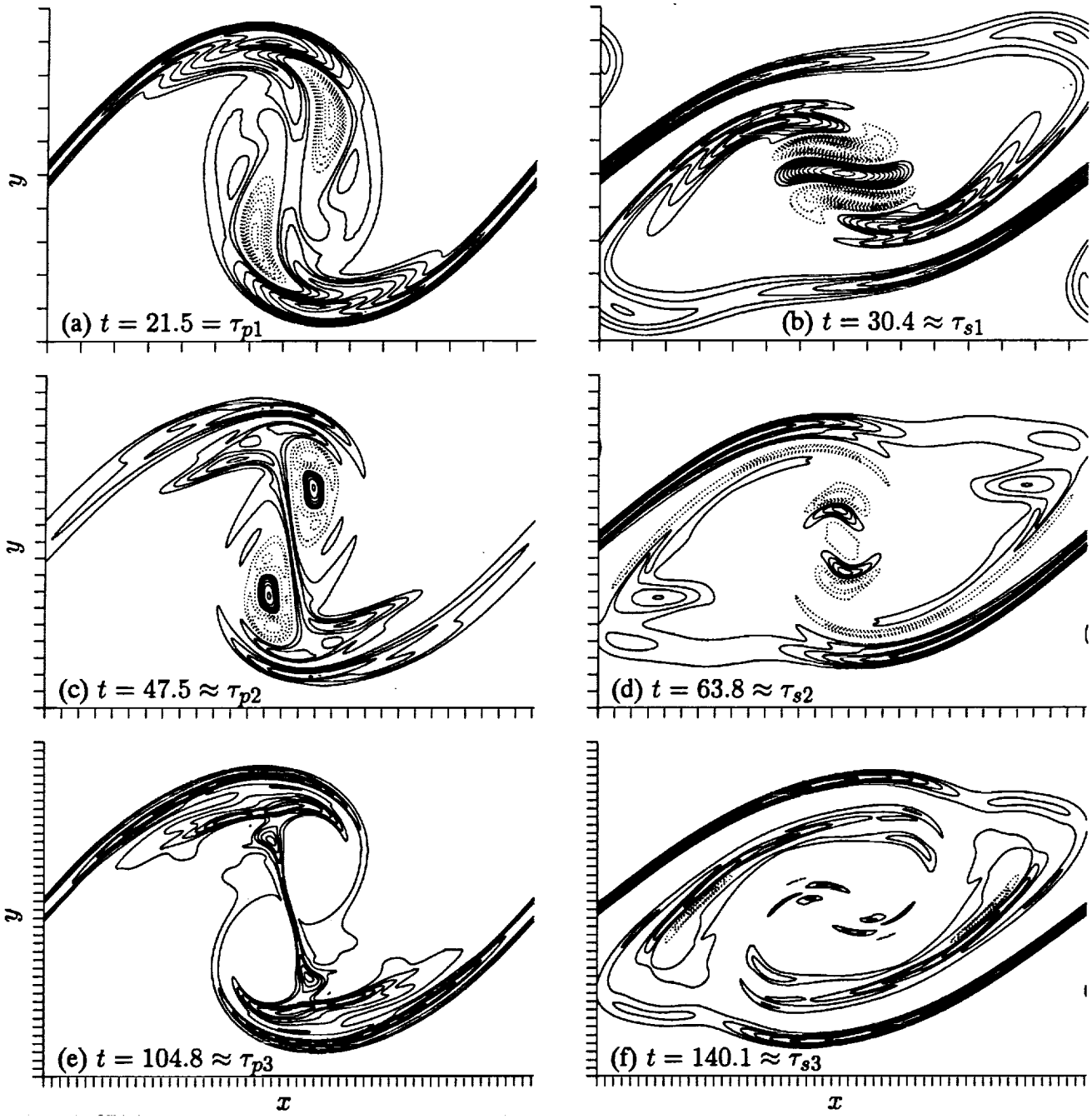

Figure 15. Contours of ω_x for perturbations with $\beta = 1$ in the RP. Perturbations are evolving on a base flow undergoing (a,b) one, (c,d) two, and (e,f) three pairings (2D1P, 2D2P, and 2D3P, respectively). The contour increments are (a,b) $1.5\Gamma_x^0/{\delta_\omega^0}^2$, (c,d) $5\Gamma_x^0/{\delta_\omega^0}^2$, and (e,f) $16\Gamma_x^0/{\delta_\omega^0}^2$. Solid contours indicate positive vorticity, dotted contours indicate negative vorticity, and tic marks are at δ_ω^0 intervals.

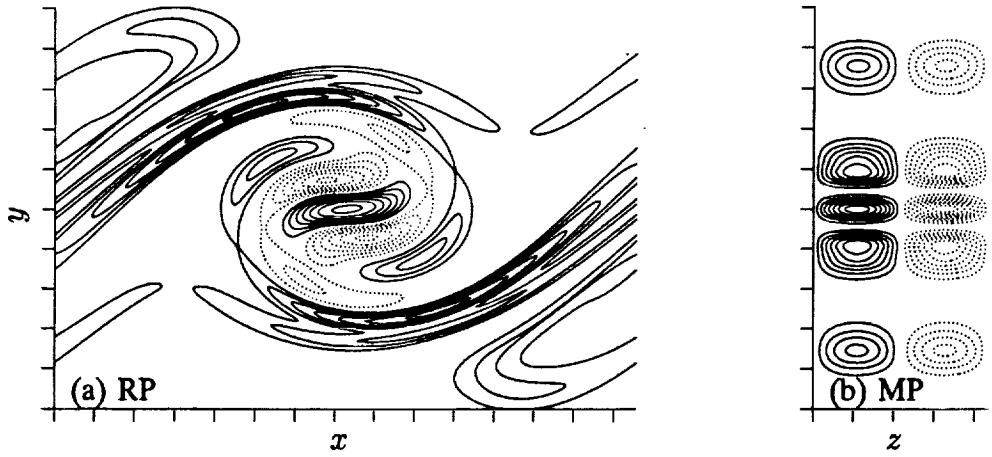

Figure 16. Contours of ω_x for a perturbation with $\beta = 1$ evolving on a single-pairing base flow (2D1P); $t = 35.1$ (a time after that in fig. 15(b)). The contour increments are (a) $3\Gamma_x^0/{\delta_\omega^0}^2$ and (b) $\Gamma_x^0/{\delta_\omega^0}^2$. Solid contours indicate positive vorticity, dotted contours indicate negative vorticity, and tic marks are at δ_ω^0 intervals.

also section 5 of this paper). Similar layered vorticity patterns form in the braid regions after further pairings (figs. 15(d) and 15(f)).

Also apparent in these figures is the streamwise vorticity in the roller cores. At the first pairing (τ_{p1}), the streamwise vorticity associated with each of the original unpaired rollers is visible as a large region of negative vorticity. For each pairing, the relative magnitude of the streamwise vorticity disturbances remaining in the prepairing cores is smaller until, at τ_{p3} (fig. 15(e)), there is virtually no streamwise vorticity disturbance left in the cores. The other vorticity components are also small in the prepairing cores at τ_{p3}. At the same time, the streamwise vorticity disturbances away from the core become more complicated, with finer structure relative to the size of the roller. This change is expected, since the effective Reynolds number is doubling with each pairing. Also, with each additional pairing the disturbance is "folded over" (like kneaded bread), resulting in more striated disturbances. This is especially apparent in the perturbation spanwise vorticity disturbances ($\omega_z^{3D} = \omega_z - < \omega_z >_z$), shown for τ_{p2} and τ_{p3} in figure 17. It is important to recall that these very complicated perturbation flows are a result of a linear evolution. The source of the complexity is the evolving base flow, not three-dimensional nonlinearity. Even with these differences between the disturbances at different pairings (disturbance levels in the cores and fineness of striations), several of the qualitative features of the vorticity fields are the same during the second and third pairings (see figs. 15 and 17).

As noted in section 4.2, disturbances with $\beta = \frac{1}{4}$ are largely stable until the onset of a pairing, and those with $\beta = \frac{1}{8}$ are largely stable until the beginning of a second pairing. Vorticity contours of these largely stable disturbances show qualitative differences from their fundamental ($\beta = 1$) disturbance counterparts.[10] In figure 18 a comparison is made of the streamwise vorticity structure of the $\beta = 1$ (fundamental) and $\beta = \frac{1}{8}$ disturbances at a time between the first and second pairings (these cases are the same as those shown in fig. 14(b)). In addition to being much weaker, the ω_x structure in the $\beta = \frac{1}{8}$

[10]The structures of the other unstable perturbations (e.g., $\beta = \frac{1}{2}$) are qualitatively similar to those of the $\beta = 1$ case.

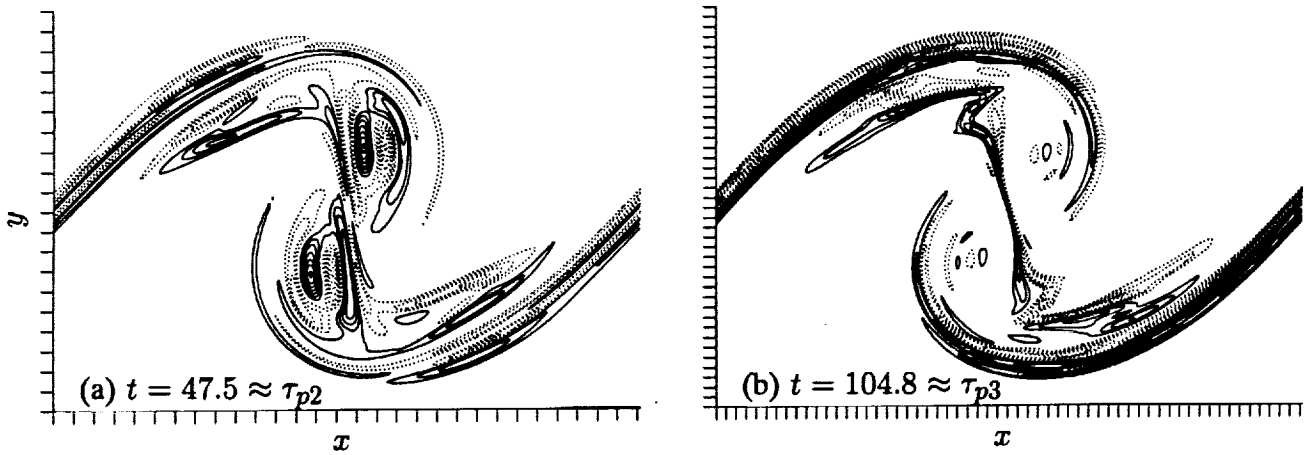

Figure 17. Contours of perturbation spanwise vorticity (ω_z^{3D}) in the RP of $\beta = 1$ perturbations evolving on a (a) two-pairing (2D2P) and (b) three-pairing (2D3P) base flow. The contour increment is $12\Gamma_x^0/\delta_\omega^{0\,2}$. Solid contours indicate positive vorticity, dotted contours indicate negative vorticity, and tic marks are at δ_ω^0 intervals.

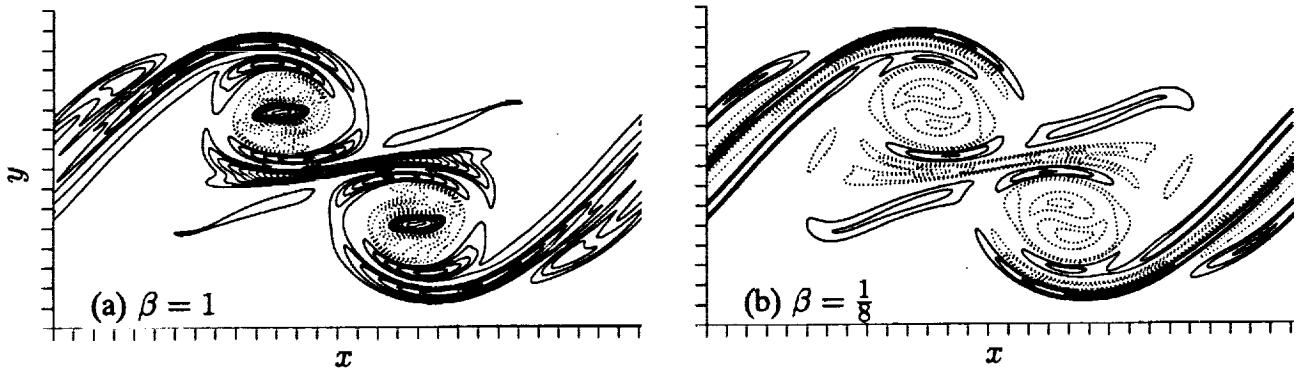

Figure 18. Contours of ω_x in the RP at $t = 40.4$ ($\tau_{p2} = 46.7$) on a base flow undergoing two pairings (2D2P). The contour increments are (a) $3\Gamma_x^0/\delta_\omega^{0\,2}$ and (b) $0.04\Gamma_x^0/\delta_\omega^{0\,2}$. Solid contours indicate positive vorticity, dotted contours indicate negative vorticity, and tic marks are at δ_ω^0 intervals.

case is qualitatively different, e.g., the engulfed rib vorticity is negative rather than strongly positive and the MP contains layers of ω_x that alternate in sign.

5 THREE-DIMENSIONAL PAIRINGS

In this section, the full nonlinear evolution of a mixing layer undergoing one pairing is examined. Results from two simulations with different initial three-dimensional disturbance strengths are studied and compared with the linear analysis discussed in sections 4.1 and 4.3. Table 2 lists some characteristics of the initial conditions for these two simulations (LOW1P and HIGH1P) along with values of several of the reference times defined and used in this paper; other simulations referred to later in the paper are included in the table as well. In both simulations the initial three-dimensional perturbation is in the spanwise fundamental $(0, 1)$ Fourier mode (see eq. (11)).

Table 2. Parameters of the three-dimensional simulations. Two-dimensional disturbance profiles are VE unless superscripted $^{\omega G}$, in which case they are ωG. Three-dimensional disturbance profiles are ωG unless superscripted ^{vG}, in which case they are vG. $Re_0 = 250$, $\phi_{\alpha 0} = 0$, $\lambda_x = 1.16(2\pi)$, $\lambda_z = 0.6\lambda_x$, and $Pr = 1.0$ for all cases. A "T" indicates that the flow is too "turbulent" for τ_{s2} to be well defined. Numbers given with less precision (τ_{s1}) are the result of $-\omega_b$ not being computed at every time step for some simulations. All the flows were either too "turbulent" or not computed long enough to determine τ_{o1} and τ_{o2}. The HIGH0P simulation was referred to as LOWDEL in Part 1.

Simulation	A_{10} $\times 10^2$	$A_{\frac{1}{2}0}$ $\times 10^2$	$A_{\frac{1}{4}0}$ $\times 10^2$	A_{01}† $\times 10^2$	$A_{0\frac{1}{2}}$† $\times 10^2$	$A_{0\frac{1}{4}}$† $\times 10^2$	$\phi_{0\frac{1}{2}}$	$\phi_{0\frac{1}{4}}$	τ_r	τ_{o0}	τ_{p1}	τ_{s1}	τ_{p2}	τ_{s2}
HIGH0P	4.00			8.32					12.4	15.9				
LOW1P	4.00	3.00		1.66					11.9		21.6	28.8		
HIGH1P	4.00	3.00		8.32					11.5		23.4	27.4		
LOW2P	$4.52^{\omega G}$	$3.47^{\omega G}$	$5.14^{\omega G}$	1.59					11.8		21.1	32	40.0	53
MID2P	$4.52^{\omega G}$	$3.47^{\omega G}$	$5.14^{\omega G}$	3.18					11.8		21.1	32	40.3	54
HIGH2P	$4.52^{\omega G}$	$3.47^{\omega G}$	$5.14^{\omega G}$	9.64^{vG}					11.2		20.1	31.2	38.3	T
PH$\frac{\pi}{4}$0P	4.00			8.32	6.66		$\frac{\pi}{4}$		12.2	15.4				
PH01P	4.00	3.00		8.32	6.66		0		11.4		22.2	27.1		
PH$\frac{\pi}{4}$1P	4.00	3.00		8.32	6.66		$\frac{\pi}{4}$		11.4		22.0	27.7		
PH$\frac{\pi}{8}$1P	4.00	3.00		8.32	6.66		$\frac{\pi}{8}$		11.4		22.0	27.4		
WMID2P	$4.52^{\omega G}$	$3.47^{\omega G}$	$5.14^{\omega G}$	3.18	1.02	1.54	0	0	11.8		21.1	31	40.1	54
WHIGH2P	$4.52^{\omega G}$	$3.47^{\omega G}$	$5.14^{\omega G}$	9.64^{vG}	2.71^{vG}	1.54	0	0	11.2		20.4	31	38.5	T
TURB2P	4.00	3.00	3.00	8.32	6.66	10.11	$\frac{\pi}{8}$	$\frac{7\pi}{16}$	11.3		21.0	29.2	47.1	T

†For comparison with cases cited in Part 1, $\Gamma_x/A_{0\beta} = 4.382$, 5.472, and 7.210 for ωG disturbances with $\beta = 1$, 1/2, and 1/4, respectively. For vG disturbances, $\Gamma_x/A_{0\beta} = 4(\pi/2)^{1/4} k_z/\sqrt{k_z^2 + 1}$, where $k_z = 2\pi\beta/\lambda_z$.

5.1 Weakly Three-Dimensional Pairing

In Part 1 it was found that the evolution of infinitesimal three-dimensional perturbations provided a good approximation of finite-amplitude perturbations even after the onset of three-dimensional nonlinearity. This is also true for flows undergoing pairings. In figure 19, the evolutions of the normalized three-dimensional amplitude A^*_{3D} and the normalized circulation Γ^*_x for both the LOW1P and HIGH1P flows are compared to those derived from linear analysis in section 4. These three simulations are begun from initial conditions that are identical except for the strength of the three-dimensional perturbation, with LOW1P having a weaker (by a factor of five) three-dimensional perturbation than HIGH1P (see table 2). As can be seen in figure 19, both the amplitude and circulation of LOW1P evolve nearly as predicted by linear analysis, with some slight differences occurring during and after the pairing. In contrast, the stronger perturbation of HIGH1P results in some departure from linear analysis as soon as $t = 5$.

Despite the good agreement between linear analysis and the LOW1P simulation, there are some nonlinear effects at, and beyond, the first pairing.[11] In figures 20 and 21, the streamwise vorticity and the three-dimensional spanwise vorticity ω_z^{3D} of both LOW1P and the corresponding linear analysis are shown for times near τ_{p1} and τ_{s1}. At τ_{p1} there is little difference in ω_x between the linear and nonlinear computations. All the same features are present, though some details of shape and level are slightly different. In contrast, the three-dimensional spanwise vorticity in the BP is significantly different at τ_{p1}. The nonlinear evolution of the "cups" (discussed in Part 1), which are visible in figure 21(b) as the two intense regions of negative perturbation, has resulted in the divergence of the solutions. It is remarkable that the streamwise vorticity and the integrated diagnostics (e.g., A^*_{3D} and Γ^*_x) are not significantly affected. Also note that the linear perturbations have the following symmetry:

$$\omega_i(x, y, z) = \omega_i(-x + 2x_s, -y, z) \quad \text{where } i \text{ denotes } x \text{ or } y, \text{ and} \tag{16}$$

$$\omega_z(x - x_s, y - y_s, z) = -\omega_z(-x + x_s, -y + y_s, z) \tag{17}$$

where $(x_s, y_s) = (0, 0)$ or $(\frac{\lambda_x}{2}, 0)$. This symmetry is preserved by the linearized equations, but not by the Navier-Stokes equations. Thus the symmetry is not apparent in figure 21(b).

By τ_{s1}, differences due to nonlinear effects in the LOW1P flow are more pronounced. The ribs begin a marginal collapse, which results in wider streamwise vorticity contours in the braid region (fig. 20(d)). The collapse parameter $\mathcal{L}$ is shown in figure 19(c). This parameter is based on the results of Lin and Corcos (1984) and is discussed in depth in Part 1. In the LOW1P flow, $\mathcal{L}$ reaches a plateau level that is just below the collapse criterion level (13.1) by τ_{p1}. The marginal collapse observed in this flow is thus in agreement with the predictions of Lin and Corcos (1984). The structure of the streamwise vorticity in the paired roller of LOW1P has also begun to diverge from the linear results. There is no longer a correspondence between all regions of positive and negative vorticity for the two cases. Contours of ω_z^{3D} are again different in the linear and nonlinear cases. In particular, at this time the relative magnitude of the ω_z^{3D} perturbation is somewhat lower in LOW1P than in the linear case. The strength of the three-dimensional spanwise vorticity can be measured by W_{z3D}, which is defined analogously to the amplitude A_{3D} (the spanwise vorticity is used instead of the velocity in eq. (7)).

[11] Note that the same level of three-dimensionality in nonpairing flows resulted in no discernible differences until after τ_{o0} (see Part 1).

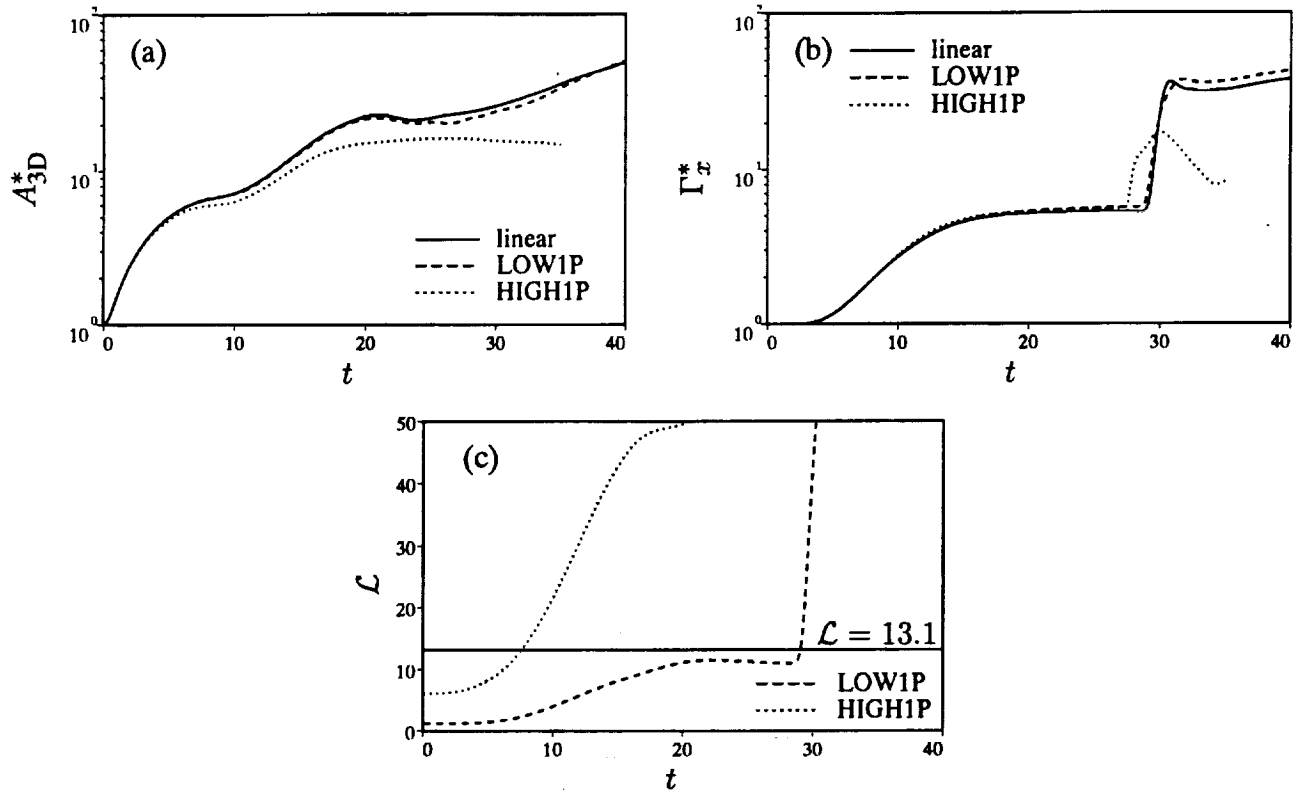

Figure 19. Time development of (a) A^*_{3D}, (b) Γ^*_x, and (c) the Lin and Corcos collapse parameter $\mathcal{L}$ for various levels of initial three-dimensionality. Note $\mathcal{L} = 0$ for linear analysis.

The spanwise vorticity amplitude W_{z3D} normalized by $\Gamma^0_x/\delta^{0\,2.5}_\omega$ is 48% lower in the LOW1P case (5.80 for LOW1P and 8.57 from linear analysis). At later times this discrepancy in the strength of the spanwise vorticity perturbation gets larger, as can be seen in figures 21(e) and 21(f). At this time ($t = 40.0$) the normalized W_{z3D} is 6.36 for LOW1P and 14.65, according to linear analysis. Note that, at this time, the discrepancies in the magnitudes of the other vorticity components and the velocity components are less than 8%. The above results suggest that the spanwise vorticity perturbations are the first to encounter significant nonlinearity and to saturate, but that this occurs without significantly affecting the other vorticity components. As noted above, the development of the cups is responsible for this difference.

5.2 Highly Three-Dimensional Pairing

The HIGH1P flow described in this section results from an initial STI disturbance of the same amplitude as that used in the ROLLUP case described in Part 1 (a factor of five larger than in LOW1P). As expected, the early evolution of HIGH1P is very similar to that of its nonpairing counterpart. In particular, the prepairing evolution of HIGH1P is characterized by the same "cups" and collapsed "ribs" that were described in detail in Part 1 (compare fig. 22 with fig. 10 of Part 1). A quantitative comparison between the evolution of vorticity extrema, mid-braid spanwise vorticity, mid-braid strain rate, and momentum thickness in the HIGH1P and HIGH0P (corresponding nonpairing flow) is given in figures 22 and 23. The differences between the two flows become significant by $\tau_{o0} = 15.9$ of HIGH0P. Despite this similarity, comparison of figure 22 with figure 10 in Part 1 reveals two effects

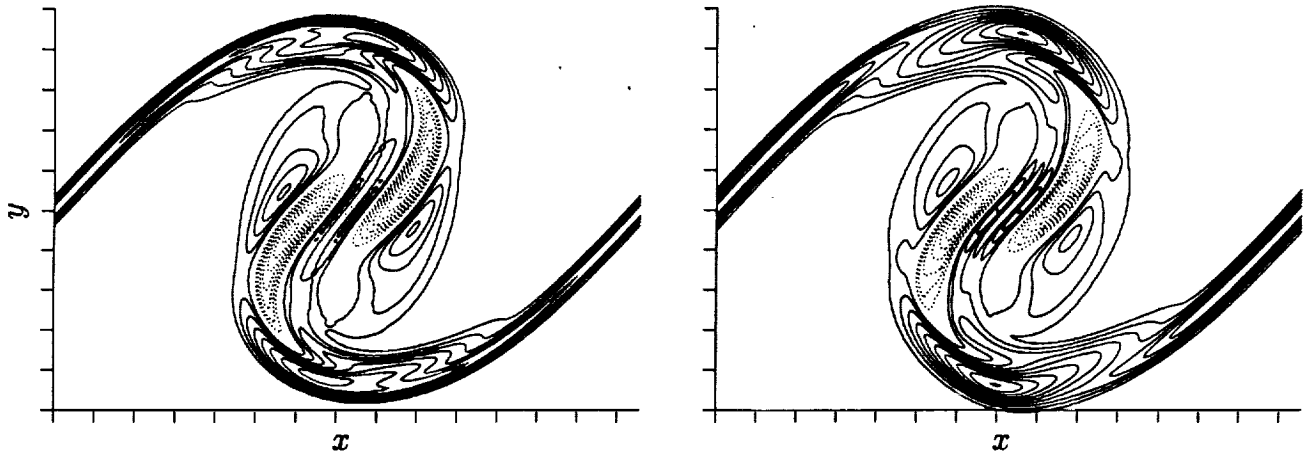

(a) LOW1P at $t = 22.6 \approx \tau_{p1}$ (b) linear at $t = 22.6 \approx \tau_{p1}$

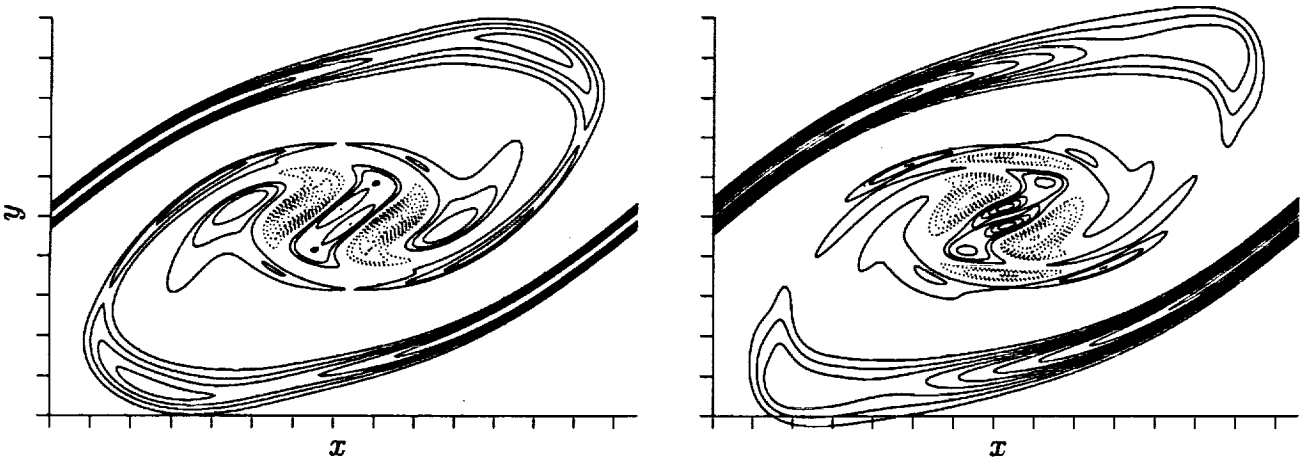

(c) LOW1P at $t = 28.2 \approx \tau_{s1}$ (d) linear at $t = 28.2 \approx \tau_{s1}$

Figure 20. Contours of ω_x in the RP. The base flow for the linear analysis is 2D1P. Contour level is $1.5\Gamma_x^0/{\delta_\omega^0}^2$. Negative contours are dotted.

of the impending pairing. First, the ribs that will be engulfed (center of the x-domain) are perceptibly different from the surviving ribs (edges of the x-domain). In particular, they are more closely aligned with the streamwise direction in the pairing flow (resulting in larger values of ω_x and smaller values of ω_y in fig. 23). Second, the two rollers in the domain are closer together than in the nonpairing case, indicating that the pairing has begun.

As with the nonpairing flows discussed in Part 1, HIGH1P is highly three-dimensional and undergoes significant three-dimensional nonlinear evolution (see fig. 19). In fact, the three-dimensional amplitude (A_{3D}) exceeds A_{s0} for most of the evolution (fig. 25(a)). The three-dimensionality also affects the two-dimensional modes (fig. 25(b)). Note that the peak in the subharmonic amplitude ($A_{\frac{1}{2}0}$) is broader and is delayed relative to the two-dimensional case. Also, in the two-dimensional case the amplitude of the fundamental oscillates as the pairing rollers corotate (section 3.1). Such large oscillations are not evident in HIGH1P because the pairing rollers lose their identity before $\tau p1$ (see below). Despite the strong three-dimensionality of this flow, the circulation of the rib vortices (Γ_x) is well predicted by

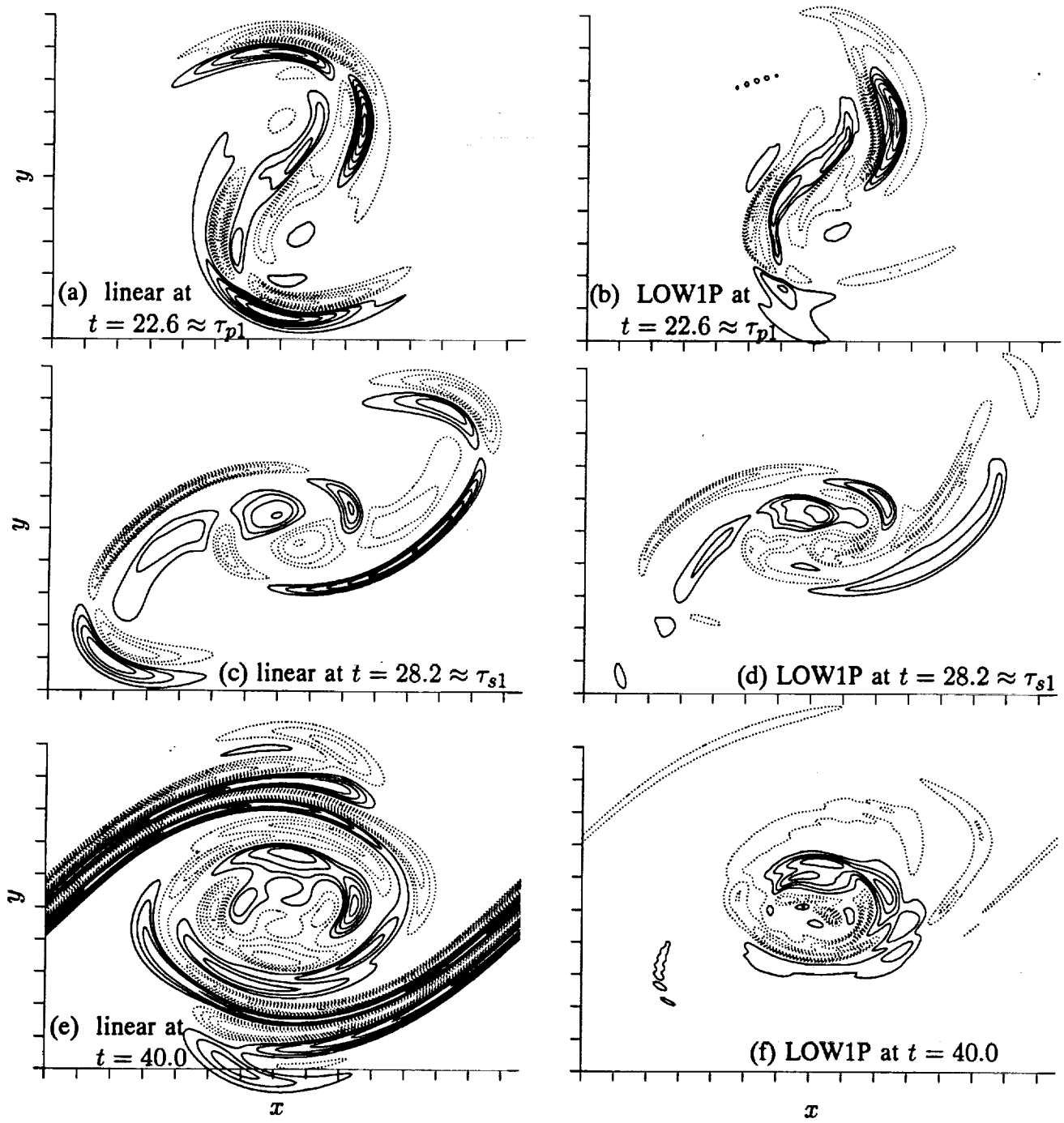

Figure 21. Contours of perturbation spanwise vorticity (ω_z^{3D}) in the BP. Contour level is $3\Gamma_x^0/\delta_\omega^{0\,2}$. Negative contours are dotted.

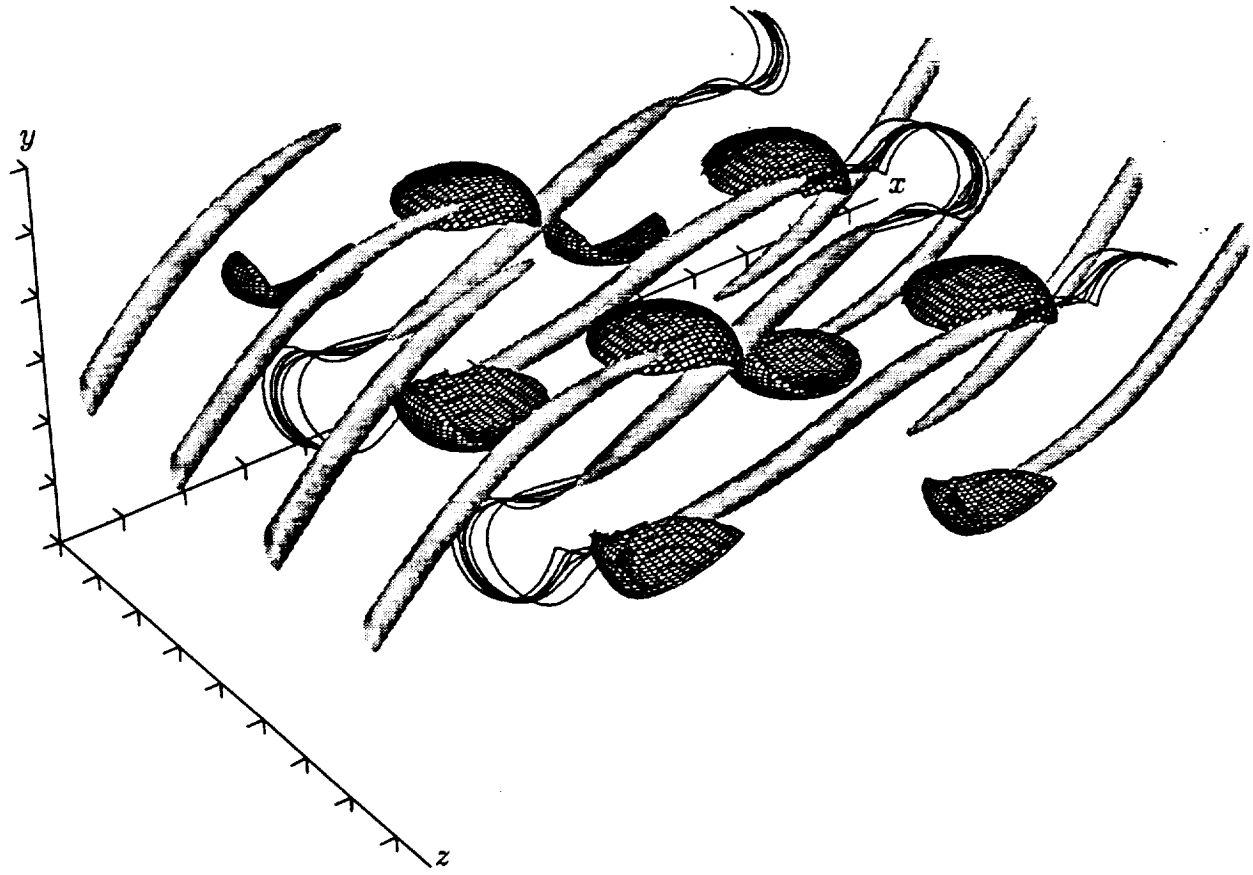

Figure 22. Surfaces of constant vorticity magnitude and vortex lines at $t = 14.6$ in HIGH1P. Cross-hatched surfaces represent $\omega_z = -4.0$ and solid surfaces show $\sqrt{\omega_x^2 + \omega_y^2} = 4.0$. The "rib" structures include ω_x and ω_y of the same sign; this sign alternates in z (negative for the closest rib). Note that periodicity has been used to extend the domain in the spanwise direction and that the same vortex lines go through both of the counterrotating rib vortex pairs (concealed by the rib surface contour). Tic marks are at δ_ω^0 intervals.

the linear computations until τ_{s1} (see fig. 19(c)), as are the plateau levels of mid-braid vorticity and strain rate ($-\omega_b$ and S; see fig. 24). Thus, the plateau level of the Lin and Corcos (1984) collapse parameter (see eq. (A-3)) can be well predicted in this flow by scaling the linear results (fig. 24(d)).

As was discussed in Moser and Rogers (1991), pairing of the cups and ribs ultimately results in a transition to turbulence. This process is depicted in more detail for HIGH1P in figures 26 and 27, where the spanwise vorticity in the BP (between-ribs plane) and RP (rib plane) is shown. There are several key features of this development that were noted in Moser and Rogers (1991). First the cups are torn apart (fig. 26(c)), and then the spanwise vorticity in the BP reorganizes into thin sheets (fig. 26(d)) that subsequently undergo secondary roll-ups (fig. 26(e)). During the same time, the relatively simple prepairing spanwise vorticity pattern in the RP (figs. 27(a) and 27(b)) is transformed into an apparently turbulent vorticity distribution (fig. 27(f)), with many small-scale granular regions of both signs of spanwise vorticity. The flow rapidly becomes too complex to allow a detailed description of the development of all its features, but the analysis presented below does yield some insight into the processes underlying this transition.

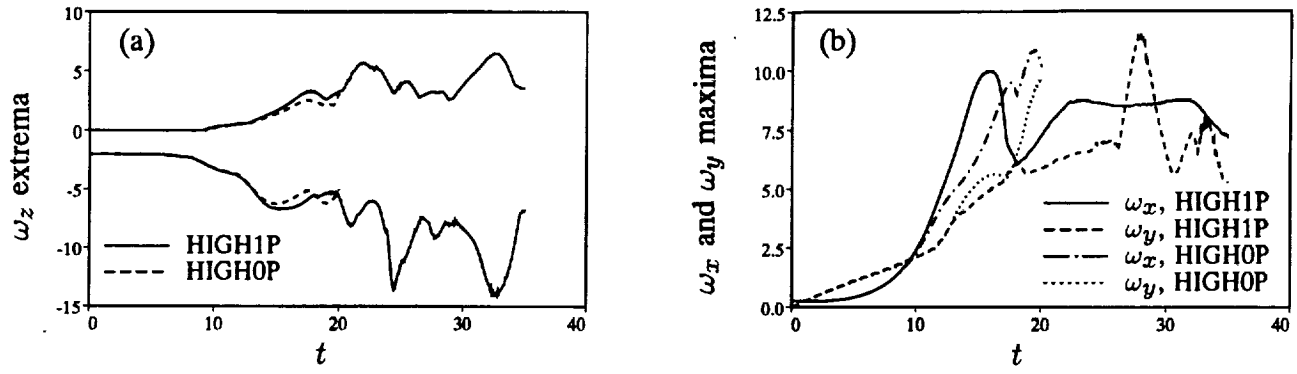

Figure 23. Time development of (a) ω_z extrema and (b) maxima of ω_x and ω_y.

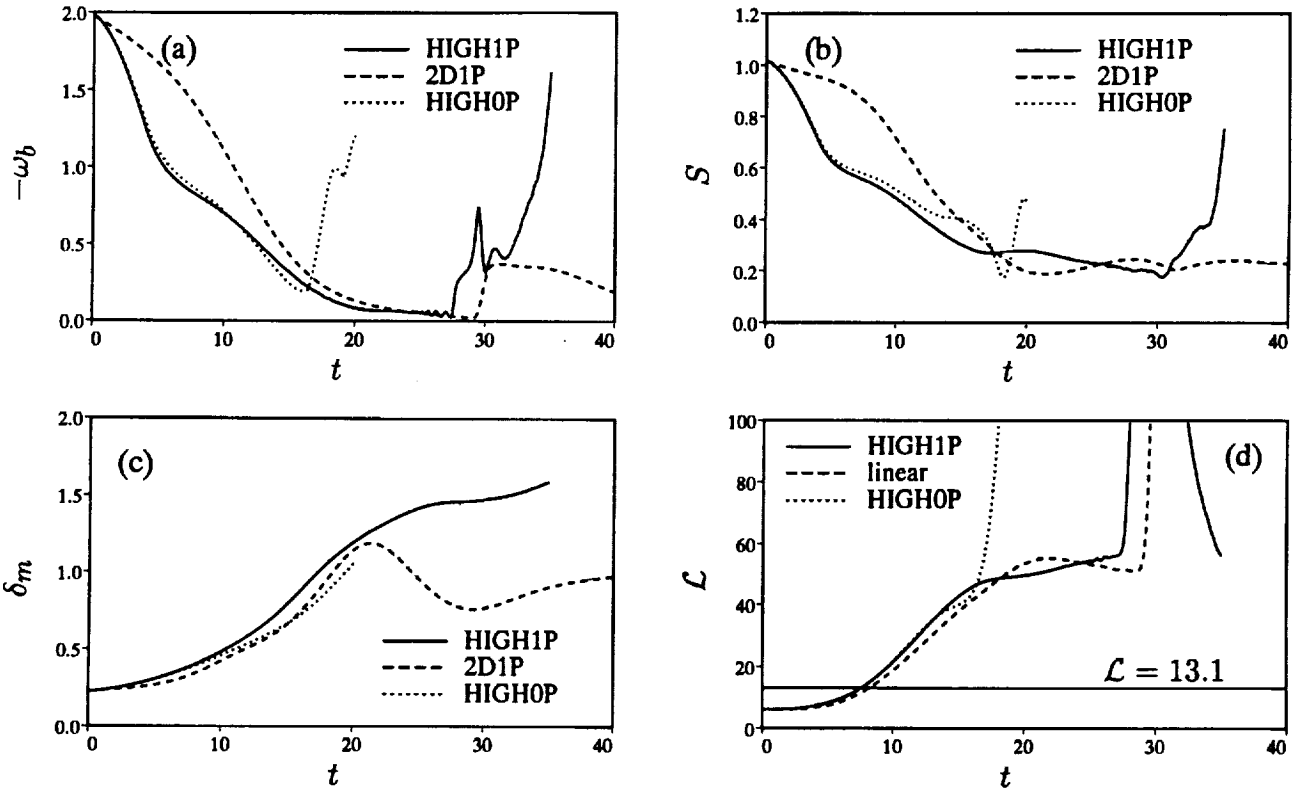

Figure 24. Time development of (a) mid-braid vorticity, (b) mid-braid strain rate, (c) momentum thickness, and (d) the Lin and Corcos collapse parameter. In (d), the curve labeled *linear* was obtained by scaling Γ_x^0 to be the same as the value in HIGH1P.

As in Part 1, the point symmetry (eq. (13)) (present in HIGH1P) allows the vortex lines associated with the ribs to be unambiguously defined since the rib vortices are constrained to be centered at the symmetry points. In HIGH1P there are symmetry points in both the surviving and engulfing braid region, so both sets of rib vortex lines can be tracked. HIGH1P also satisfies the plane symmetry (eq. (12)), which requires that w, ω_x, and ω_z be zero in the between-ribs plane (BP). The equation governing the spanwise vorticity in the BP is thus particularly simple:

$$\frac{\partial \omega_z}{\partial t} + u\frac{\partial \omega_z}{\partial x} + v\frac{\partial \omega_z}{\partial y} = \omega_z\frac{\partial w}{\partial z} + \frac{1}{Re}\left(\frac{\partial^2 \omega_z}{\partial x^2} + \frac{\partial^2 \omega_z}{\partial y^2}\right) + \frac{1}{Re}\frac{\partial^2 \omega_z}{\partial z^2} \tag{18}$$

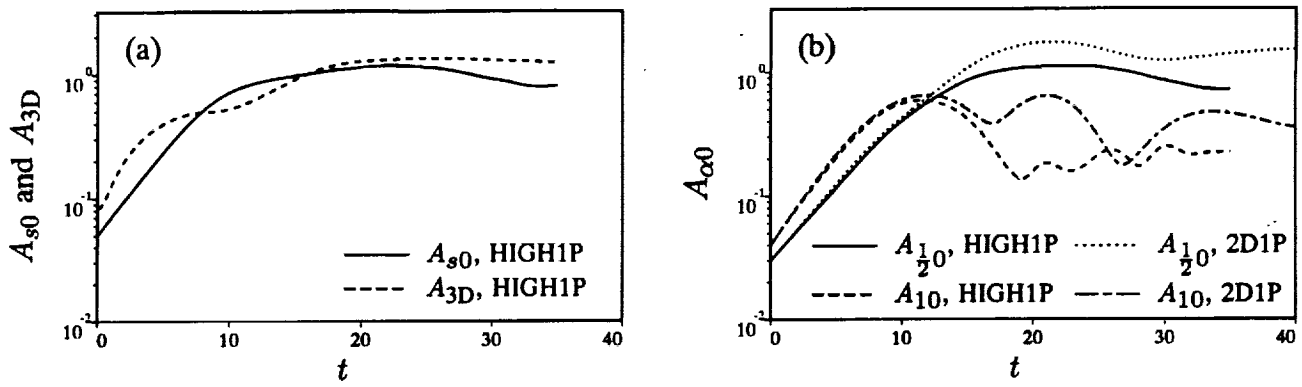

Figure 25. Time development of disturbance amplitudes for HIGH1P and the corresponding two-dimensional case (2D1P).

This is the two-dimensional vorticity equation except for the single stretching term ($\omega_z \frac{\partial w}{\partial z}$) and the spanwise diffusion term ($\frac{1}{Re} \frac{\partial^2 \omega_z}{\partial z^2}$).

5.2.1 Evolution of rib vortex lines– It is apparent from figure 22 that, at $t = 14.6$, the vortex lines passing through the ribs leave the RP and are twisted around each other near a horseshoe tip that connects one rib vortex to its neighbor. This distortion gives rise to the positive spanwise vorticity regions in the rib plane at this time (fig. 27(a)). Such distortion of rib vortex lines was seen to be the major source of positive spanwise vorticity in the absence of pairings (Part 1). Rib vortex lines at $t = 19.3$ are shown in figure 28. The vortex lines for both the surviving ribs and the engulfed ribs are highly distorted, with large excursions out of the rib plane. Note that, at several points, the vortex lines through neighboring engulfed ribs are coming very close together. This proximity allows viscosity to reconnect the vortex lines, yielding a different topology at a later time. This has already begun to occur, as is evidenced by the small regions of positive spanwise vorticity in the BP at this time (fig. 26(b)). Initially, the spanwise vorticity was all negative in this plane. According to equation (18), the only way that positive spanwise vorticity can arise in the BP is by viscous diffusion in the spanwise direction. At several locations this diffusion results in viscous reconnection of the vortex lines. The positive regions of spanwise vorticity shown in figure 26(b) are located where the engulfed rib vortex lines shown in figure 28 are pinched together. It is interesting to note that, in this very complicated flow, the topology of the vortex lines associated with the major structures is still largely that of the initial vortex sheet, i.e., there has been almost no vortex reconnection to form closed vortex loops or vortex lines running counter to the mean flow across the entire spanwise domain.

Where the rib vortex lines cross the rib plane, there must be a region of nonzero spanwise vorticity. The correspondence of features in the spanwise vorticity contours with rib vortex line crossings is shown in figure 27(b). Note that almost all the regions of nonzero spanwise vorticity are associated with the crossing of rib vortex lines. The major exceptions are the four long, thin regions of particularly strong vorticity associated with the cup structures. There are also two small positive regions near the center of the roller that are associated with the "sub-rib" structure discussed in Part 1. The spanwise vorticity pattern in the between plane can also be understood in terms of the cups and wisps associated with the rib and sub-rib vortex lines (see Part 1). Thus, the features of the mixing layer at this time are manifestations of the structures present in the nonpaired layer.

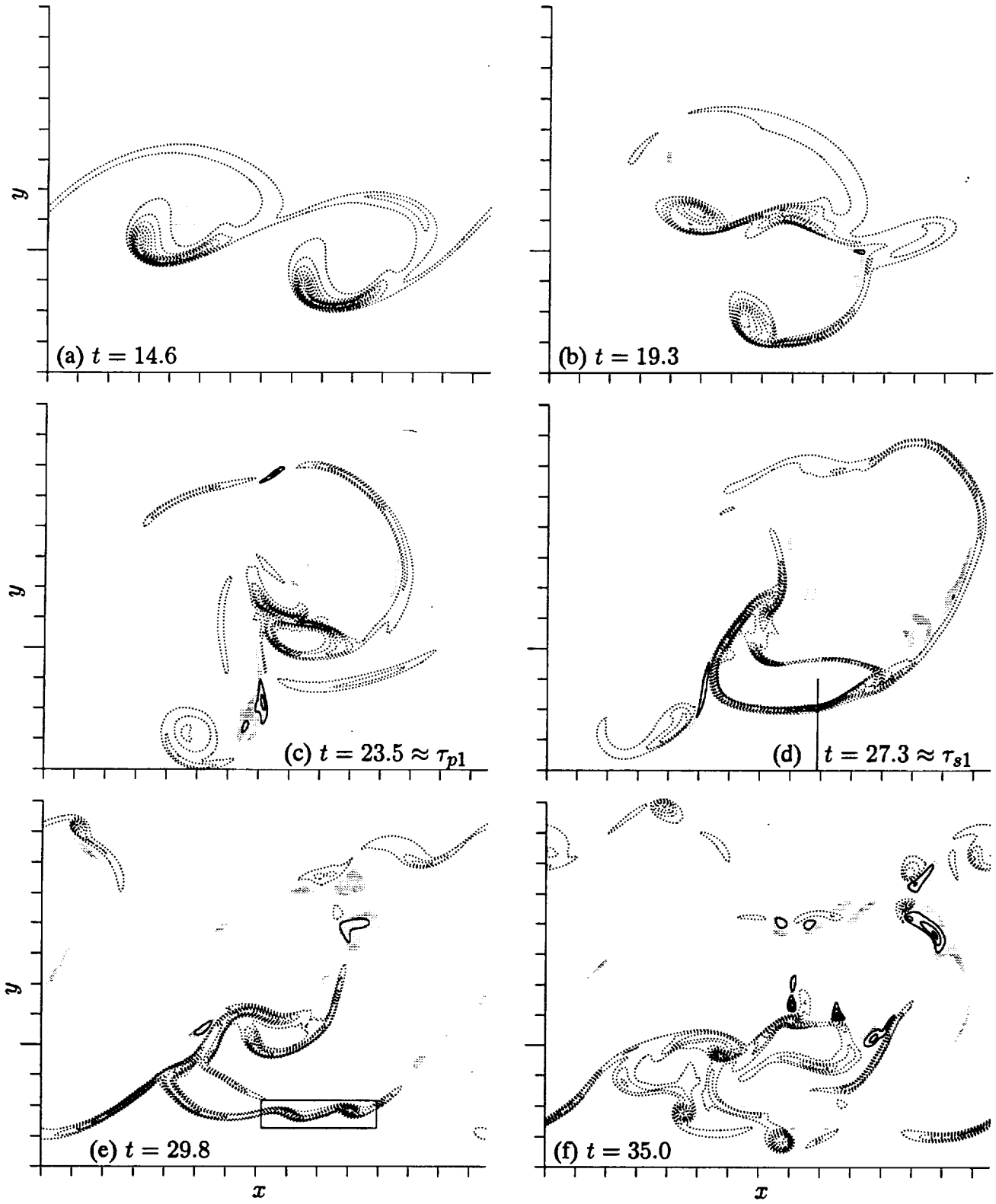

Figure 26. Contours of ω_z in the $z = 0$ BP of HIGH1P. The contour increments are (a,b,f) ± 0.6 and (c,d,e) ± 0.8 (approximately $1.65\Gamma_x^0/\delta_\omega^0$ and $2.20\Gamma_x^0/\delta_\omega^0$, respectively). Negative contour levels are dotted. Regions of positive spanwise vorticity are shaded. $y = 0$ is at the long tic mark, not the center of the domain. The secondary roll-up marked with a box in (e) and the plane given by the vertical line in (d) will be further investigated later. Tic marks are at δ_ω^0 increments.

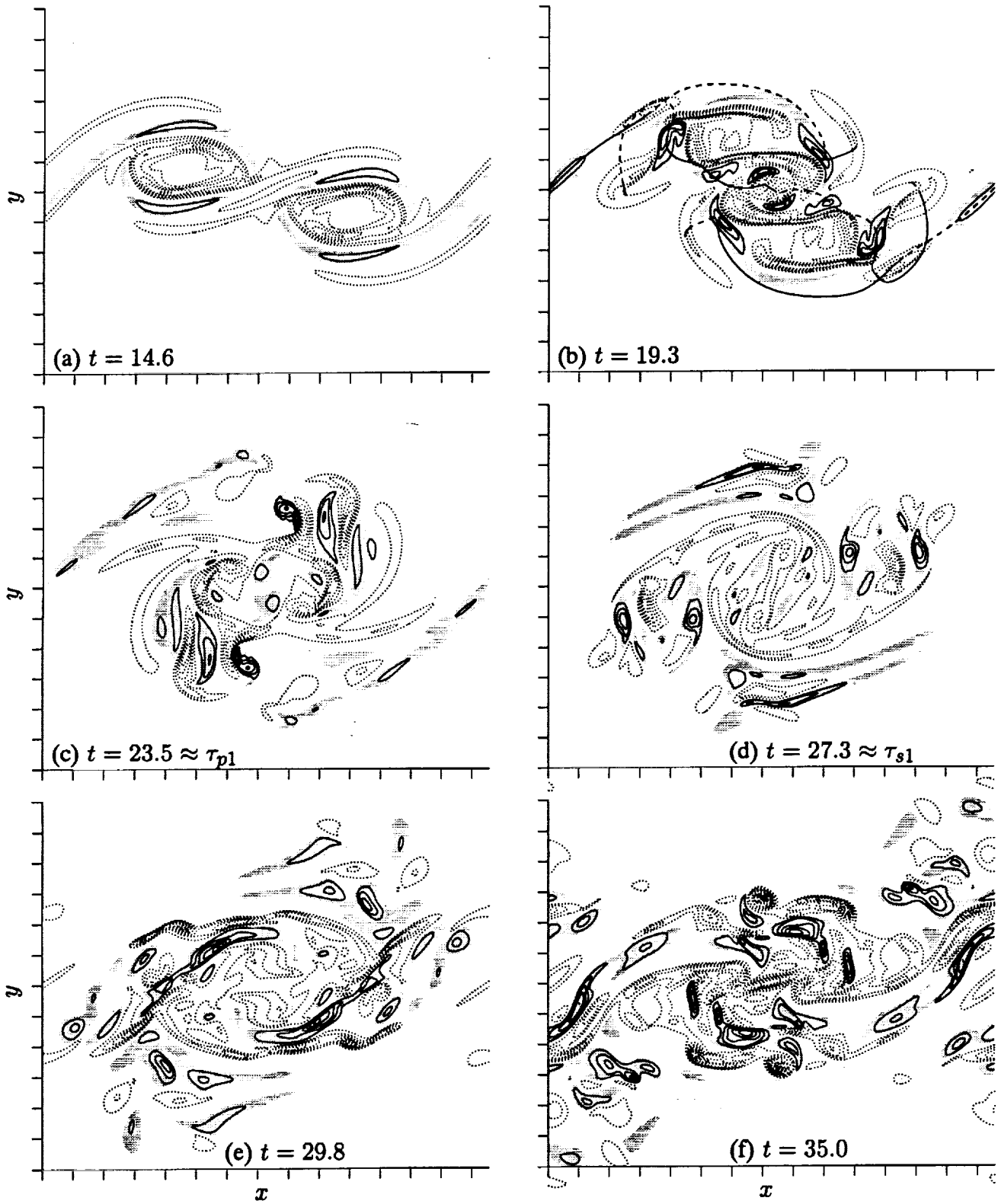

Figure 27. Contours of ω_z in the $z = \lambda_z/4$ RP of HIGH1P. The contour increments are (a,b,f) ± 0.6 and (c,d,e) ± 0.8 (approximately $1.65\Gamma_x^0/\delta_\omega^0$ and $2.20\Gamma_x^0/\delta_\omega^0$, respectively). Negative contour levels are dotted. Regions of positive spanwise vorticity are shaded. In (b) the heavy dark lines are rib vortex lines; they are dashed when the vortex line is behind the RP. Tic marks are at δ_ω^0 increments.

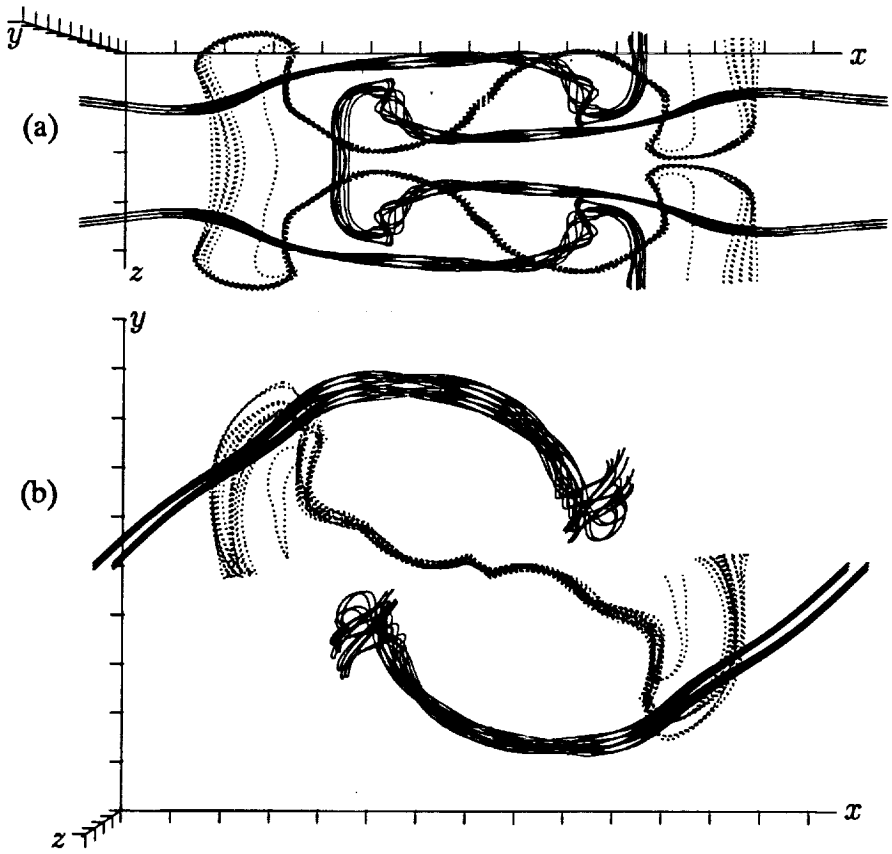

Figure 28. Vortex lines that pass through or near the symmetry points in the surviving (solid) and engulfed (dotted) ribs for HIGH1P at $t = 19.3$: (a) top view and (b) side view. Tic marks are at δ_ω^0 increments.

The correspondence of vorticity structures to the prepairing ribs and cups does not persist for long. By $t = 23.5 \approx \tau_{p1}$, the vorticity in the roller can no longer be described in terms of these original structures. Vortex lines through (and near) the symmetry point in the middle of the paired roller (fig. 29) no longer have the large excursions shown in figure 28, indicating that the topology of the vorticity has changed as a result of viscous reconnection. Thus, at this time, the vortex lines passing through the engulfed-rib symmetry point can no longer be identified as the engulfed rib. The cup structures are also not identifiable at this time, so the only persisting major features of the prepairing mixing layer are the surviving ribs. Vortex lines representing the surviving ribs at $t = 23.5 \approx \tau_{p1}$, $t = 27.3 \approx \tau_{s1}$, and $t = 31.1$ are shown in figures 29 and 30. At τ_{p1}, the main rib vortex lines are wrapped into the pairing roller, although they extend far above and below the roller. At the point of greatest excursion (in y) of the vortex lines, lines from neighboring ribs are being pinched together, allowing viscosity to reconnect them. This has been largely completed by τ_{s1} (fig. 30). At this time, the rib vortex lines again connect to the neighboring ribs far from the rollers through the wisp of spanwise vorticity shown in figure 26(d).

It is this wisp of spanwise vorticity that crosses the MP at τ_{s1}, leading to the circulation jump at that time. Thus, as in Part 1, the circulation jump at τ_{s1} occurs because the rib vortices are pulled over (or under) the roller into the neighboring braid region. When the vortex lines are pulled all the way through the MP (at about $t = 30$; fig. 30(b) is just after this), the circulation should have tripled,

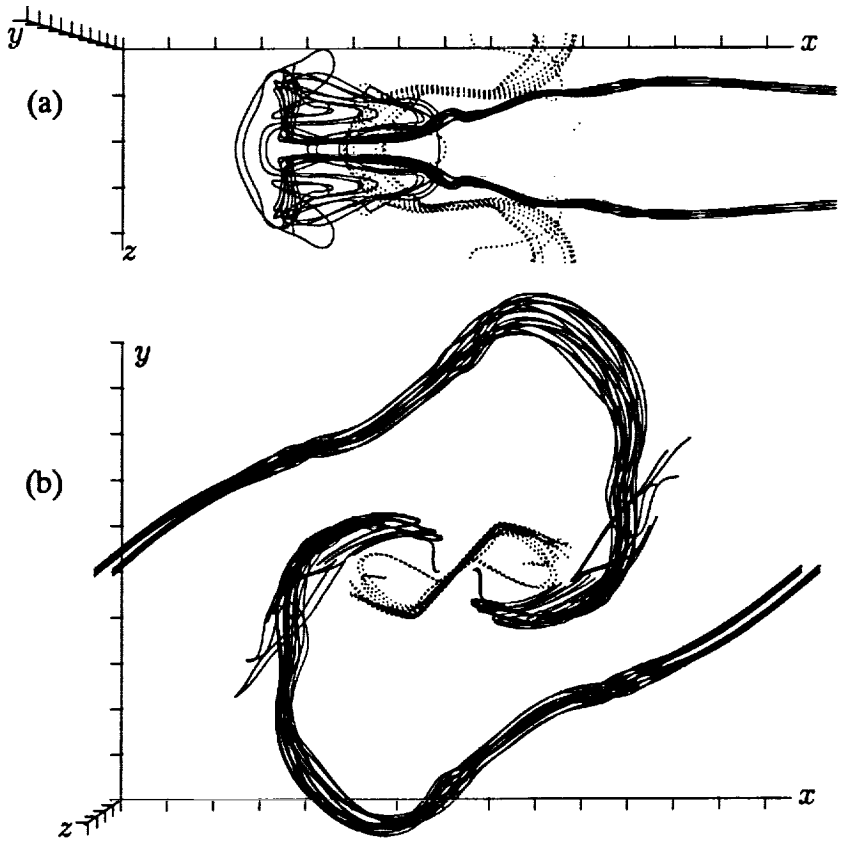

Figure 29. Vortex lines that pass through or near the symmetry points in the surviving (solid) and engulfed (dotted) ribs for HIGH1P at $t = 23.5 \approx \tau_{p1}$: (a) top view and (b) side view. Only one set (right side) of surviving ribs is included in (a). Tic marks are at δ_ω^0 increments.

since then vortex lines from three sets of ribs cross the MP (the original rib and the ribs from periodic images up- and downstream). The actual maximum circulation jump (from 2.05 before τ_{s1} to 6.33 at $t = 30$, see fig. 19(b)) is slightly more than a factor of three; thus, some core vortex lines must also have crossed the MP.

At $t = 30$, the mid-braid circulation (fig. 19(b)) reaches a maximum and begins a rapid decline. Like the circulation jump, this also is caused by spanwise vorticity entering the braid region, but in this case the vortex lines associated with it are kinked in a sense opposite to that of the rib lines. The spanwise vorticity structure that causes the circulation decline is apparent in figure 26(e) (the long, thin sheet of spanwise vorticity in the lower left portion of the domain). It is not surprising that these vortex lines are kinked in the opposite sense of the ribs, since most of the prepairing core vortex lines are kinked in this way.

5.2.2 Formation and evolution of vortex sheets– The thin sheets of spanwise vorticity that form in the BP become very long and wide compared to their thicknesses. For example, the boxed region in figure 26(e) has been magnified in figure 31(a), along with a z-y cross section through the right roller in that region. Since this is essentially a two-dimensional vortex sheet, it is no surprise that it is undergoing a Kelvin-Helmholtz roll-up, as noted in Moser and Rogers (1991). The velocity profile averaged in x over the extent of the box in figure 31(a) is shown in figure 32. The average velocity

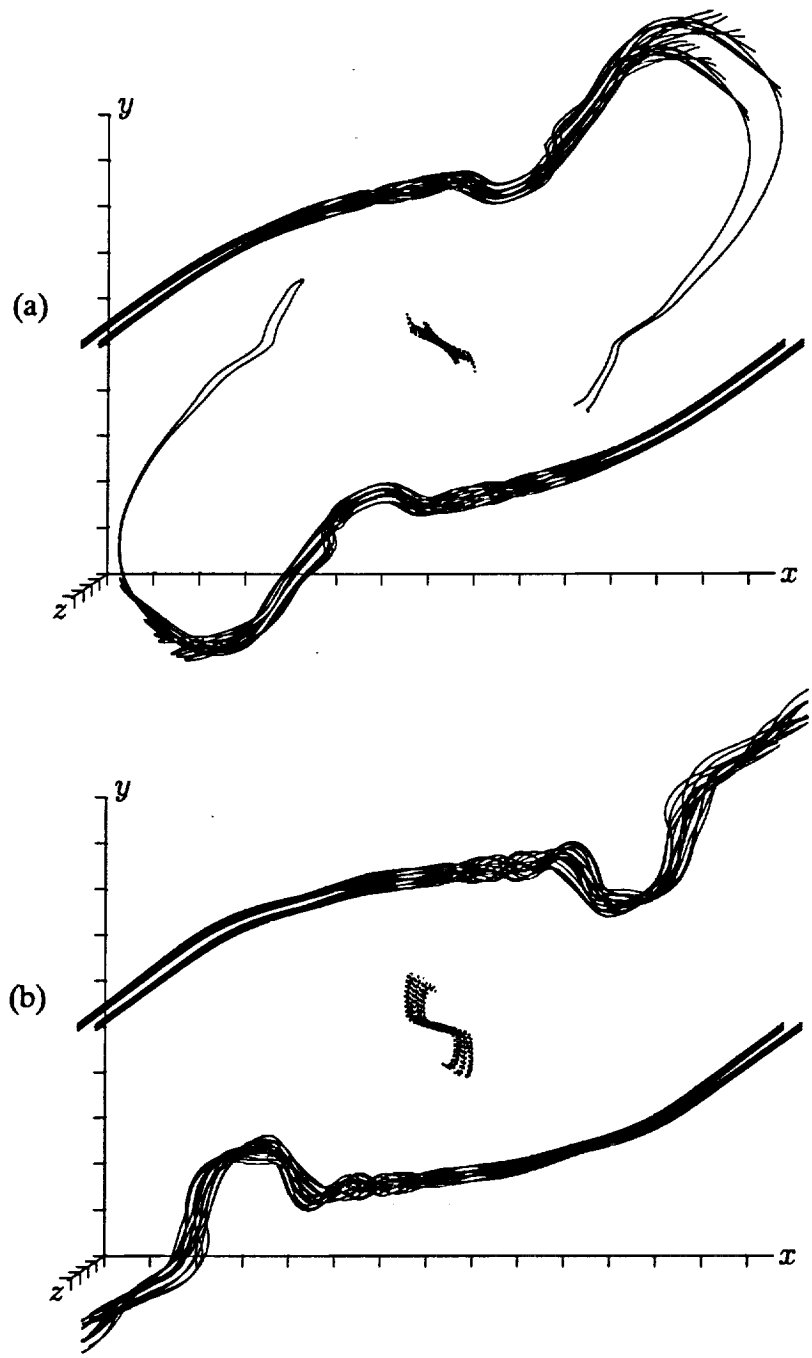

Figure 30. Vortex lines that pass through or near the symmetry points in the surviving (solid) and engulfed (dotted) ribs for HIGH1P at (a) $t = 27.3 \approx \tau_{s1}$ and (b) $t = 31.1$. Tic marks are at δ^0_ω increments.

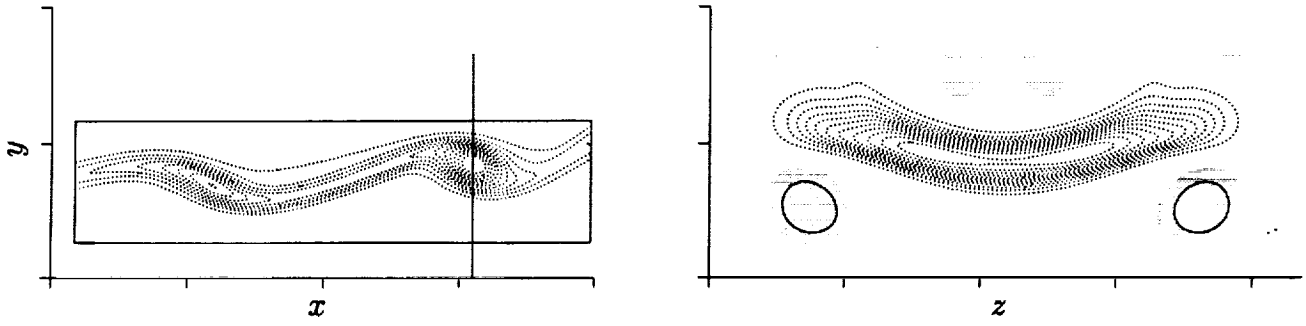

(a) Enlargement of box in figure 26(e) (b) z-y plane through the vertical line in (a)

Figure 31. Contours of ω_z. The contour increment is ± 0.8 and negative contours are dotted. Regions of positive ω_z are shaded and tic marks are at δ_ω^0 increments. The domain is $7 \leq x \leq 11$, $-3 \leq y \leq -1$, and $0 \leq z \leq \lambda_z$.

jump across this mini-mixing layer is approximately 0.8, and the vorticity thickness is approximately 0.27.[12] The most unstable wavelength of such a shear layer is about 2.0, which is in good agreement with the spacing between the forming rollers in figure 31(a). This secondary roll-up of the internal shear layer continues until, by $t = 35$, individual rollers have developed (the two rollers in the bottom of the domain of fig. 26(f)). At this time there are also other internal shear layers that are beginning to roll up (see fig. 26(f)). The formation of thin, internal shear layers in the BP and their subsequent roll-up increases the complexity of the flow and contributes to the cascade to small scales and the development of turbulence.

According to equation (18), the only way that spanwise vorticity can be amplified in the BP is by stretching in the z direction. This stretching must therefore be responsible for the formation of the thin sheets of spanwise vorticity discussed above. In the case of the thin sheet that is shown rolling up in the box in figure 26(e), this strain is primarily due to the surviving rib vortices. At $t = 27.3 \approx \tau_{s1}$, when the vortex sheet is forming (see fig. 26(d)), the surviving rib vortices and some core streamwise vorticity form a stagnation point in the BP near the position of the forming vortex sheet (see fig. 33). Note that the large regions of streamwise vorticity at the bottom of the domain in figure 33(b) are the surviving rib vortices. This quadrupole produces a persistent, coherent strain that produces the thin sheets of spanwise vorticity. Other thin sheets that form in the roller core are similarly produced by coherent strain in the BP, but the complexity of the core precludes associating these coherent strain regions with known structures. In the more complex flows described in section 6, the formation of thin sheets and their secondary roll-up is a prominent feature of the BP spanwise vorticity.

6 MULTIPLE PAIRINGS

It was observed in section 5.2 that if a mixing layer is sufficiently three-dimensional, a transition to turbulence can be initiated by a pairing. To allow such a transition to be completed, flows with two pairings have been simulated. In addition, we wish to determine if, for flows with weaker three-dimensionality, a transition might be triggered by the second pairing. This might be expected, since the level of three-dimensionality increases after the first pairing (see section 4.1). Three cases with

[12]The unaveraged velocity jump across the internal shear layer is as high as 1.3 at the right roll-up in figure 31(a).

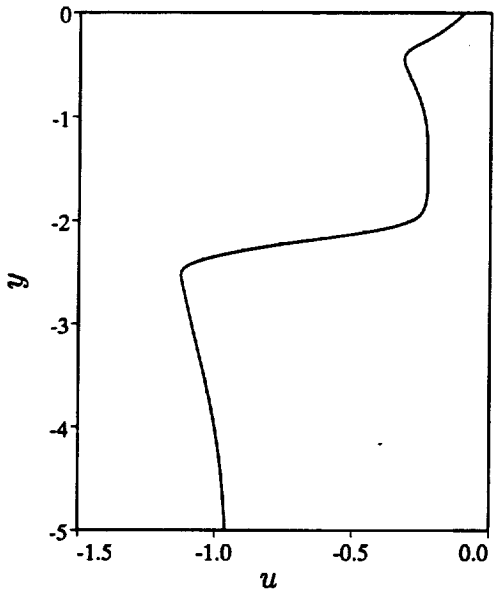

Figure 32. Streamwise velocity profile as a function of y in the BP, averaged over the x-domain defined by the box in figure 26(e) and figure 31(a).

different initial levels of three-dimensionality were simulated (LOW2P, MID2P, and HIGH2P). LOW2P has an initial circulation comparable to that of LOW1P, HIGH2P has an initial circulation comparable to HIGH1P, and MID2P is intermediate between these two (see table 2). For historical reasons, initial disturbances for these cases have different functional forms than those of the flows discussed in the previous sections. These differences in form were shown in Part 1 to cause no qualitative, and only slight quantitative, differences in the evolution of flow.

6.1 Weakly Three-Dimensional Double Pairings

Since the LOW2P flow has initial three-dimensionality similar to that of LOW1P, it is expected to be equally well predicted by linear analysis (see section 5.1). This is indeed the case, as can be seen in figures 34(a) and 34(b), where the normalized three-dimensional amplitude A^*_{3D} and the normalized circulation Γ^*_x are plotted. As with LOW1P, there are only insignificant departures from linearity before $\tau_{p1} = 21.1$; however, both the timing of the circulation jump at $\tau_{s1} \approx 33$ and the new plateau level reached after the jump in LOW2P are noticeably different from those derived through linear analysis. In addition, A_{3D} begins to diverge from the linear evolution at $\tau_{p2} = 40.0$. In the MID2P flow, Γ^*_x exhibits a larger departure from linear analysis after τ_{s1}, and A_{3D} begins to diverge from the linear evolution sooner (at $\tau_{p1} = 21.1$). In contrast, HIGH2P diverges from the linear A_{3D} evolution by about $t = 5$. Further evidence of the low level of the LOW2P three-dimensionality is provided by the Lin and Corcos collapse parameter ($\mathcal{L}$) and the momentum thickness evolution (figs. 34(c) and 34(d)). In LOW2P, the rib-collapse criterion is not satisfied until $t \approx 25$, well after the first pairing, even though collapse of the ribs is one of the first nonlinear processes to occur (see section 5.1). The momentum-thickness evolution of LOW2P is similar to that of the corresponding two-dimensional flow.

Also in agreement with the behavior of LOW1P, the LOW2P vorticity structures show only limited effects of nonlinearity. At $t = 54.7 \approx \tau_{s2}$, the ribs in LOW2P have collapsed, in agreement with the

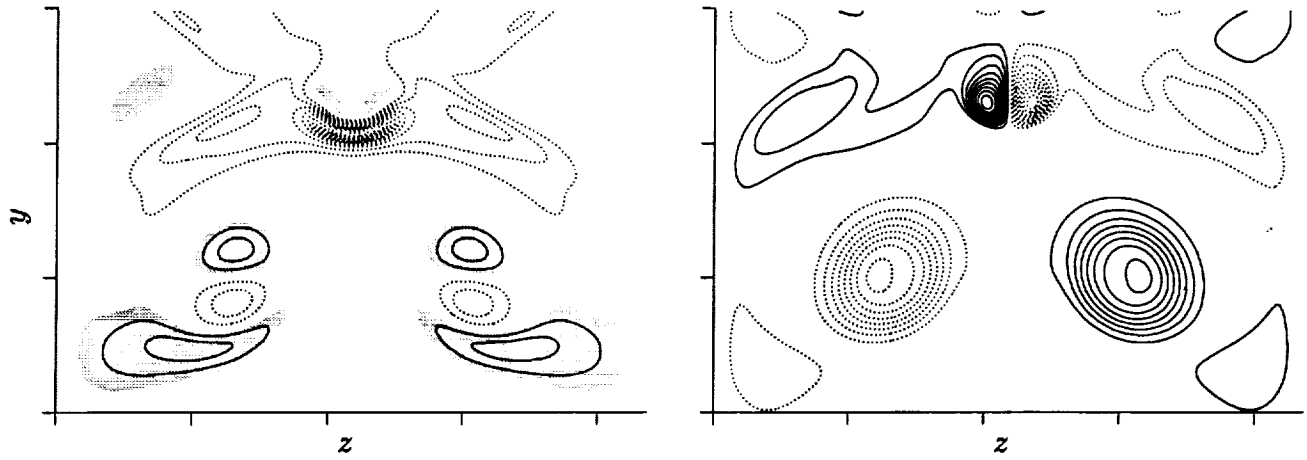

(a) Contours of ω_z (b) Contours of ω_x

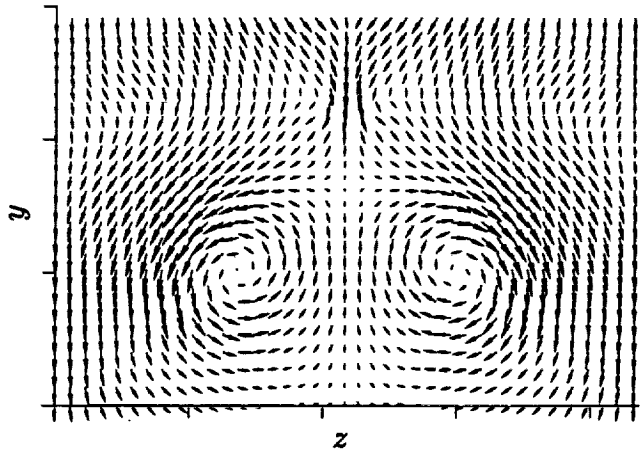

(c) Velocity vectors

Figure 33. The HIGH1P flow in the z-y plane passing through the vertical line in figure 26(d). The contour increment is ± 0.6, negative contours are dotted, and in (a), regions of positive spanwise vorticity are shaded. The y-domain depicted is from -4 to -1. Tic marks are at δ_ω^0 increments.

theory of Lin and Corcos (1984). Because of the collapse, the regions of rib streamwise vorticity shown in figure 35(d) are thicker than those associated with the linear results shown in figure 35(b). Also, the thin layers of perturbation spanwise vorticity present in the linear case (fig. 35(a)) are eliminated from the braid region in LOW2P. The structure of the core of LOWP2 is qualitatively similar to the corresponding linear-analysis results, although the details are different. Notably absent from LOW2P are the isolated, thin shear layers that formed in HIGH1P and led to secondary Kelvin-Helmholtz roll-ups (this was determined by examining the total ω_z as well as ω_z^{3D}).

In the MID2P case at this time ($t = 54.7 \approx \tau_{s2}$), there are more signs of nonlinear development (figs. 35(e) and 35(f)). The ribs are more strongly collapsed and, relative to the initial strength of the three-dimensional perturbation, the perturbation spanwise vorticity is weaker. In addition, the perturbations in the core have a more compact structure than those predicted by linear analysis and those in LOW2P.

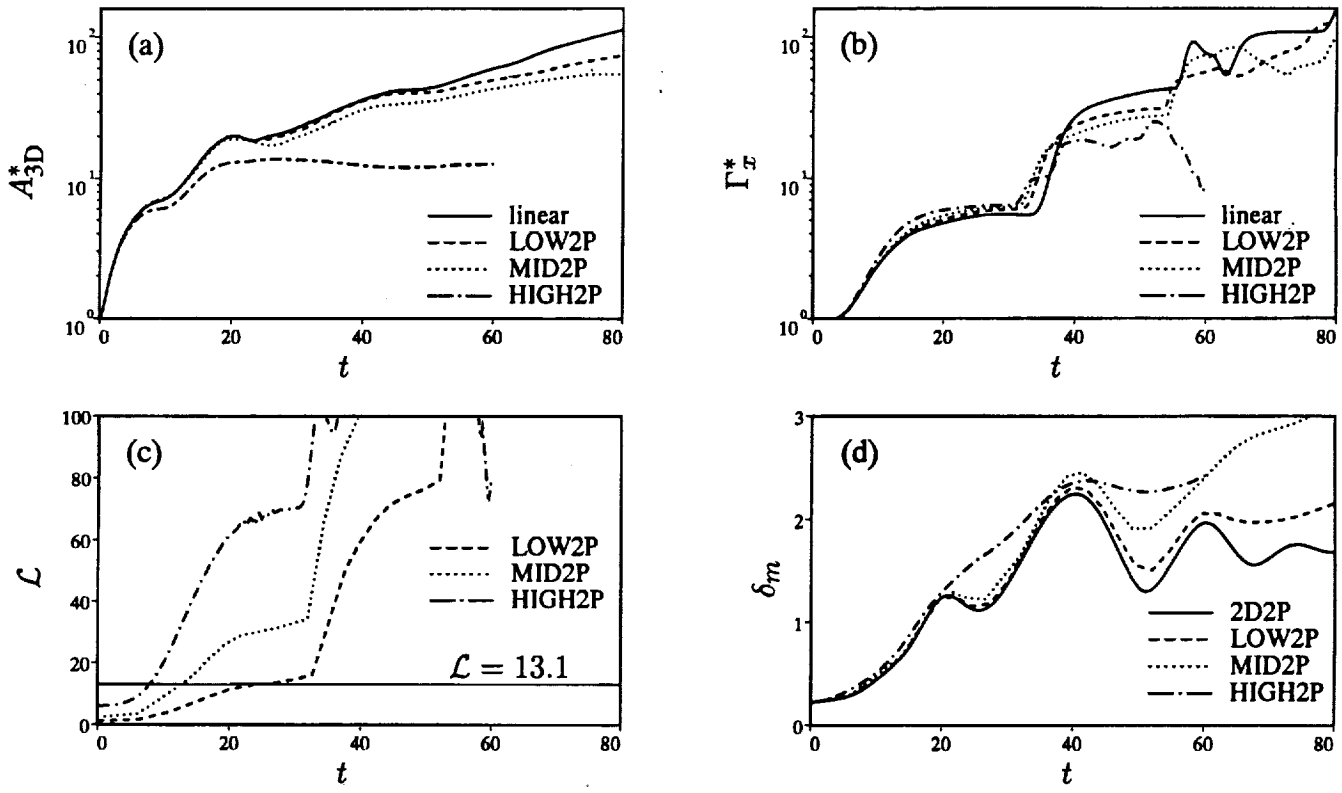

Figure 34. Time development of (a) A^*_{3D}, (b) Γ^*_x, (c) Lin and Corcos collapse parameter, $\mathcal{L}$, and (d) momentum thickness, δ_m.

The initial three-dimensionality of MID2P is approximately 2.5 times weaker than that of HIGH1P or HIGH2P. As a consequence, transition is not initiated at the first pairing of MID2P. However, the three-dimensionality of MID2P increases by a factor of two or more between the first and second pairings, as measured by A_{3D} and Γ_x (fig. 34). Thus transition could conceivably be initiated at the second pairing. Contours of spanwise vorticity[13] in both the BP and the RP of MID2P at $t = 39.1 \approx \tau_{p2}$ and $t = 54.7 \approx \tau_{s2}$ are shown in figure 36. While some of the features in these figures show some similarity to those of the HIGH1P flow shown in figures 26 and 27 (e.g., the formation of some thin filaments of spanwise vorticity in the BP), MID2P is clearly not undergoing a transition to small-scale turbulence at this time. There is no indication of secondary roll-ups forming on the thin sheets of spanwise vorticity, and the spanwise vorticity in the RP remains fairly organized.

There are several possible reasons for the lack of transition in MID2P at the second pairing. First, the aspect ratio of the three-dimensional disturbances (ratio of spanwise scale to streamwise scale of the flow) is smaller by a factor of two at τ_{p2} than at τ_{p1} because no spanwise scale change has been allowed. This imposed small aspect ratio could inhibit the transition (although it will be seen in section 7.3 that the flow evolution changes very little in a spanwise domain four times as large unless strong $(0, \beta)$ subharmonics are included in the initial condition). Second, A_{3D} is not a particularly good basis of comparison when the thicknesses of the mixing layers being compared are substantially different (e.g., HIGH1P at τ_{p1} versus MID2P at τ_{p2}). This is because there is an implied length scale in the definition of A_{3D} (see section 2.2). A better measure in this case is $A_{3D}/\sqrt{\delta_m}$, which is plotted in figure 37

[13]Not the perturbation spanwise vorticity shown in figure 35.

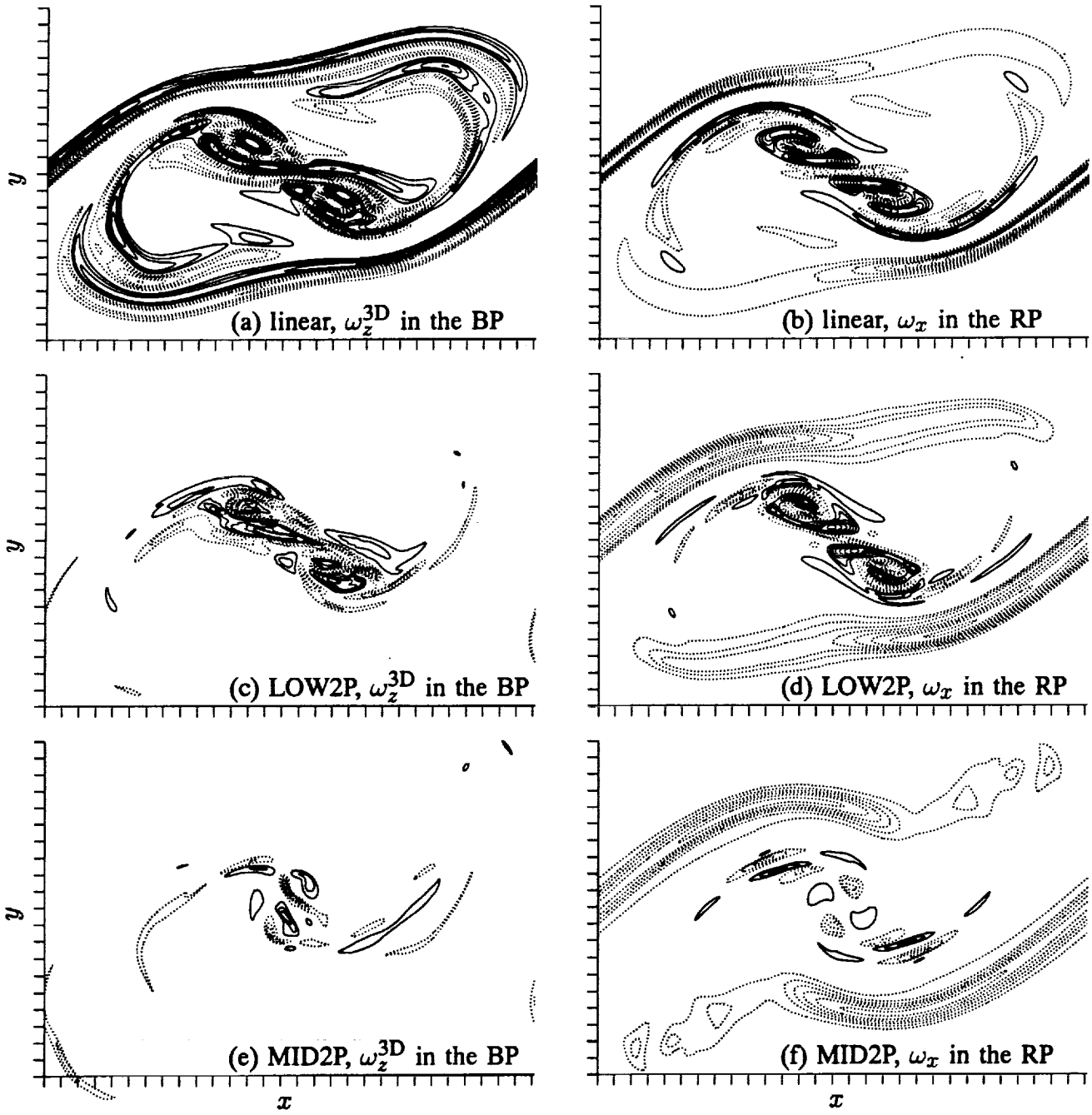

Figure 35. Contours of (ω_z^{3D}) and ω_x at $t = 54.7 \approx \tau_{s2}$. Contour levels are $\pm 3\Gamma_x^0/\delta_\omega^{0\,2}$, and negative contours are dotted. Tic marks are at δ_ω^0 intervals.

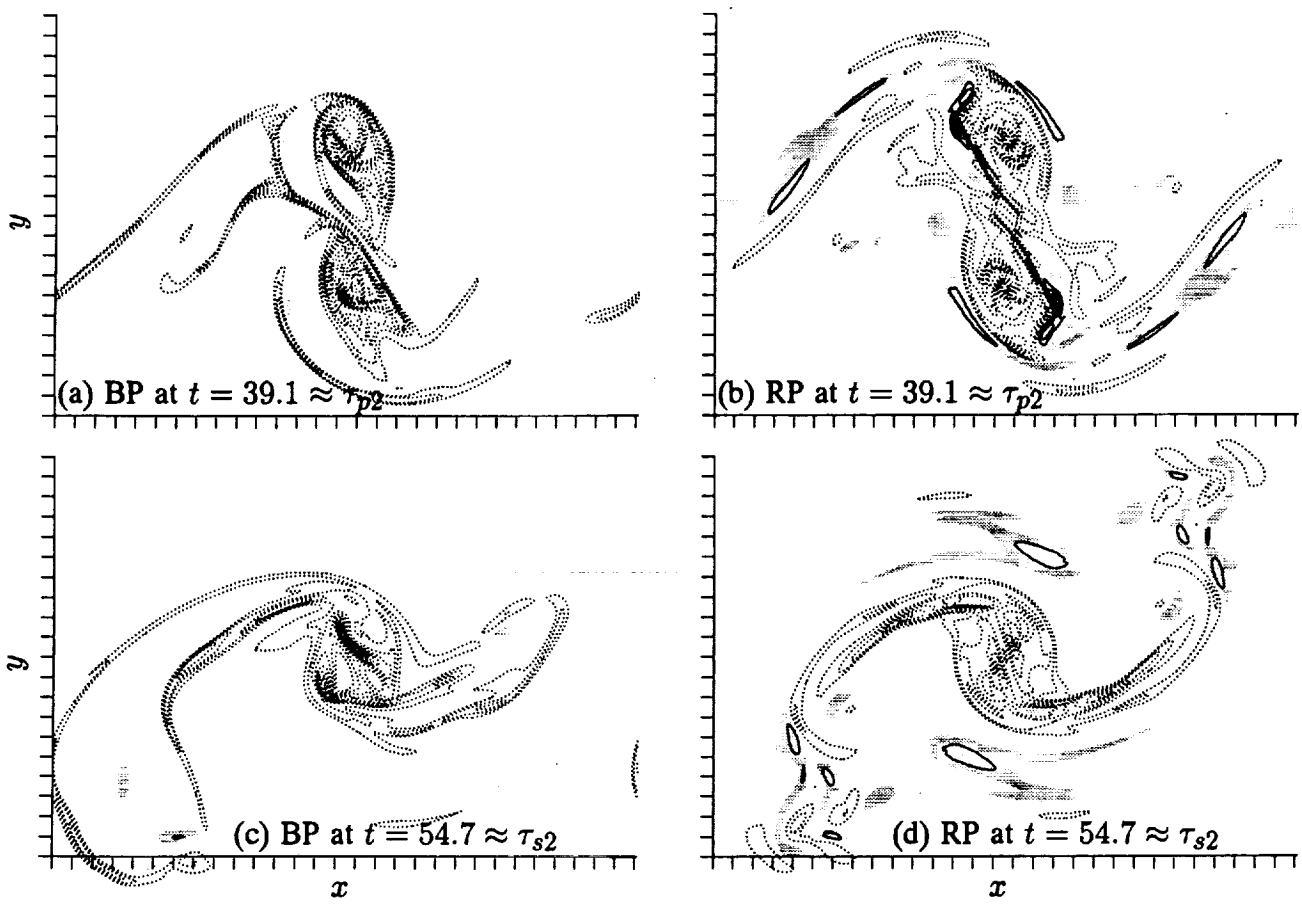

Figure 36. Contours of ω_z for MID2P. The contour increment is ± 0.3. Areas of positive spanwise vorticity are shaded, and negative contours are dotted. Tic marks are at δ_ω^0 increments.

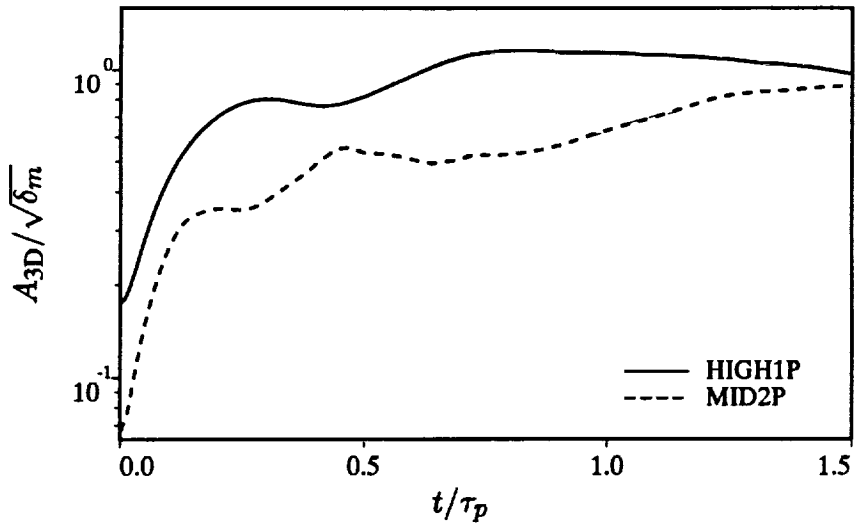

Figure 37. Time development of $A_{3D}/\sqrt{\delta_m}$ as a function of t/τ_p, for HIGH1P and MID2P, where τ_p is τ_{p1} for HIGH1P and τ_{p2} for MID2P.

for MID2P and HIGH1P.[14] By this measure, the three-dimensionality of MID2P at τ_{p2} is weaker by a factor of 1.8 than that of HIGH1P at τ_{p1}. Finally, there may be some subtle difference between MID2P and HIGH1P since MID2P has undergone a previous pairing. For example, in MID2P the roller cores have already paired once and therefore do not have the simple cup structures of unpaired rollers.

The MID2P flow is sufficiently three-dimensional for the rib vortex lines to be pulled all the way over the double-paired roller. This is illustrated in figure 38. As in HIGH1P, the rib vortex lines become distorted and are brought together with those of neighboring ribs, allowing them to viscously reconnect. This has started to occur in figure 38(a) ($t = 59.7$). Note that the reconnection does not pinch off the heads of the hairpin vortices, as was the case in HIGH1P. Instead, each rib reconnects with its other neighbor (fig. 38(b)), which makes the head of the resulting hairpins have spanwise vorticity of opposite sign (positive). The sense (or direction in z) of the rib vortex lines has thus been reversed. This reconnection results in a region of strong positive spanwise vorticity in the BP (fig. 39). This positive vorticity is sheet-like at $t = 65.0$, but by $t = 76.1$ (fig. 39(b)) it is concentrated in a very compact "roller." The rib vortex line reconnection depicted in figure 38 is neither the first nor the last to occur in MIDP2. At $t \approx 35$ (before the reconnection shown in fig. 38), the rib vortex lines reconnect as in HIGH1P, preserving the sense of the rib vortex lines. After the reconnection shown in figure 38, further reconnections occur, some of which change the sign of the vorticity in the tip region connecting the ribs and some of which preserve it.

6.2 Highly Three-Dimensional Double Pairing

As with HIGH1P, transition to small-scale turbulence is initiated at the first pairing (τ_{p1}) in HIGH2P. This can be observed in figures 40 and 41, where spanwise vorticity in the BP and RP of HIGH2P at four times (two of which are within the period illustrated in figs. 26 and 27) are shown. Clearly, the same interaction of the cups in the pairing rollers is occurring, leading to the formation of thin shear layers, secondary roll-ups in the BP, and small-scale granularity in the RP (see section 5.2). As the second pairing proceeds, the complex, transitioning rollers are brought together. The structures in each roller can then interact, increasing the complexity of the double-paired roller. By $t = 39.1 \approx \tau_{p2}$ (figs. 40(c) and 41(c)), the prepairing structure is no longer discernible. Thin sheets and secondary roll-ups in the BP, and small-scale granularity in the RP, which characterize the flow at τ_{p1}, are also present at τ_{p2}. Later ($t = 52.1$; see figs. 40(d) and 41(d)), secondary roll-ups continue and there is enhanced turbulence activity in the braid region, especially in the RP, while the turbulence in the core appears to be decaying.

The onset of turbulence is accompanied by the continuous entry of spanwise vorticity into the braid region (see figs. 40 and 41), even before τ_{p2}. Thus the process described in section 3.1, by which pairing leads to reentry of spanwise vorticity into the braid region, is no longer relevant. There is no τ_{s2} in this case (see table 2). Also, since the braid region is turbulent, the circulation Γ_x can no longer be taken to be the rib circulation.

As would be expected for a turbulent flow, many features of HIGH2P are qualitatively different from those of nontransitional flows. For example, a comparison of the spanwise vorticity of HIGH2P and MID2P at $t = 39.1 \approx \tau_{p2}$ (see figs. 36, 40, and 41) reveals no similarity; HIGH2P is clearly

[14]The momentum thicknesses for HIGH1P and MID2P are plotted in figure 23(c) and figure 34(d), respectively.

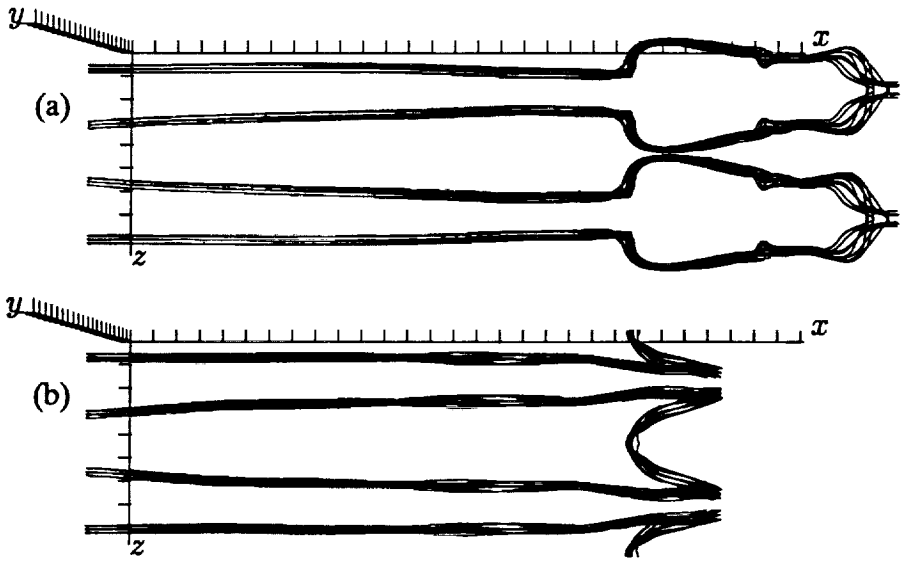

Figure 38. Top view of vortex lines that pass through or near the symmetry points in the surviving ribs for MID2P at (a) $t = 59.7$ and (b) $t = 65.0$. The domain has been periodically extended in the spanwise direction to show two pairs of ribs. Tic marks are at δ_ω^0 intervals.

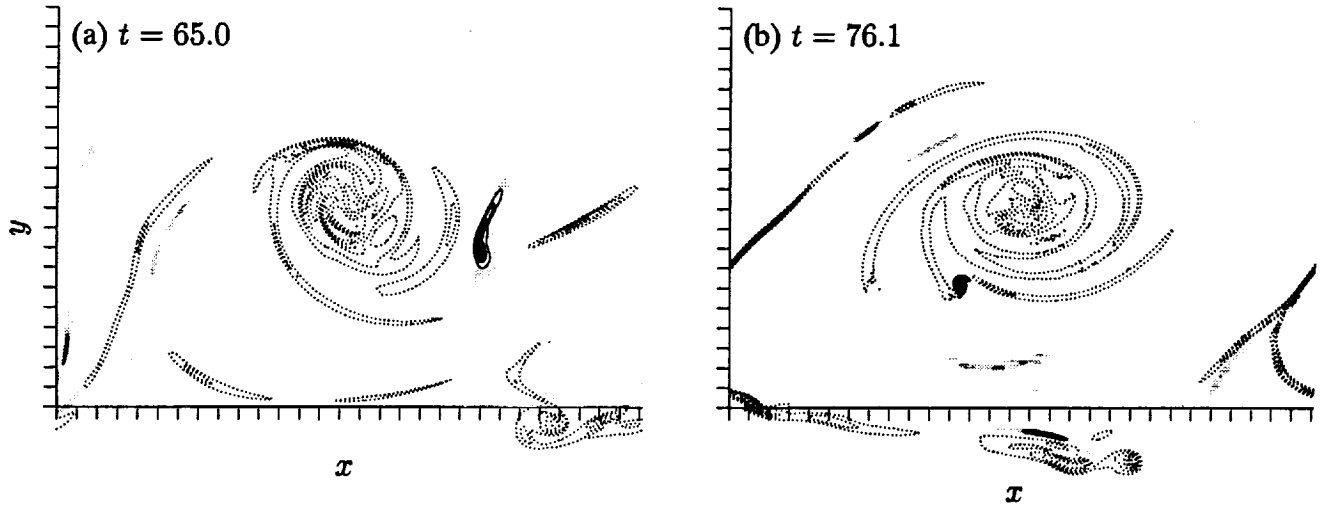

Figure 39. Contours of ω_z in the BP of MID2P. Vortex lines shown in figure 38(b) pass through the region of intense positive vorticity in (a). The contour increment is ± 0.3 and the peak level of positive ω_z is 2.80 in (a) and 4.53 in (b). Regions of positive vorticity are shaded and negative contours are dotted. Tic marks are at δ_ω^0 intervals.

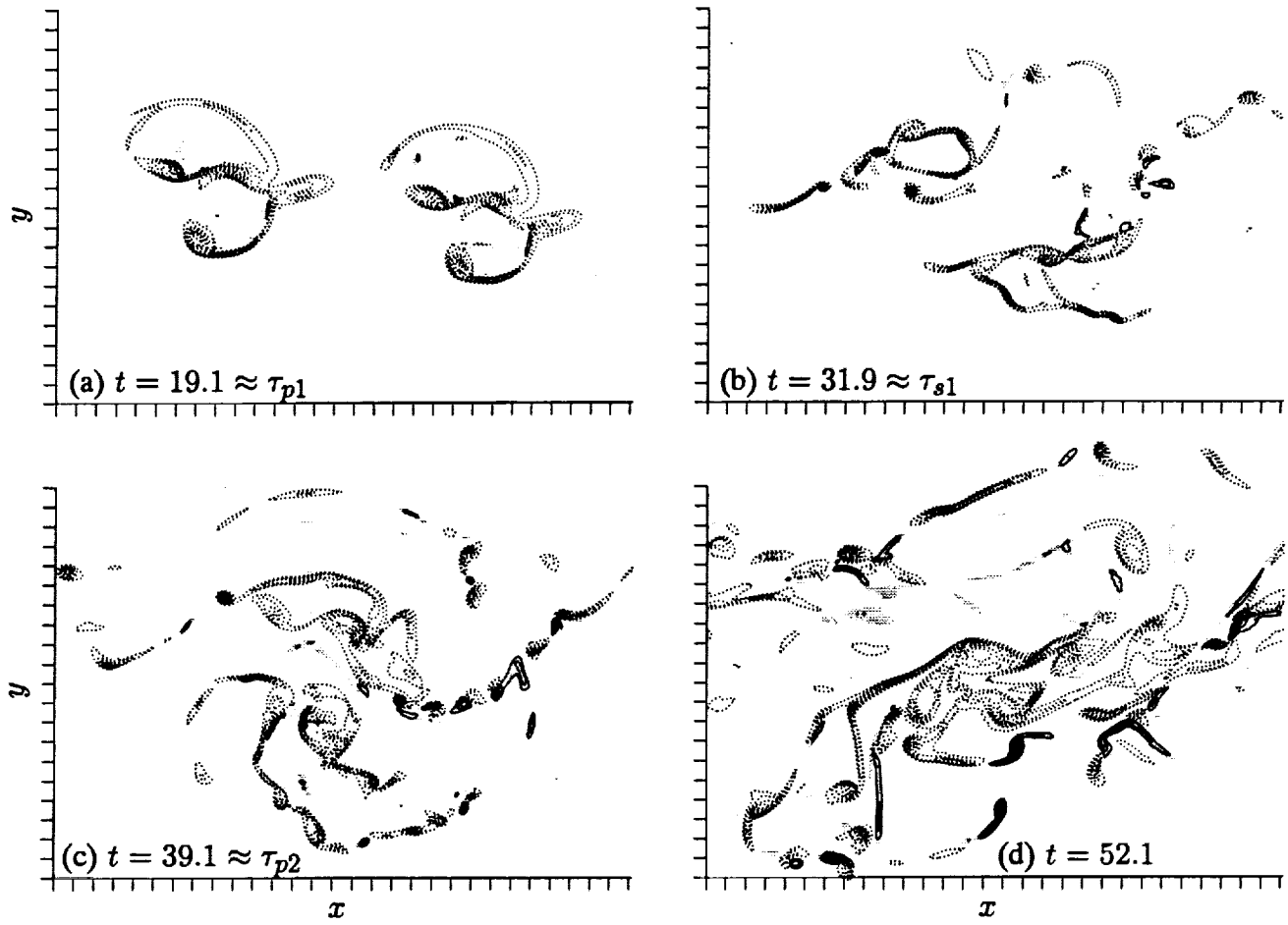

Figure 40. Contours of ω_z in the BP of HIGH2P. The contour increments are (a) ± 0.6, (b) ± 0.8, (c) ± 0.5, and (d) ± 0.3. Regions of positive vorticity are shaded and negative contours are dotted. Tic marks are at δ_ω^0 intervals.

turbulent, while MID2P is not. The structures of the passive scalar fields present in these flows are also qualitatively different (fig. 42). Scalar interfaces in HIGH2P are highly distorted with many small-scale features, while those in MID2P are smooth and regular. This suggests that a flow visualization of HIGH2P based on passive markers would appear turbulent. There has also been more molecular mixing of the scalar in the HIGH2P flow than in MID2P (see section 8). Finally, the presence of turbulence produces a steadier growth of the mixing layer than in the nontransitional flows (see fig. 34(d)). The oscillations in the thickness of the layer (caused by the pairings) have been largely eliminated, consistent with the monotonic growth expected of a fully turbulent layer. The characteristics of post-transitional turbulent mixing layers will be examined further in section 8.

7 SPANWISE SCALE CHANGE

In the flows discussed in the preceding sections, the spanwise scale was constrained to be $\lambda_z = 0.6\lambda_x$. This scale was selected based on the linear analysis of section 4.2, which suggested that this was the wavelength of the fastest-growing disturbance. Also, it was found that the linear mechanism by which the dominant spanwise wavelength could change was very slow. However, this observation

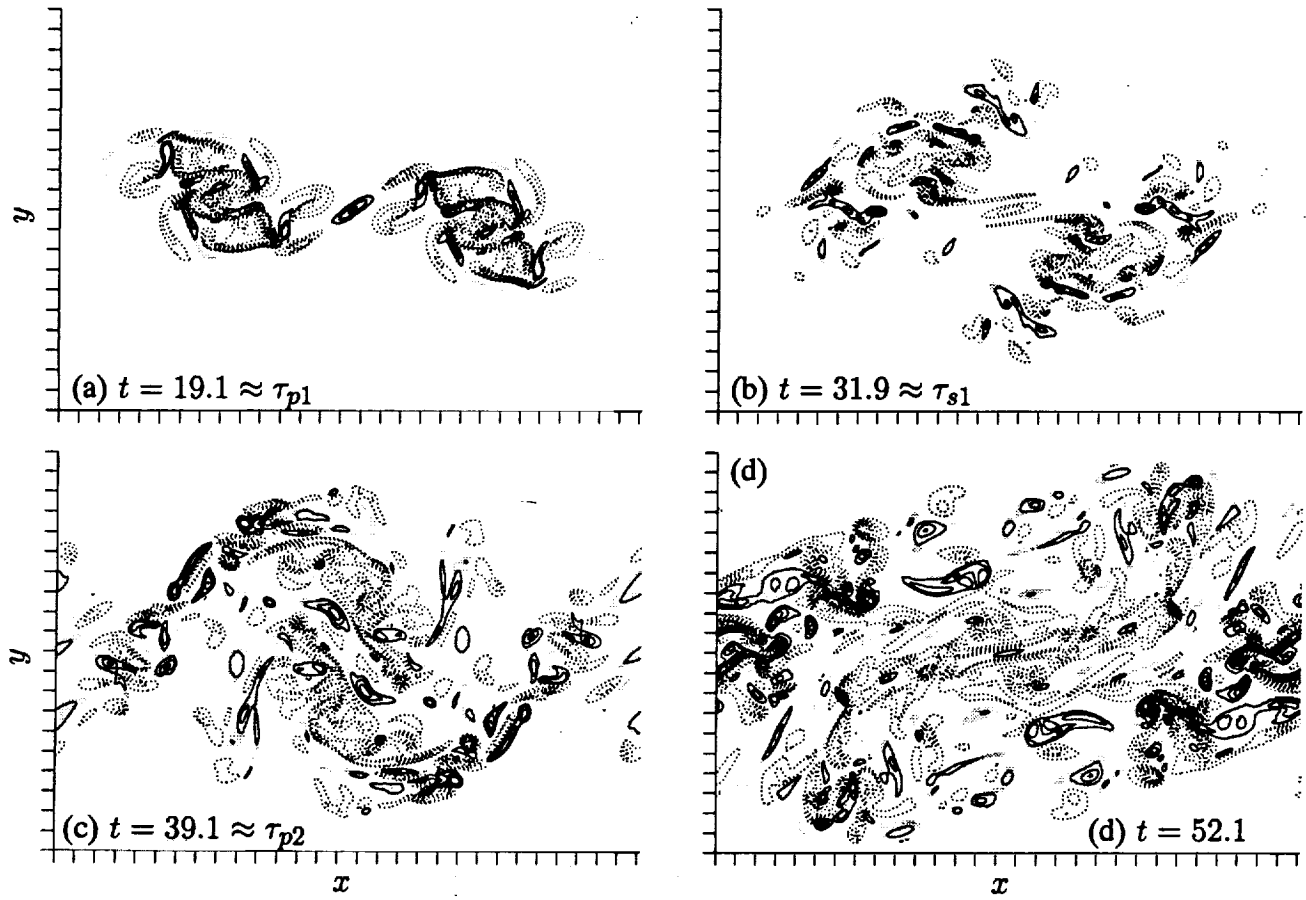

Figure 41. Contours of ω_z in the RP of HIGH2P. The contour increments are (a) ± 0.6, (b) ± 0.8, (c) ± 0.5, and (d) ± 0.3. Regions of positive vorticity are shaded and negative contours are dotted. Tic marks are at δ_ω^0 intervals.

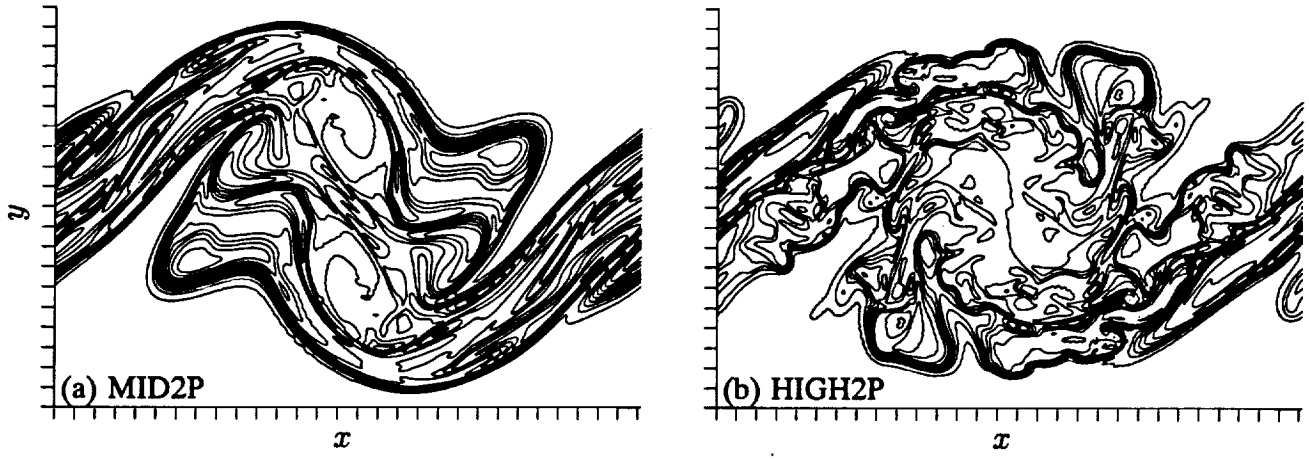

Figure 42. Contours of the passive scalar in the BP at $t = 39.1 \approx \tau_{p2}$. The contour increment is 0.08, from 0.02 (bottom) to 0.98 (top), and tic marks are at δ_ω^0 increments.

is different from the (nonlinear) experimental results of Huang and Ho (1990), which suggest that the dominant spanwise scale should double after each pairing. In this section we investigate nonlinear mechanisms that could hasten a scale change. In particular we would like to determine the cause of the discrepancy between the experimental results of Huang and Ho (1990) and those of Bernal and Roshko (1986), who found that a spanwise scale change did not occur until the transition to turbulence. In addition, the extent to which the results discussed in the previous sections are affected by the spanwise scale restraint is examined.

Most of the flows discussed below are identical to those discussed in the previous sections, except that the spanwise subharmonic modes $(0, \frac{1}{2})$ and, in some cases, $(0, \frac{1}{4})$ are initialized (see table 2). When including these subharmonic modes, the phase of the subharmonics relative to the fundamental disturbance must be specified. Since there is no streamwise vorticity in the (0,0) mode, the range over which the subharmonic phase ($\phi_{0\frac{1}{2}}$; see eq. (11)) can be varied without including redundant cases is from 0 to $\pi/4$. The endpoints of this range represent extreme phasings, which have special properties discussed in section 7.2. For the second subharmonic, the nonredundant range of $\phi_{0\frac{1}{4}}$ is 0 to $\pi/2$. The values of $\phi_{0\beta}$ and the initial disturbance amplitudes $A_{0\beta}$ are listed in table 2 for each of the flows presented below.

Following the reasoning used in section 4.2, the dominant spanwise scale (Λ_z) is defined to be the wavelength λ_z/β ($\beta \neq 0$) associated with the maximum amplitude $A_{s\beta}$. By this definition $\Lambda_z = \lambda_z$ initially for all cases discussed here except for the TURB2P flow (described in detail in section 8), in which $\Lambda_z = 4\lambda_z$ at $t = 0$. A scale change is said to occur when Λ_z changes. Since the simulations have a finite spanwise domain not more than four times larger than λ_z, there are only a few discrete wavelengths near λ_z that can be represented in the simulation. Thus any scale changes that occur, must occur at discrete times. There can be no gradual change in Λ_z. The time τ_{sc} is defined to be the time at which such a scale change occurs. Note that scale change as defined here reflects a change in the energy in spanwise Fourier modes. Such a scale change does not necessarily imply a change from an array of rib vortices at one spacing to similar rib vortices at another spacing (see section 7.2).

7.1 Nonlinear Scale Change

The evolution of A_{s1} and $A_{s\frac{1}{2}}$ for the PH01P, PH$\frac{\pi}{4}$1P, and PH$\frac{\pi}{4}$0P simulations (see table 2) is shown in figure 43(a). A scale change occurs in each of these cases (even the nonpairing case, PH$\frac{\pi}{4}$0P) at times τ_{sc} of 31.5, 29.4, and 28.9, respectively. Scale change occurs first in the nonpairing case because the pairing suppresses the growth of $A_{s\frac{1}{2}}$. In the pairing cases, the two phasings have different scale-change times because at $t \approx 20$, the growth of $A_{s\frac{1}{2}}$ is delayed for PH01P. An intermediate phasing case (PH$\frac{\pi}{8}$1P) was also simulated (not shown in fig. 43); it had a scale-change time intermediate between that of PH01P and PH$\frac{\pi}{4}$1P ($\tau_{sc} = 29.9$).

The occurrence of scale change in these nonlinear cases is in contrast to the predictions of linear analysis in section 4.2, which indicate that such a scale change should not occur until after several pairings. This suggests that the scale change in these cases is essentially nonlinear. In figure 44, A^*_{s1} and $A^*_{s\frac{1}{2}}$ from PH$\frac{\pi}{4}$1P and PH$\frac{\pi}{4}$0P are compared with the corresponding linear results. The most important difference between the linear and nonlinear cases is that the nonlinear $\beta = 1$ mode has

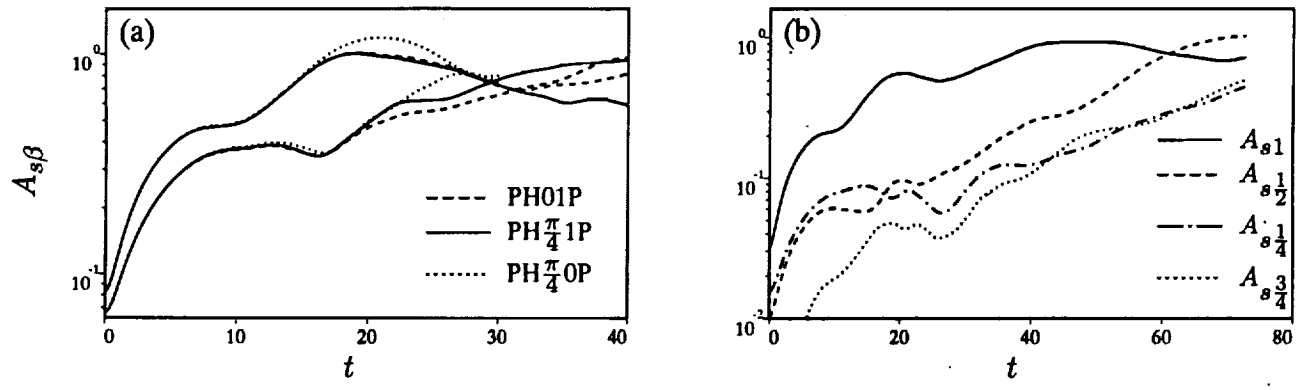

Figure 43. Time development of three-dimensional disturbance amplitudes ($A_{s\beta}$) for (a) PH01P, PH$\frac{\pi}{4}$1P, and PH$\frac{\pi}{4}$0P (upper 3 curves at $t = 10$ are A_{s1} and lower 3 are $A_{s\frac{1}{2}}$) and (b) WMID2P ($A_{s\frac{3}{4}}$ not initialized).

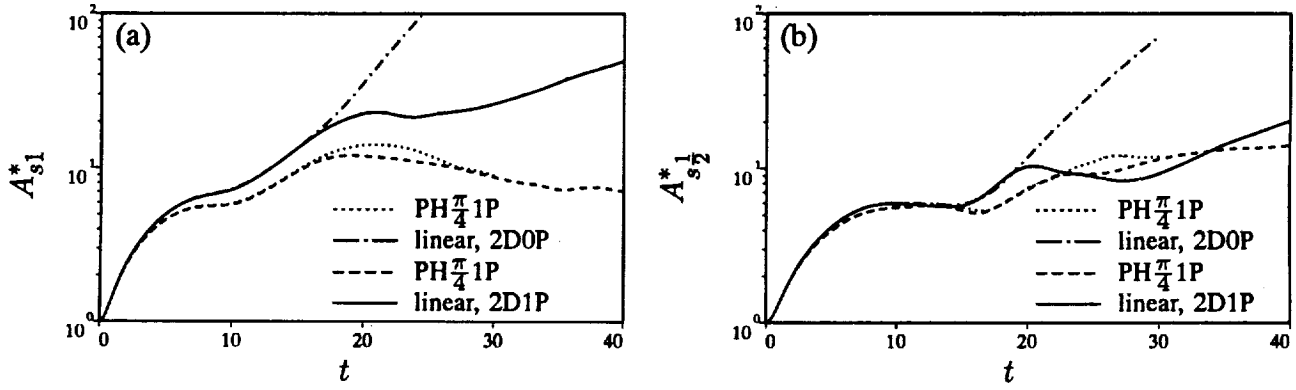

Figure 44. Time development of (a) A^*_{s1} and (b) $A^*_{s\frac{1}{2}}$.

saturated, as was observed in section 5.2. That is, A^*_{s1} does not grow beyond $t = 20$ and the growth prior to this time is less. This saturation occurs in the nonpairing case as well, even though the linear-analysis perturbations are undergoing post-τ_{o0} exponential growth (see section 4.1). In contrast, $A^*_{s\frac{1}{2}}$ does not stop growing, although it does evolve nonlinearly. $A^*_{s\frac{1}{2}}$ even exceeds the linear results around $t = 30$ in the pairing case. Thus it is the nonlinear saturation of the fundamental ($\beta = 1$) coupled with the continued growth of the subharmonic ($\beta = \frac{1}{2}$) that allows the spanwise scale to change. To confirm this, we examine WMID2P (fig. 43(b)), which has weaker initial three-dimensional disturbances that therefore saturate later. The scale change occurs much later in this case (after the second pairing, $\tau_{sc} = 61.0$), and only after A_{s1} has saturated.

7.2 Spanwise Scale-Change Mechanisms

To understand the mechanisms by which the spanwise scale changes, we must first examine the physical consequences of the different phasings of the subharmonics. When subharmonic $(0, \beta)$ modes are added, the resulting rib vortices are no longer of uniform strength. The initial patterns of rib-strength variation for $\phi_{0\frac{1}{2}}$ of 0, $\frac{\pi}{4}$, and $\frac{\pi}{8}$ are shown in figures 45(a), 45(d), and 45(g). The $\phi_{0\frac{1}{2}} = 0$ phase results in ribs of two strengths, arranged with a strong pair and a weak pair next to each other

(fig. 45(a)). This arrangement preserves the spanwise reflection symmetry (eq. (12)). The other extreme phasing ($\phi_{0\frac{1}{2}} = \frac{\pi}{4}$) produces ribs of three strengths: a strong and weak rib of the same sign and two opposite-signed, medium-strength ribs (fig. 45(d)). With this phasing, the point-reflection symmetry (eq. (13)) is preserved, with the symmetry points located in the middle of the strongest and weakest ribs. Intermediate phasings (e.g., $\phi_{0\frac{1}{2}} = \frac{\pi}{8}$, fig. 45(g)) result in a rib pattern intermediate between the above extremes, and have no symmetries.

Once the spanwise vorticity is largely removed from the MP, it might be expected that the MP rib locations would be largely determined by the net induced motion of each rib vortex on the rest of the ribs. The simulation results indicate that this is indeed the case and that the rib locations can be well predicted by such simple arguments.[15] In PH01P, the strong rib pair drives itself upward (for the sign shown in fig. 45(a)) and the weak rib pair moves downward. Once away from the centerline, the weaker ribs drive the strong pair together while being separated by the induced motion of the stronger ribs (figs. 45(b) and 45(c)). All of the ribs are prevented from moving too far from the centerline by the compressive strain component associated with the primary roller vortices. In PH$\frac{\pi}{4}$1P the rib motion is dominated by the strongest rib, which remains fixed at the same location by flow symmetry (as does the weakest rib). The two intermediate-strength ribs rotate around the strongest rib and, because of the induced motion of the weakest rib, spiral inwards (figs. 45(e) and 45(f)). As can be seen in figures 45(c), 45(f), and 45(i), this self-induced rib motion continues for some time after τ_{s1} despite the presence of additional vorticity in the MP. By $t = 35$ the intermediate-strength ribs in PH$\frac{\pi}{4}$1P (negative ω_x in fig. 45(f)) are directly above and below the strongest (positive) rib vortex. At this point, however, many new regions of significant ω_x are present in the MP; shortly after this the flow appears "turbulent," with little evidence of the original rib vortices. As expected, the PH$\frac{\pi}{8}$1P evolution (figs. 45(g)–45(i)) is intermediate between that of the other two extreme cases.

The above rib behavior suggests two possible mechanisms for a spanwise scale change. The first (mechanism I), associated with $\phi_{0\frac{1}{2}} = 0$, may result from viscous annihilation of the strong vortex pair, which is being compressed together. The second (mechanism II), suggested by the $\phi_{0\frac{1}{2}} = \frac{\pi}{4}$ results, occurs when the inwardly spiraling, intermediate-strength vortices viscously combine with the strongest rib and leave a weak rib with the same sign as the intermediate-strength pair. Both of these mechanisms depend on viscosity to be carried to completion and are therefore slow. In practice, even flows resulting from large $(0, \beta)$ initial disturbances will not complete this process before τ_{s1}.[16] Also both scale-change mechanisms result in *weak* rib pairs with twice the initial spanwise spacing. Thus, if this kind of scale change were carried to completion it would result in a reduction of three-dimensionality. It is instructive to note that mechanism II (associated with $\phi_{0\frac{1}{2}} = \frac{\pi}{4}$) results in Fourier-mode energies that indicate spanwise scale change long before the complete viscous combination of the three stronger ribs has occurred. In particular, when the intermediate-strength rib pair is situated directly above and below the strongest rib (fig. 45(f)), the spanwise variation is primarily accounted for by the $(\alpha, \frac{1}{2})$ modes. In this state $A_{s\frac{1}{2}} > A_{s1}$ (see fig. 43(a)). Caution must therefore be used in drawing conclusions about the structures present in a flow based on the occurrence of the scale change given by Fourier-mode energies.

[15] Note that an array of uniform-strength ribs do not move from their MP locations at $y = 0$ (see section 5).

[16] Weaker initial disturbances that do not result in collapsed ribs show minimal rib movement prior to τ_{s1}.

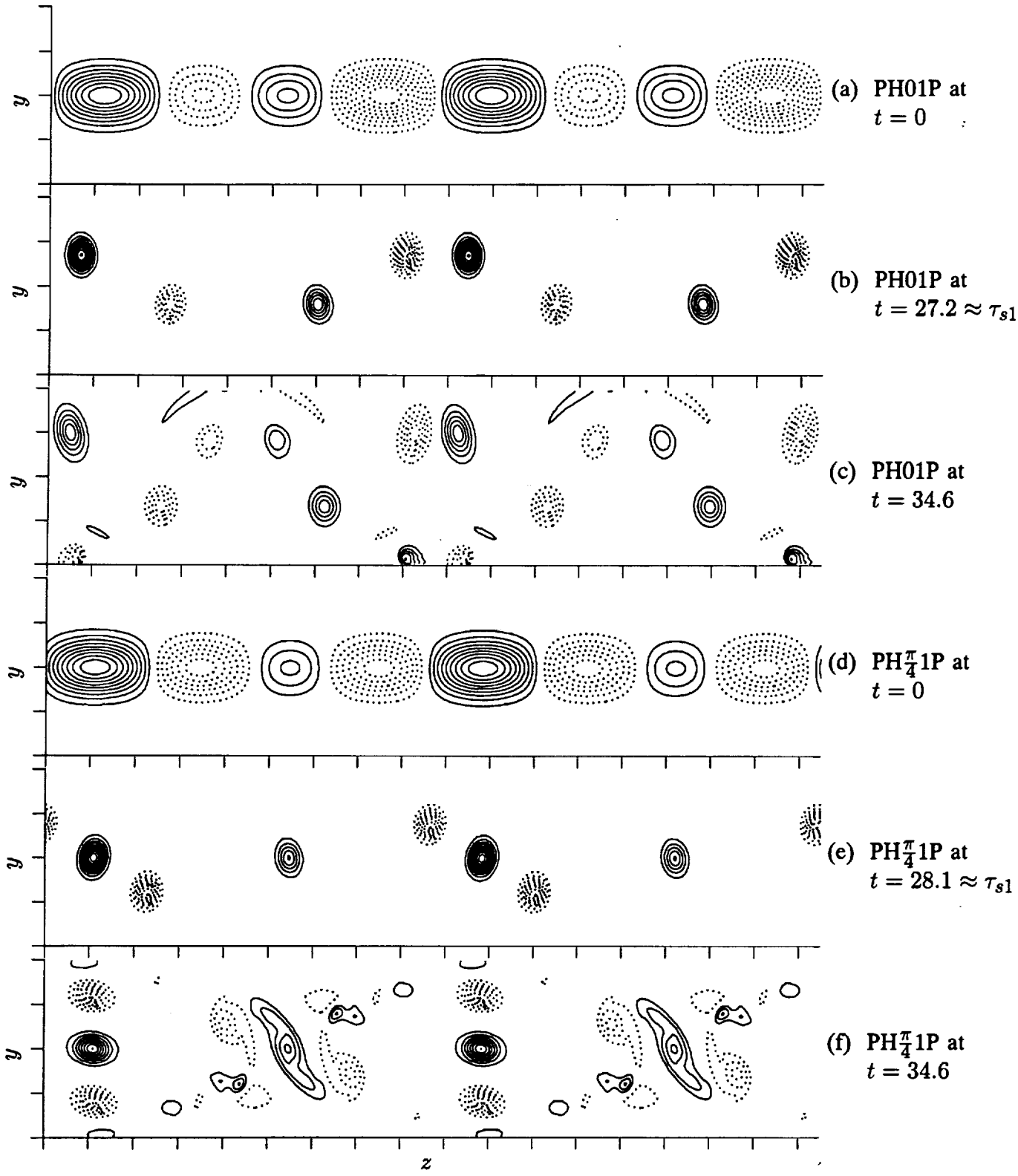

Figure 45. For caption see next page.

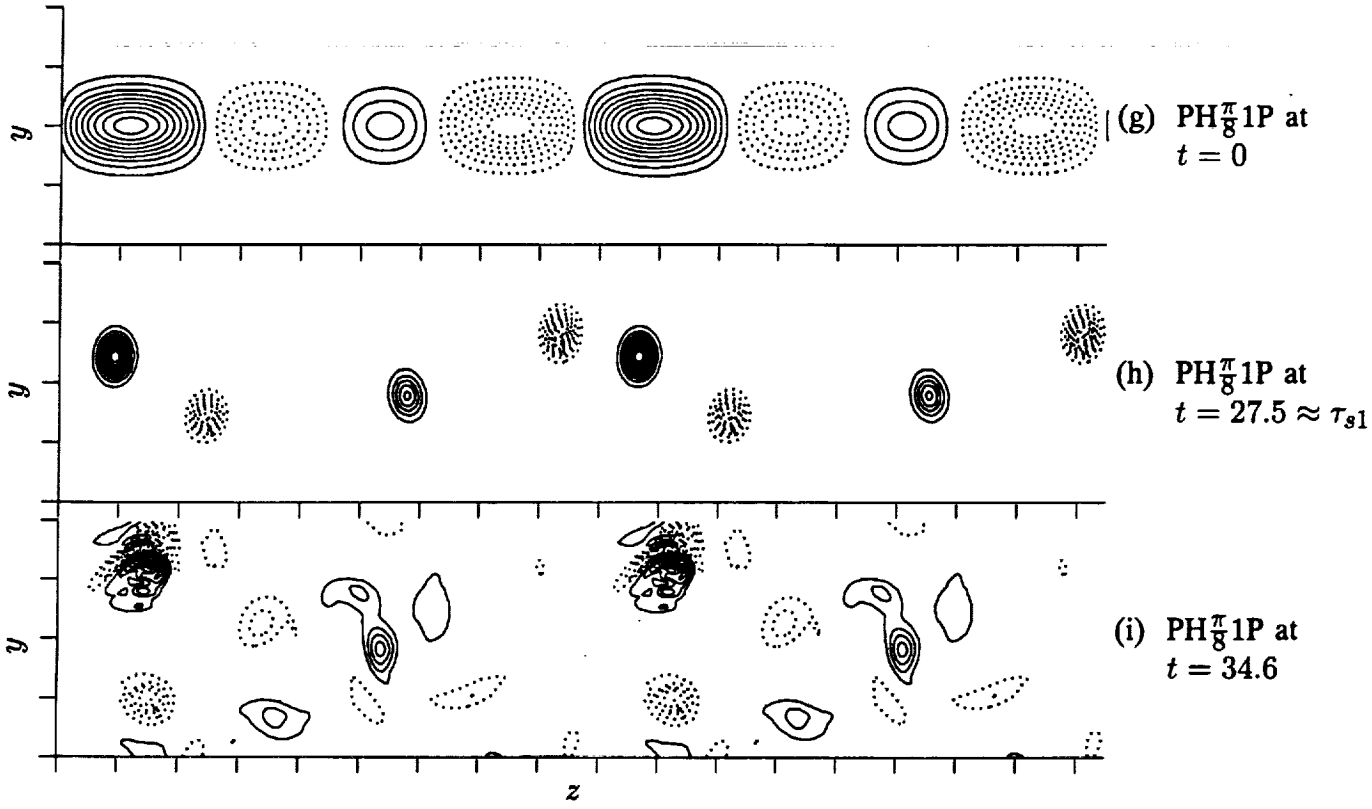

Figure 45. Contours of ω_x in the MP. The contour increment is ± 1.0 except for (a), (d), and (g) ($t = 0$), where it is ± 0.04. Solid contours indicate positive vorticity, dotted contours indicate negative vorticity, and tic marks are at δ_ω^0 intervals. The spanwise domain has been extended using periodicity to $2L_z = 4\lambda_z$.

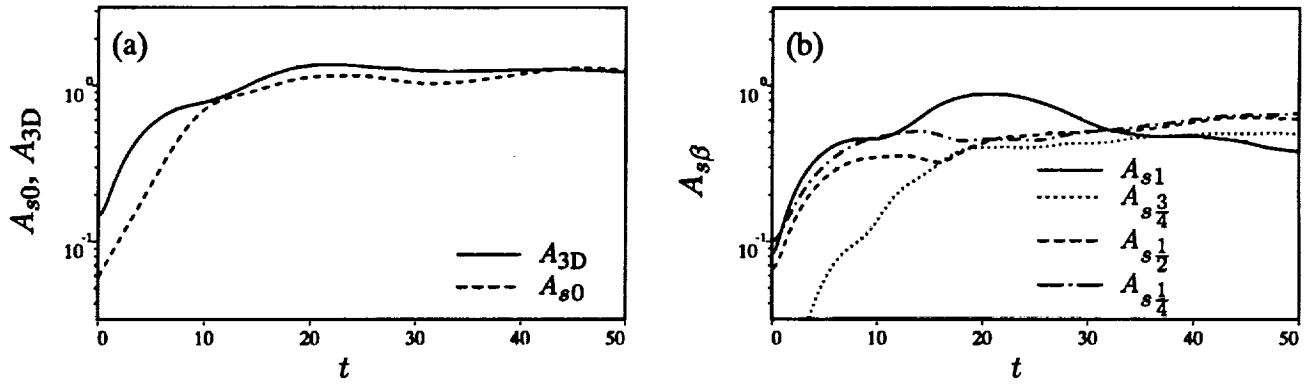

Figure 46. Time development of (a) A_{3D} and A_{s0} and (b) $A_{s\beta}$ ($A_{s\frac{3}{4}}$ not initialized) for TURB2P.

To allow the scale change to proceed further, a flow undergoing two pairings was simulated (TURB2P, see table 2). A second spanwise subharmonic was also included to allow a second scale change. The subharmonic phases ($\phi_{0\frac{1}{2}} = \frac{\pi}{8}$ and $\phi_{0\frac{1}{4}} = \frac{7\pi}{16}$) were chosen to get a very irregular initial rib-strength distribution with no symmetries. In this flow A_{3D} is larger than A_{s0} for most of the flow evolution (fig. 46(a)). A plot of $A_{s\beta}$ for various spanwise lengths is shown in figure 46(b). As can be seen from this figure, a scale change occurs at about the same time as in the previous cases ($\tau_{sc} = 32$), but both the $\beta = \frac{1}{2}$ and $\beta = \frac{1}{4}$ modes exceed the fundamental at the same time. Contours of the streamwise vorticity and the passive scalar in the surviving mid-braid plane at this time are shown in figure 47. The rib vortices have moved by mutual induction as discussed above, and it appears that both scale-change mechanisms I and II are occurring at the same time. Shortly after this time, this flow becomes turbulent and it is no longer possible to identify rib vortices in the MP. This turbulent flow is discussed in detail in section 8.

As noted above, the flow evolution in the MP becomes more complicated when vorticity reenters this plane at τ_{s1} (or at τ_{o0} in the absence of pairing). Although it appears that the reentry of spanwise vorticity did not play an important role in the scale changes discussed above, the restructuring of the MP vorticity after τ_{s1} could provide an additional mechanism for changing the characteristic spanwise scale. However, many of the flows examined in the preceding sections become "turbulent" after τ_{s1}, so that clearly defined ribs are not present to visually determine the spanwise scale (although Λ_z is still well defined).

To study the impact that reentry of vorticity into the braid region could have on scale change, we consider WMID2P, a flow with weaker initial perturbations. Figure 48 shows MP contours of ω_x at six different times during the evolution of WMID2P. By $t = 20$ the rib vortices are collapsed. Just after $\tau_{s1} = 32$ (fig. 48(a)), additional streamwise vorticity is visible away from the centerline. This vorticity becomes stronger by $\tau_{p2} = 40.1$ (fig. 48(b)) and then (because it has the same sign as the rib vorticity at the same spanwise location) "recollapses" into the ribs, resulting in stronger rib vortices, which are again compact and near the centerline (fig. 48(c)). Note that, except for $z = 0$ and $z = L_z/2$, the BP's are not symmetry planes and streamwise vorticity can cross through them. After $\tau_{s2} = 54$ (fig. 48(d)) another reentry of vorticity into the MP occurs. This time, however, ω_x of both signs is generated above and below many of the ribs. The recollapse is thus more complicated, but the compressive component of the strain associated with the primary rollers again drives the vorticity towards the centerline (fig. 48(f)), where some of it is wound into the ribs. Since there was a marked subharmonic component to the reentering vorticity, it can change the relative strengths of the ribs. At $t = 61.3 \approx \tau_{sc}$ (fig. 48(e)) mechanism I, described above, is active, as evidenced by the two pairs of rib vortices that are compressed together and dropping below the centerline (one on the domain boundary). Indeed, 11 time units later (fig. 48(f)), there appear to be only two pairs of significant rib vortices, approximately equally spaced and slightly above the centerline. Viscous effects have weakened the remaining ribs, whose remnants are still visible in figure 48(f). Although the actual scale change in the WMID2P flow occurred by mechanism I, the "recollapse" may be responsible for speeding up the process by enhancing the nonuniformity of the ribs.

It is perhaps surprising that scale change (as defined here) occurs even in the absence of pairing (see section 7.1). This scale change is not predicted by linear analysis (see fig. 14(a)). At early times (before $\tau_{o0} = 15.4$), the PH$\frac{\pi}{4}$0P flow evolves in the same way as the PH$\frac{\pi}{4}$1P flow, since the initial

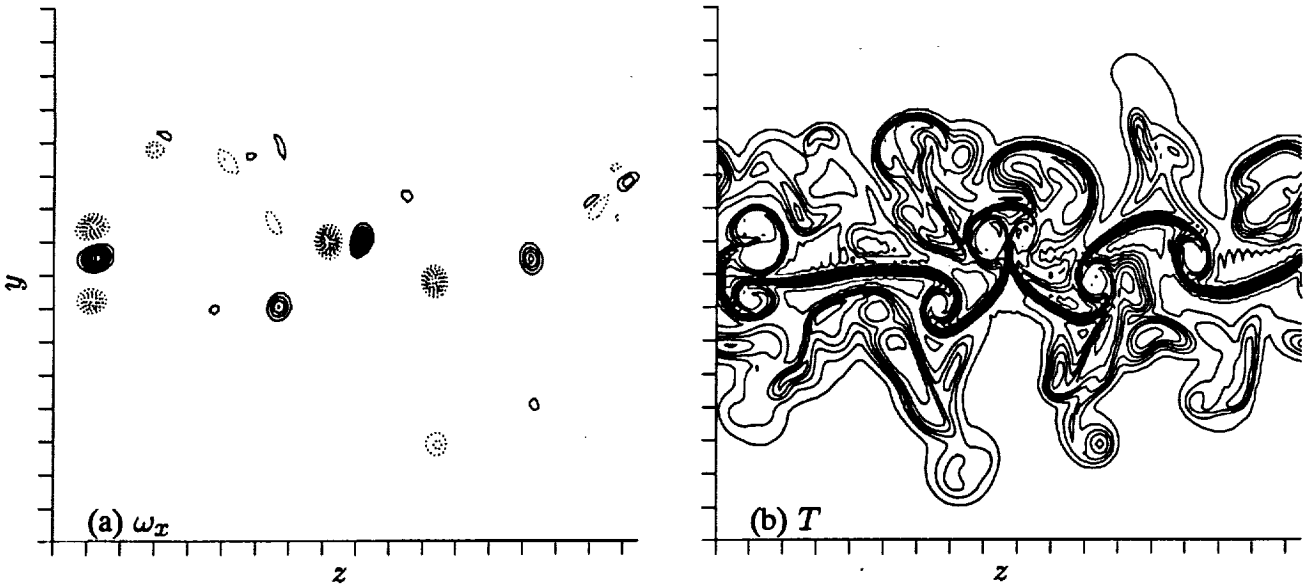

Figure 47. Contours of ω_x and the passive scalar (T) in the surviving MP of the TURB2P simulation at $t = 32.2$ ($\tau_{s1} = 29.2$). The contour increment is ± 1.0 in (a) and is 0.08 (from 0.02 to 0.098) in (b). Solid contours indicate positive vorticity, dotted contours indicate negative vorticity, and tic marks are at δ_ω^0 intervals.

three-dimensional perturbations are identical (see fig. 43(a)). By $t = 30$ (well beyond τ_{o0}) the flow has been "oversaturated" for a long time and much vorticity has reentered the braid region, greatly increasing the complexity of the flow (see fig. 49). Because of this, the flow appears "turbulent." Although there are no well-defined ribs in the MP, it is clear that a single large-scale structure ($\beta = \frac{1}{2}$) dominates the MP. This scale change is a result of the reentry of turbulent vorticity into the braid region. It is apparently unrelated to the two scale-change mechanisms discussed above.[17]

7.3 Comparison With Narrow-Spanwise-Domain Results

The flows discussed in sections 5 and 6 were precluded from undergoing a scale change because the largest possible spanwise wavelength corresponded to $\beta = 1$. The extent to which these simulations are affected by this constraint is therefore of great interest. Our main concern is how robust the results of sections 5 and 6 are, that is, whether low-amplitude spanwise subharmonic modes produce any large changes in the flow evolution. To test this, two simulations (WMID2P and WHIGH2P, see table 2) with weak spanwise subharmonics were examined.

It should be noted that, without the spanwise subharmonics, the WMID2P and WHIGH2P flows would be identical to the MID2P and HIGH2P flows (discussed in section 6), respectively. Comparisons of WMID2P with MID2P and of WHIGH2P with HIGH2P thus allow one to determine the extent to which the constraints on spanwise scales in MID2P and HIGH2P are modifying the flow.

[17] Although $A_{s\frac{1}{2}} > A_{s1}$ after $\tau_{sc} = 28.9$, $A_{0\frac{1}{2}}$ remains significantly smaller than A_{01}. It is thus quite possible that streamwise-averaged measures of scale change, such as that used by Huang and Ho (1990), would not indicate any scale change in this flow.

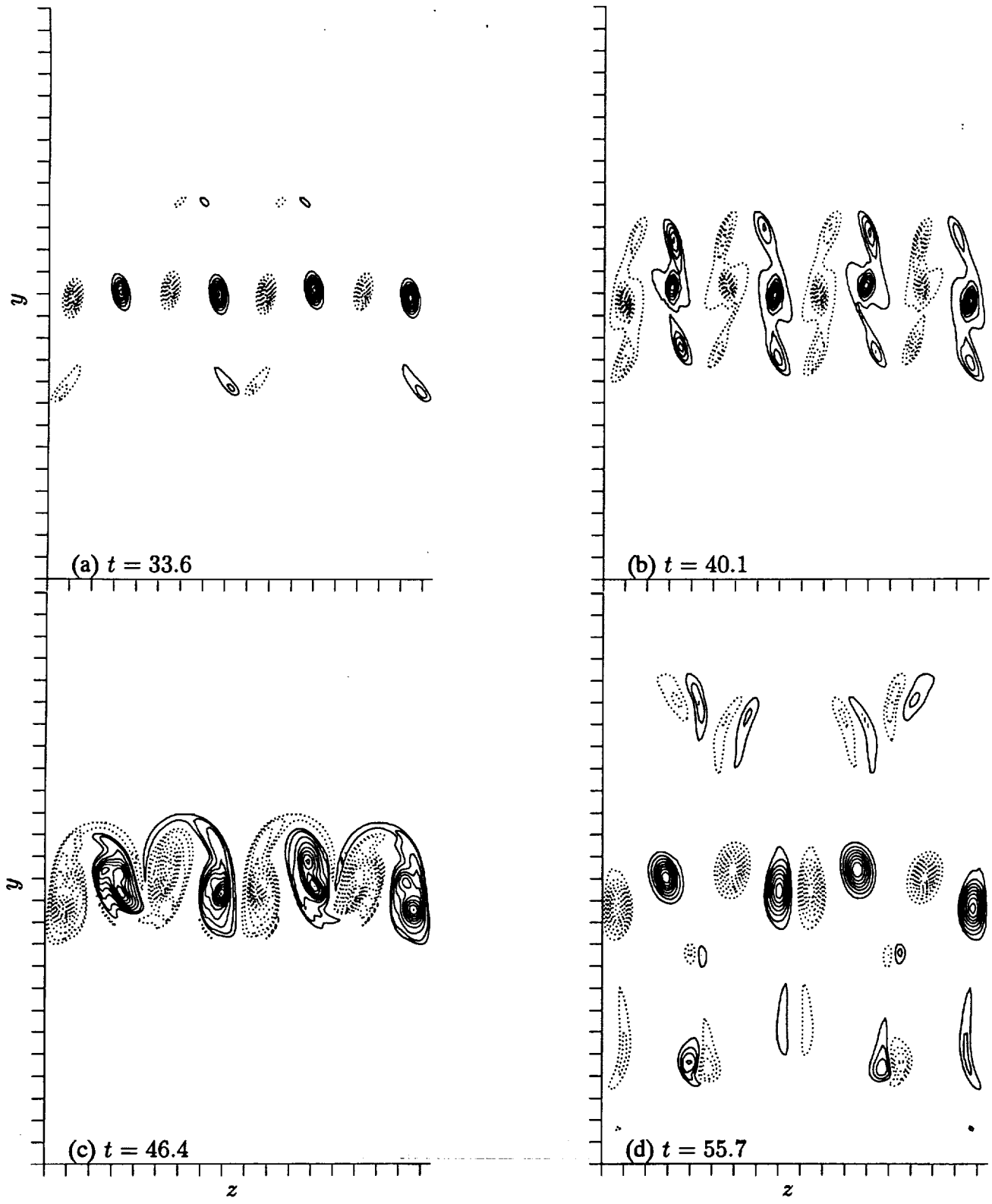

Figure 48. For caption see next page.

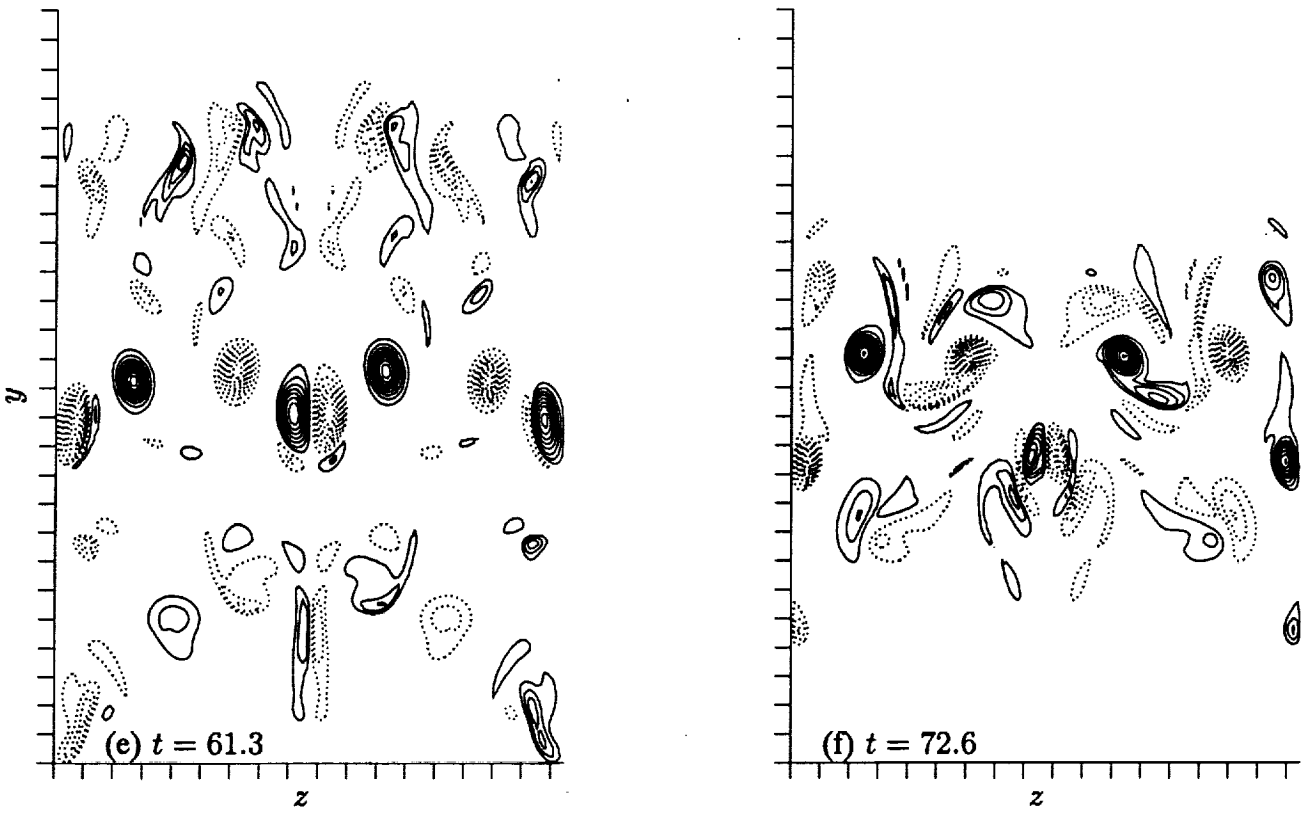

Figure 48. Contours of ω_x in the MP of WMID2P. The contour increments are (a,b,c) ± 0.2, (d) ± 0.3, (e) ± 0.35, and (f) ± 0.4. In (c) there is an extra contour at ± 0.1 to show the vorticity crossing the BP's. Solid contours indicate positive vorticity, dotted contours indicate negative vorticity, and tic marks are at δ_ω^0 intervals.

The evolutions of the initialized two-dimensional and STI modes in the WHIGH2P and HIGH2P simulations are compared in figure 50. Differences in A_{10} are noticeable after $t \approx 25$, well after τ_r. Similarly, differences in $A_{\frac{1}{2}0}$ occur after $t \approx 40$, well after τ_{p1}. The amplitude $A_{\frac{1}{4}0}$ in both simulations is very similar throughout the time considered. The amplitude A_{s0} also agrees well throughout the flow development (fig. 51(a)) because, by the time the individual $A_{\alpha 0}$ amplitudes differ, they make only a small contribution to A_{s0}. Perhaps more surprising is that A_{3D} also differs by 6% at most and is virtually identical up to $t = 35$. In WHIGH2P a scale change occurs at $\tau_{sc} = 48.1$ (fig. 50(b)) that cannot occur in HIGH2P. The differences between the evolutions of the WMID2P and MID2P flows are even less than the differences between WHIGH2P and HIGH2P.

Comparisons of other flow statistics (such as mid-braid strain rate, mid-braid vorticity level, rib circulation, layer thickness, and vorticity extrema) and flow-field contour plots also indicate similar flow evolution between both pairs of simulations, particularly for $t < 40$. These results confirm that a spanwise scale change triggered by weak spanwise subharmonics is slow. Thus, strong spanwise subharmonics are needed for flow evolution to vary significantly from that discussed in section 6.

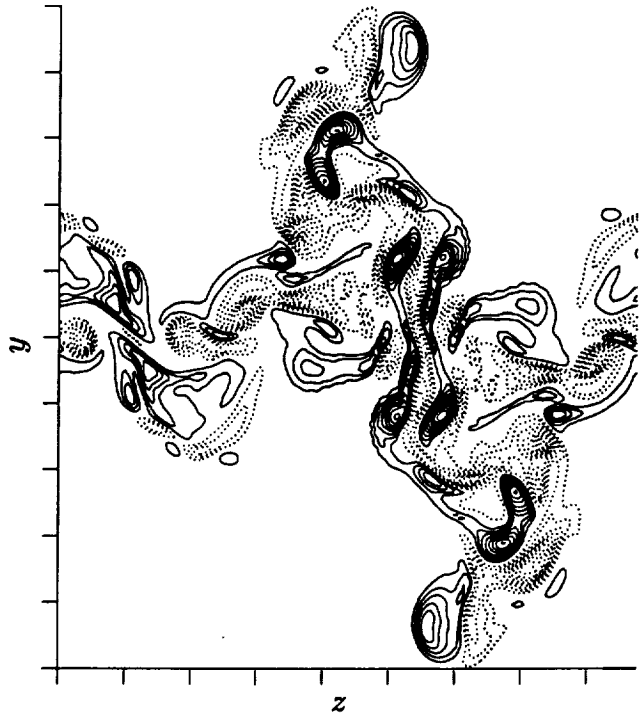

Figure 49. Contours of ω_x in the MP of PH$\frac{\pi}{4}$0P at $t = 30.0$. The contour increment is ± 0.6. Solid contours indicate positive vorticity, dotted contours indicate negative vorticity, and tic marks are at δ_ω^0 intervals.

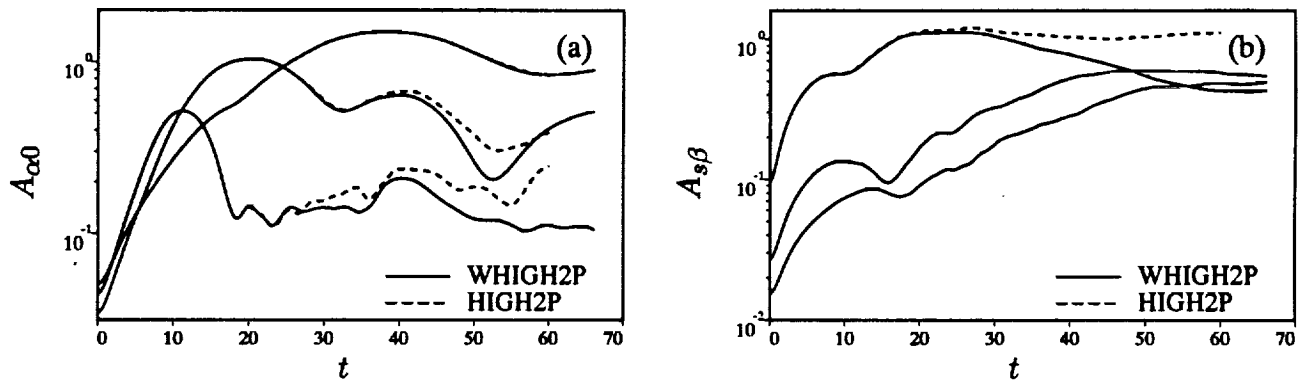

Figure 50. Time development of (a) $A_{\alpha 0}$ and (b) $A_{s\beta}$ for WHIGH2P and HIGH2P. In (a) the curves that peak at $t = \tau_r = 11.2$ are A_{10}, those that peak at $t = \tau_{p1} = 20.4$ are $A_{\frac{1}{2}0}$, and those that peak at $t = \tau_{p2} = 38.5$ are $A_{\frac{1}{4}0}$. In (b) $A_{s1} > A_{s\frac{1}{2}} > A_{s\frac{1}{4}}$ at $t = 0$. (Note $A_{s\frac{1}{2}} = A_{s\frac{1}{4}} = 0$ for HIGH2P.)

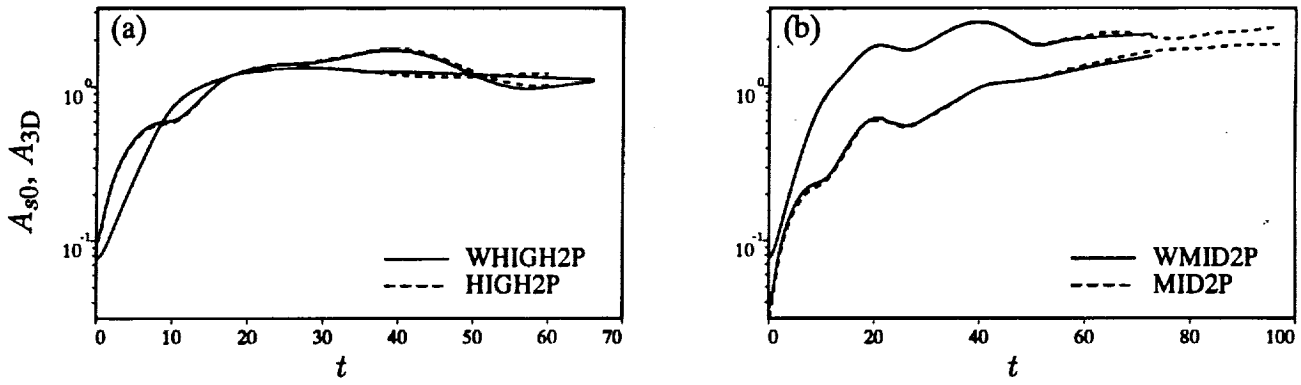

Figure 51. Time development of A_{s0} and A_{3D} for (a) WHIGH2P and HIGH2P and (b) WMID2P and MID2P. At $t = 40$ the upper curves are A_{s0} and the lower curves are A_{3D}.

8 CHARACTER OF THE POST-TRANSITION FLOW

Several of the flows discussed in the preceding sections undergo a transition to turbulence. However, most of these were constrained in some artificial way. For example, HIGH2P was constrained by the exclusion of spanwise subharmonics and the imposition of symmetries in the initial condition. While these constraints help to analyze the transition process, they produce an unnatural turbulence. One case (TURB2P) was designed to eliminate all symmetries and most constraints. The disorder in the resulting flow is similar to that in experimental mixing layers. For example, the MP passive scalar contours shown in figure 47 are similar to the flow-visualization pictures of Bernal and Roshko (1986). In this section, the character of this turbulence will be extensively documented to provide a basis for comparisons with experimental measurements and with future simulations begun from turbulent initial conditions. The flow at $t = 39.8$ is chosen for this purpose because it contains "healthy turbulence" and yet is before $\tau_{p2} = 47.1$ and therefore far from being oversaturated. It is thus not affected by the absence of a further pairing.

At $t = 32.2$ (fig. 47) TURB2P is undergoing a transition similar to that described in section 6.2 for the HIGH2P flow. However, there is a subtle difference. Because of the strong subharmonic STI disturbances and their relative phasings, the ribs do not remain at fixed locations in the braid region. Consequently, well-defined "rib planes" and "between-ribs planes" do not exist. The distinction between higher-order roll-ups of thin vortex sheets in the BP's and the granular patterns in the RP's is thus largely absent. The flow appears to contain a combination of both these features at all spanwise locations (see fig. 52).

While x-y contour plots of ω_z in the HIGH2P (figs. 40 and 41) and TURB2P (fig. 52) flows are qualitatively similar (with the exception noted above regarding the RP and BP features), the x-z planes appear significantly more "turbulent" in TURB2P. Much of the increased complexity is due to the elimination of the symmetries given in equations (12) and (13). Vorticity contours in the centerline x-z plane of the TURB2P flow are shown in figure 53 at times before and after the transition. The loss of regularity is obvious.[18]

[18]Note that there is still some evidence of engulfed ribs at $x = L_x/2$ in figure 53(d).

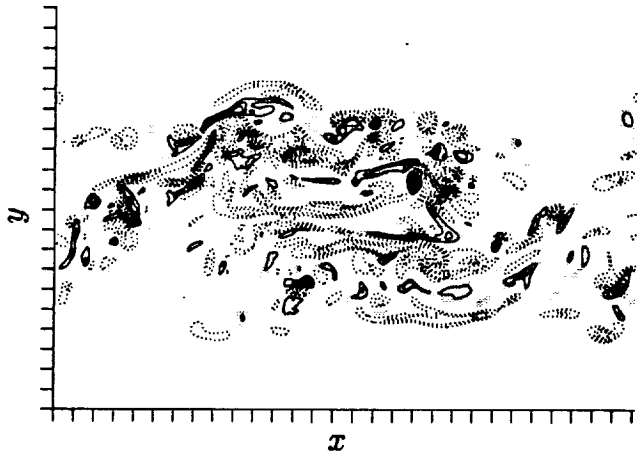

Figure 52. Contours of ω_z in the $z = 0$ x-y plane at $t = 39.8$ in TURB2P. The contour increment is ± 0.5. Regions of positive vorticity are shaded and negative contours are dotted. Tic marks are at δ_ω^0 intervals.

The y-dependence of several horizontally averaged statistics is shown in figure 54. Both the mean velocity and mean scalar profiles are roughly symmetric around the layer centerline. The mean velocity ($\overline{U}$) is almost an error function (an error function of the same thickness is plotted in fig. 54(a) for reference). The mean scalar ($\overline{T}$) profile is more nearly piecewise-linear. This suggests that a constant-eddy-viscosity model might be adequate for the transport of momentum, but not of the scalar. At this time ($t = 39.8$) both mean gradients are negligible beyond $|y| \approx 8$.

The rms velocity fluctuations (u', v', and w') and the Reynolds stress ($-\overline{uv}$) are shown in figure 54(b). At $t \approx 10$ (not shown), all rms velocities have a well-defined single peak at the centerline. By $t = 39.8$, however, they are approximately constant over the central portion of the mixing layer (about $-4 \leq y \leq 4$). The rms velocity fluctuations all decay slowly in y. This is due to the slowly decaying potential velocity fluctuations. Two-dimensional fluctuations dominate the potential velocity far from the vortical part of the layer, resulting in a lower level of w' compared to u' and v' for large y. The potential velocity fluctuations do not contribute to the Reynolds stress ($-\overline{uv}$); thus the Reynolds stress decays rapidly in y.[19] Like the rms velocities, the rms vorticities (denoted by ω_i' and shown in fig. 54(d)) are roughly constant over the region $-4 \leq y \leq 4$ (profiles are even flatter at later times) after exhibiting single peaks at the centerline early in the layer development.

At $t = 39.8$, the Reynolds stress correlation coefficient $-\overline{uv}/(u'v')$ is just over 0.6 in the central portion of the layer. Later in time ($t = 50$), $-\overline{uv}$ changes sign over at least part of the layer (the middle at this time). This is associated with the completion of the second pairing ($\tau_{p2} = 47.1$). The reversal in sign of the Reynolds stress $-\overline{uv}$ is associated with counter-gradient momentum flux and has been observed in other temporally developing (e.g., Riley and Metcalfe, 1980; Metcalfe et al., 1987) as well as forced, spatially developing (Oster and Wygnanski, 1982; Lowery and Reynolds, 1986; Lele, 1989) mixing layers. It is particularly prevalent in two-dimensional flows. Riley and Metcalfe and Metcalfe et al. attributed this change in sign to oversaturation. While it is true that the first pairing (unless

[19]The scalar fluctuations, the vorticity fluctuations, and the scalar fluxes also do not exhibit slowly decaying potential tails. All these quantities are essentially zero where the mean gradient is zero.

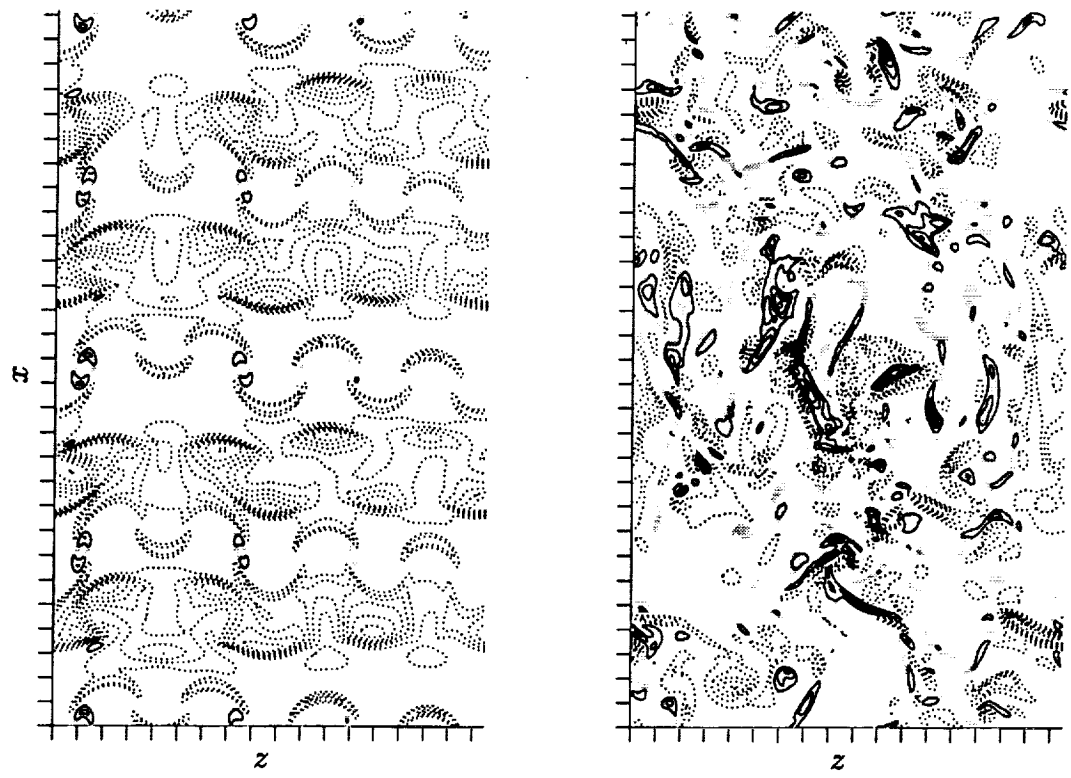

(a) ω_z at $t = 11.7$ (b) ω_z at $t = 39.8$

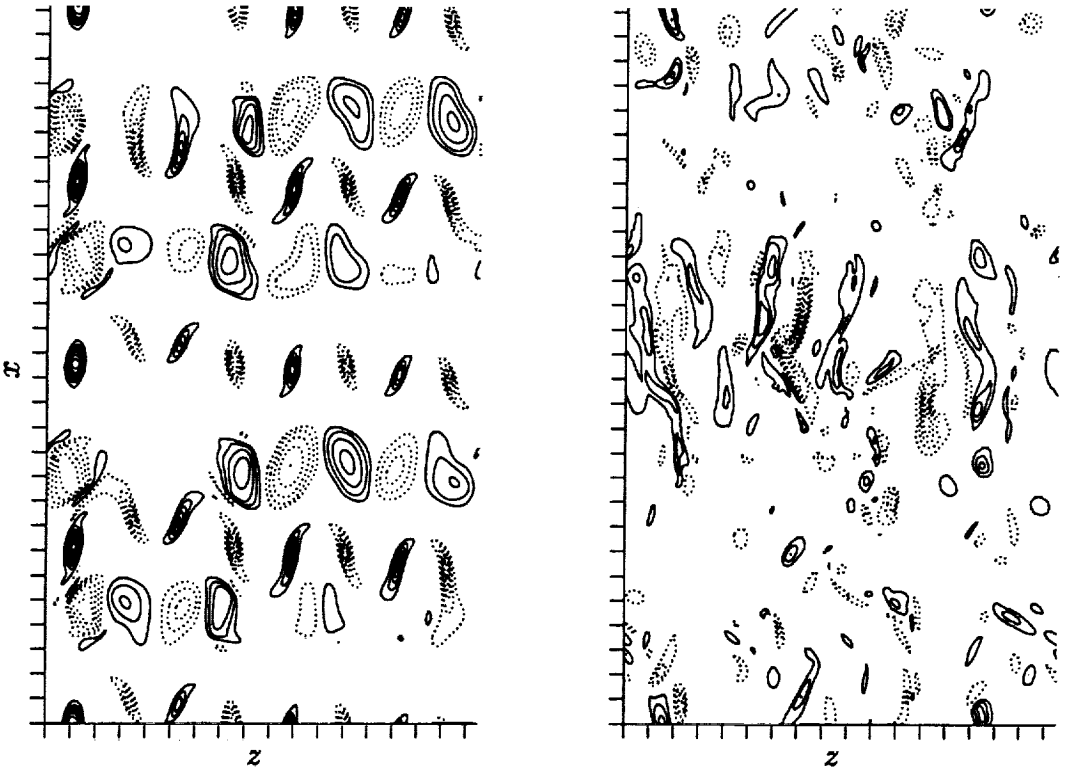

(c) ω_x at $t = 11.7$ (d) ω_x at $t = 39.8$

Figure 53. Contours of ω_z and ω_x in the centerline z-x plane of TURB2P. The contour increment is ± 0.5 except in (d), where it is ± 1.0. Shaded regions indicate regions of positive ω_z (opposite in sign to the mean vorticity), dotted contours indicate negative vorticity, and tic marks are at δ_ω^0 intervals.

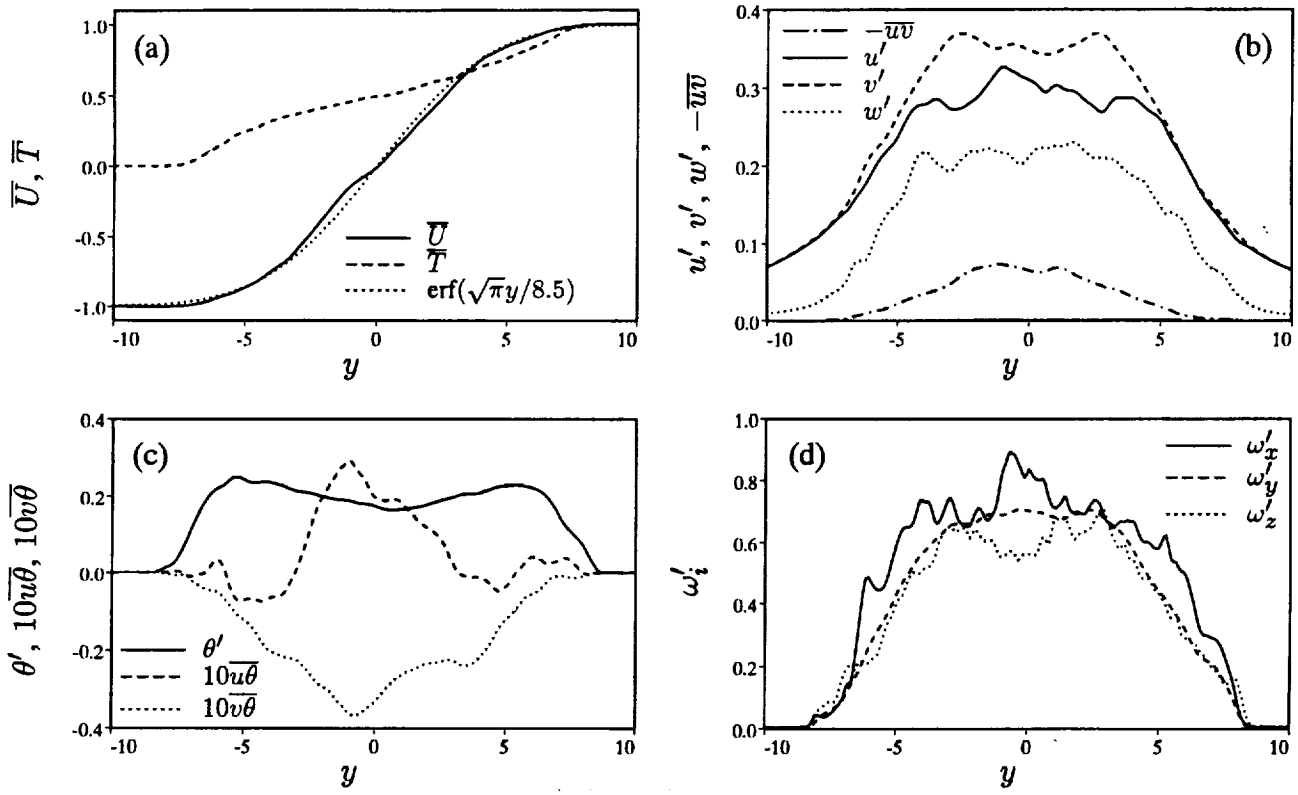

Figure 54. Profiles in y of various x-z averaged statistics for TURB2P at $t = 39.8$.

substantially delayed) will prevent this change in sign of the Reynolds stress, further pairings do not, in general, happen fast enough to eliminate a period of counter-gradient momentum flux after each pairing. Strong three-dimensionality can change this, however, and both the TURB2P and WHIGH2P flows do not exhibit such a change in sign (or the accompanying reduction in momentum thickness) after the first pairing (as does the WMID2P flow). It is unclear whether the change in sign observed in all three of these flows after the second pairing could be prevented by a third pairing.

The rms scalar fluctuation profile (note that θ is used here for $T - \overline{T}$ and that θ' is its rms value) is double-peaked (fig. 54(c)), a feature that becomes more pronounced after the first pairing. Because of the mean shear, the scalar flux vector has both streamwise and vertical components ($\overline{u\theta}$ and $\overline{v\theta}$), even though there is no streamwise mean scalar gradient. The correlation coefficients $\overline{u\theta}/(u'\theta')$ and $\overline{v\theta}/(v'\theta')$ at $t = 38.9$ are roughly 0.4 and -0.5, respectively.

The profiles of $\bar{\epsilon}$, the x-z averaged dissipation rate of turbulent kinetic energy, at $t = 39.8$ in TURB2P and at $t = 40.1$ in WMID2P are shown in figure 55(a). The time evolution of the y-integral of these profiles (ϵ_t) is shown in figure 55(b) for the same two flows. The presence of many small-scale structures in the TURB2P flow (e.g., figs. 53(b) and 53(d)) results in a significantly higher rate of kinetic energy dissipation. As a result, the integrated turbulent kinetic energy is smaller in TURB2P than in WMID2P after τ_{p1}.[20]

[20] In WMID2P the "production" of turbulent kinetic energy actually becomes negative for a period after each pairing. Thus, while the kinetic energy is roughly constant in TURB2P after $t = \tau_{p1}$, it increases and oscillates in WMID2P, remaining above the TURB2P level for $t > \tau_{p1}$.

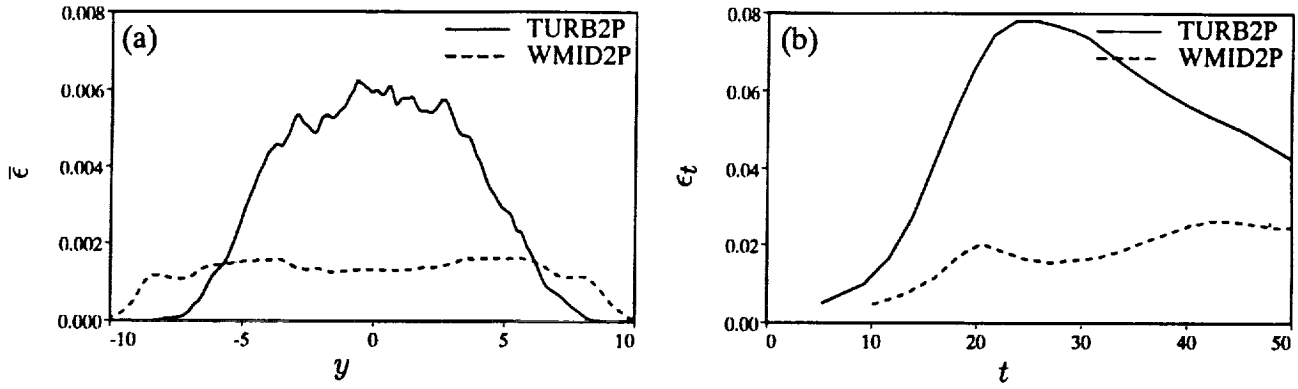

Figure 55. Dissipation rate of turbulent kinetic energy for TURB2P and WMID2P. (a) Profiles in y of x-z averaged dissipation rate at $t = 39.8$ for TURB2P and at $t = 40.1$ for WMID2P. (b) Time evolution of y-integrated dissipation rate.

The quantities shown above can be used to form a turbulent time scale $\overline{q^2}/\overline{\epsilon} = (\overline{u'^2} + \overline{v'^2} + \overline{w'^2})/\overline{\epsilon}$. This time scale is roughly constant in the core of the layer and is about 45 at $t = 39.8$. The turbulence Reynolds number, $Re_T = \overline{q^2}^2/(\overline{\epsilon}\nu)$, is about 3000 in the middle of the layer at this time.

One-dimensional spectra of q^2 and ϵ at $y = 0$ in TURB2P at $t = 39.8$ are shown in figure 56. These spectra indicate that the flow is well resolved, since there is at least a two-decade falloff in the dissipation spectra. Also, the fact that this is a low-Reynolds-number turbulent flow is evident since there is no discernible inertial range. Finally, it is clear that the size of the streamwise domain constrains the flow evolution, since the streamwise q^2 spectrum does not plateau at low wavenumbers. This is expected, since at $t = 39.8$ the second and final pairing in this flow has begun.

In addition to an increased rate of kinetic energy dissipation, the small-scale turbulence provides more thorough "mixing." A zero-heat-release, fast chemical reaction can be studied using the passive scalar carried in the simulations (Burke and Schumann, 1928; Zeldovich, 1950; Toor, 1962). The ratio of the amount of reaction product to the reaction product that would be present if there were no scalar fluctuations is a measure of the degree of scalar mixing (Konrad, 1976). This ratio is denoted by $\mathcal{M}$ here and is given by

$$\mathcal{M} = \frac{\int_{-\infty}^{\infty} \overline{\mathcal{P}(T(t))} - \mathcal{P}(\overline{T}(t=0))\, dy}{\int_{-\infty}^{\infty} \mathcal{P}(\overline{T}(t)) - \mathcal{P}(\overline{T}(t=0))\, dy} \tag{19}$$

where $\mathcal{P}(T) = 1 - |2T - 1|$ is the product concentration, an overline indicates the average over x and z, and the second term in each integrand eliminates the contribution of the initial scalar profile. In figure 57 the evolution of this ratio for TURB2P and WMID2P is shown (the evolution for WHIGH2P is shown in Moser and Rogers, 1991). Note that the ratio is initially 1.0 since there are no scalar fluctuations at $t = 0$. The late-time plateau level of the transitional TURB2P flow is 0.18 greater than that of the nontransitional WMID2P flow. This difference is close to the value of 0.15 measured by Konrad (1976) in his experiments at a similar Schmidt number (0.7 compared to our 1.0).

The probability density function (pdf) of ω_z is qualitatively different in the transitional and the nontransitional flows. As can be seen in figure 58, WMID2P, WHIGH2P, and TURB2P all exhibit

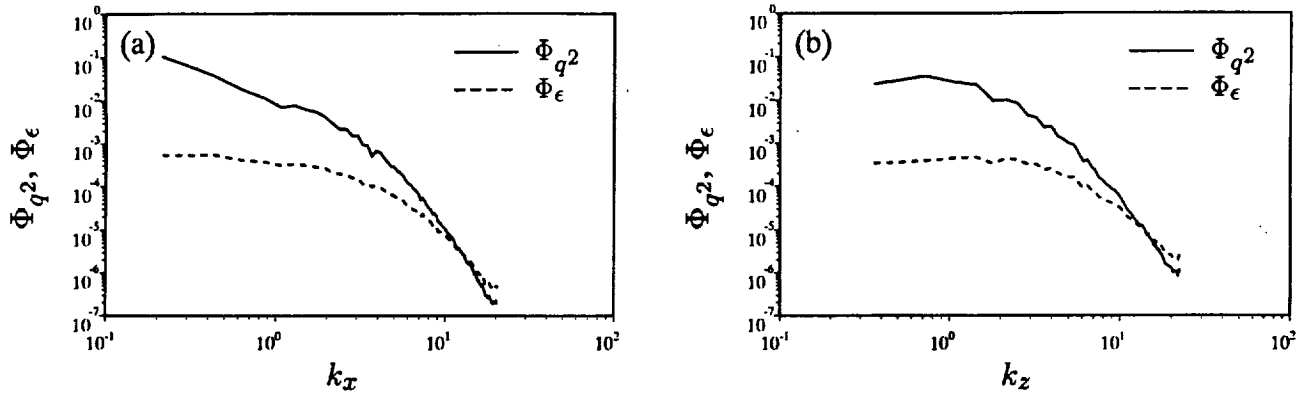

Figure 56. One-dimensional spectra of q^2 and ϵ in the (a) streamwise and (b) spanwise directions at $t = 39.8$.

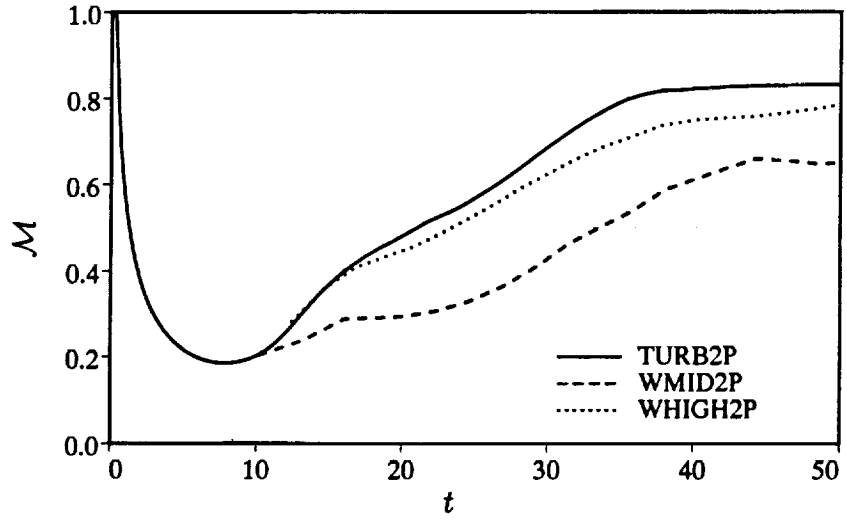

Figure 57. Time development of the "mixedness" parameter $\mathcal{M}$.

roughly exponential decay of $P(\omega_z)$ as $|\omega_z|$ becomes large. There are, however, two distinct differences between the transitional and nontransitional flows. In the nontransitional case (WMID2P), there is little positive ω_z (opposite in sign to the mean vorticity) and there are significant amounts of irrotational fluid (or at least fluid with $\omega_z \approx 0$) near the centerline of the layer. In contrast, the pdf of ω_z in the TURB2P flow is more symmetric and has a much smaller peak at $\omega_z = 0$. The pdf for the WHIGH2P flow is intermediate in both these respects. These results suggest a possible transition criterion based on the level of positive ω_z present in the flow. Such a criterion was proposed by Moser and Rogers (1991).

9 "HELICAL" PAIRING

Flow visualizations by Chandrsuda, Mehta, Weir, and Bradshaw (1978) indicated that there were strong spanwise variations in the Kelvin-Helmholtz rollers. This seemed to be the result of pairing occurring at some spanwise locations sooner than at others, resulting in rollers that appeared to be "twisted." This has led some investigators to speculate that the pairing is "helical." Pierrehumbert and Widnall (1982) have suggested that a pair of disturbances in the $(\frac{1}{2}, \pm\frac{1}{2})$ modes (oblique subharmonics)

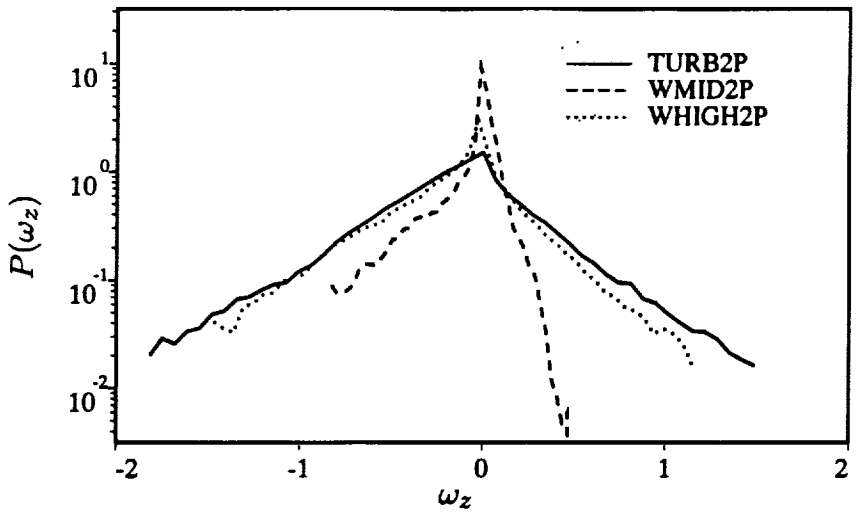

Figure 58. Probability density function of ω_z at the centerline of the layer for TURB2P at $t = 39.8$, WMID2P at $t = 40.1$, and WHIGH2P at $t = 39.9$.

could lead to such localized pairing. When properly phased relative to the two-dimensional $(1,0)$ disturbance, such an oblique subharmonic disturbance kinks two neighboring rollers such that any single roller will be closer to its downstream neighbor over part of its spanwise extent and closer to its upstream neighbor over the rest. Pierrehumbert and Widnall felt that nearby portions of the Kelvin-Helmholtz rollers would pair, resulting in a highly three-dimensional, twisted pattern similar to that observed by Chandrsuda et al.

In this section, several flows initialized with such oblique subharmonic modes are described. The parameters are given in table 3. The streamwise vorticity of the three-dimensional disturbance is given by

$$\omega_x = - \sum_{\beta=1,\frac{1}{2}} A^0_{\frac{1}{2}\beta} \mathcal{R}\left(g_\beta(y) e^{i(k_x x - \phi_{\frac{1}{2}\beta})} \right) \sin(k_z z) \tag{20}$$

where $g_\beta(y) = c_\beta(4y^2 - 2 - (k_x^2 + k_z^2))e^{-y^2}/(k_x^2 + k_z^2)^{\frac{1}{2}}$ (v-Gaussian profile or vG), and the normalization constant c_β is selected such that the integrated energy in the $(\frac{1}{2}, \beta)$ mode is unity when $A_{\frac{1}{2}\beta}$ is one. The ω_z component of the disturbance is set to make the vorticity solenoidal. The initial three-dimensional disturbance contained no ω_y, although ω_y develops rapidly to amplitudes comparable to ω_x. As with the oblique-mode cases in section 4.4 of Part 1, the relative phasing between the oblique modes and two-dimensional disturbances is important. Two extreme phasings were used. The first ($\phi_{\frac{1}{2}\frac{1}{2}} = -\pi/2$) results in kinked rollers, as suggested by Pierrehumbert and Widnall (1982). The other phasing ($\phi_{\frac{1}{2}\frac{1}{2}} = 0$) results in bulging rollers (i.e., alternating regions of thicker and thinner rollers) where the bulges of neighboring rollers are out of phase.

Table 3. Parameters of the "helical" pairing simulations. Disturbance profiles are vG, $\phi_{\alpha 0} = 0$, $Re_0 = 250$, $Pr = 0.7$, $\lambda_x = 1.16(2\pi)$, and $\lambda_z = 0.6\lambda_x$ for all cases.

Simulation	A_{10} $\times 10^2$	$A_{\frac{1}{2}0}$ $\times 10^2$	$A_{\frac{1}{2}\frac{1}{2}\frac{1}{2}}$ $\times 10^2$	$A_{\frac{1}{2}1}$ $\times 10^2$	$\phi_{\frac{1}{2}\frac{1}{2}\frac{1}{2}}$	$\phi_{\frac{1}{2}1}$	τ_r	τ_{p1}
KINK0P	12.12		8.72		$-\frac{\pi}{2}$		10.5	
KINK1P	12.12	2.00	8.72		$-\frac{\pi}{2}$		10.3	25.1
BULG0P	12.12		8.72		0		10.6	
BULG1P	12.12	2.00	8.72		0		10.2	24.2
NBULG0P	12.12		1.74	6.73	0	0	10.3	
NBULG1P	12.12	4.00	1.74	6.73	0	0	9.6	20.9

9.1 "Kinked" Roller Phasing

The kinked-phasing flow KINK0P did not undergo "helical" pairing and remained largely two-dimensional throughout its evolution. Portions of the rollers that were close to each other were initially displaced vertically, similar to rollers that do pair, but did not continue to rotate around each other and coalesce into a paired roller. The developed flow thus consisted of two kinked Kelvin-Helmholtz rollers, with the direction of the kink varying in time. Much of the flow evolution was similar to the OBLOUT simulation described in Part 1. In particular, the MP ω_x and ω_y distributions are antisymmetric in y, implying that $\Gamma_x = 0$ throughout the flow evolution. As in OBLOUT, rib "dipoles" form in the RP and move toward another rib "dipole" of opposite sign, forming a quadrupole centered in a BP, which decays due to viscosity (in the larger computational domain used here, one quadrupole forms in the center of the domain, the other on the boundary, as in OBLOUT). Because no sustained rib vortices form in this flow, streamwise (and normal) vorticity is located predominantly in the roller core where the roller is kinked. The associated three-dimensionality is thus weak, and $A_{3D} < A_{s0}$ throughout the flow evolution.

Note that, with only $(1,0)$ and $(\frac{1}{2}, \pm\frac{1}{2})$ disturbances, no nonlinear interaction can transfer energy to the $(\frac{1}{2}, 0)$ mode. Because of this, the two rollers in the domain can never pair with each other along their entire span. In experiments, some energy will certainly be present in two-dimensional subharmonic modes, and therefore the above simulation was repeated with an initially small amount of energy in the first two-dimensional subharmonic (KINK1P). This flow was virtually identical to KINK0P until τ_{p1}, when the two kinked rollers paired along the entire span (with ω_z distributions similar to those of the two-dimensional pairing discussed in section 3). It is thus apparent that, to induce pairing irregularities along the span of the flow, either a different type of initial condition or a wider spanwise length scale is needed.

Up to about τ_{s1} in KINK1P, the paired roller described above remains similar to its two-dimensional counterpart. Beyond τ_{s1}, however, there is evidence of stronger three-dimensionality. In particular, the central portion of the roller core becomes largely irrotational at some spanwise locations (alternate BP's), producing hoop-shaped structures similar to those observed in the OBLOUT simulation described in

Part 1.[21] Presumably at still later times this could lead to stronger three-dimensionality, as it does in OBLOUT.

9.2 "Bulging" Roller Phasing

For the bulging case, BULG0P, sustained ribs (whose sign is the same as that given by the initial condition) form in the braid region and collapse for the disturbance amplitudes considered here ($\Gamma_x^0 = 0.354$). As in the OBLIN simulation of Part 1, the rib vortices are oblique when they collapse and become S-shaped at late time. Because the disturbance is subharmonic in x, these ribs alternate in sign in the streamwise direction. The ω_x distribution in the roller core is opposite in sign to the adjacent rib and thus contains both positive and negative regions (it is antisymmetric in y in the CP), not unlike the pattern shown in figure 40(c) of Part 1 for the OBLOUT simulation.

The evolution of spanwise vorticity in the BP of BULG0P is illustrated in figure 59. Because the rib streamwise vorticity alternates in sign in the streamwise direction, the spanwise vorticity in the right roller is stretched (and amplified), whereas that in the left roller is weakened by "compression." Thus, even though the left roller has the stronger ω_z initially, the right roller exhibits significantly stronger ω_z by $t = 5.3$ (fig. 59(a)). By $t = 8.7$ (fig. 59(b)) the roll-up is nearly complete ($\tau_T = 10.6$). The left roller is "large" and the right roller is "small" (note the opposite is true in the other BP). At this point the nature of the vortex stretching is changing. In particular, the double-lobed pattern of core ω_x, described in the previous paragraph, has developed. Because of this, stretching (and amplification of ω_z) is occurring in the central core of the left roller and in the region where the ribs meet the core in the right roller. As with OBLOUT, the stretching is occurring on both sides of the right roller at the same spanwise location (as expected from the ω_x distribution). This results in the formation of a "hoop" structure. The beginnings of this hoop are just visible in figure 59(b). (The ω_z in the central core contour is weaker than that in the surrounding annulus.) By $t = 14.5$, there is a well-defined hoop surrounding virtually irrotational fluid (fig. 59(c)). At this time the left roller is oversaturated, resupplying spanwise vorticity to the adjacent braid regions. However, this oversaturated roller is quite different from those described in Part 1. It appears more like a postpairing roller, with spiral arms separate from the core vorticity. The "wisps" of ω_z that form these spiral arms contain the vortex lines that connect neighboring ribs, as they do in the typical roll-up evolution described in Part 1. By $t = 19.6$ (fig. 59(d)), the left roller has shed much of its spanwise vorticity to its neighbors, and the hoop of the right roller has collapsed. By $t = 22.1$ (fig. 59(e)), the left roller also collapses, and it is the right roller that appears "large." At $t = 24.3$ (fig. 59(f)), the right roller begins to reform a hoop and a second oversaturation is occurring, this time with vorticity from the right roller reentering the braid region. The left roller has completely collapsed and now consists of two higher-order roll-ups of the type described in Part 1 (for the OBLOUT case) and in section 5.2 of this paper. The ω_z levels associated with these higher-order roll-ups are very high (up to -19.8), and in figure 59(f) it was necessary to contour them with levels different from those used for the right roller (which would not even show up at the lowest contour level used for the higher-order roll-ups). At this point the flow appears to be beginning a transition to a more "turbulent" state, with many small-scale structures appearing in the vorticity field (see also fig. 61(d)).

[21] It is interesting to note that hoop structures form in OBLOUT from $(1, 0)$ and $(1, \pm 1)$ disturbances and in this simulation from $(\frac{1}{2}, 0)$ and $(\frac{1}{2}, \pm\frac{1}{2})$ disturbances after a pairing.

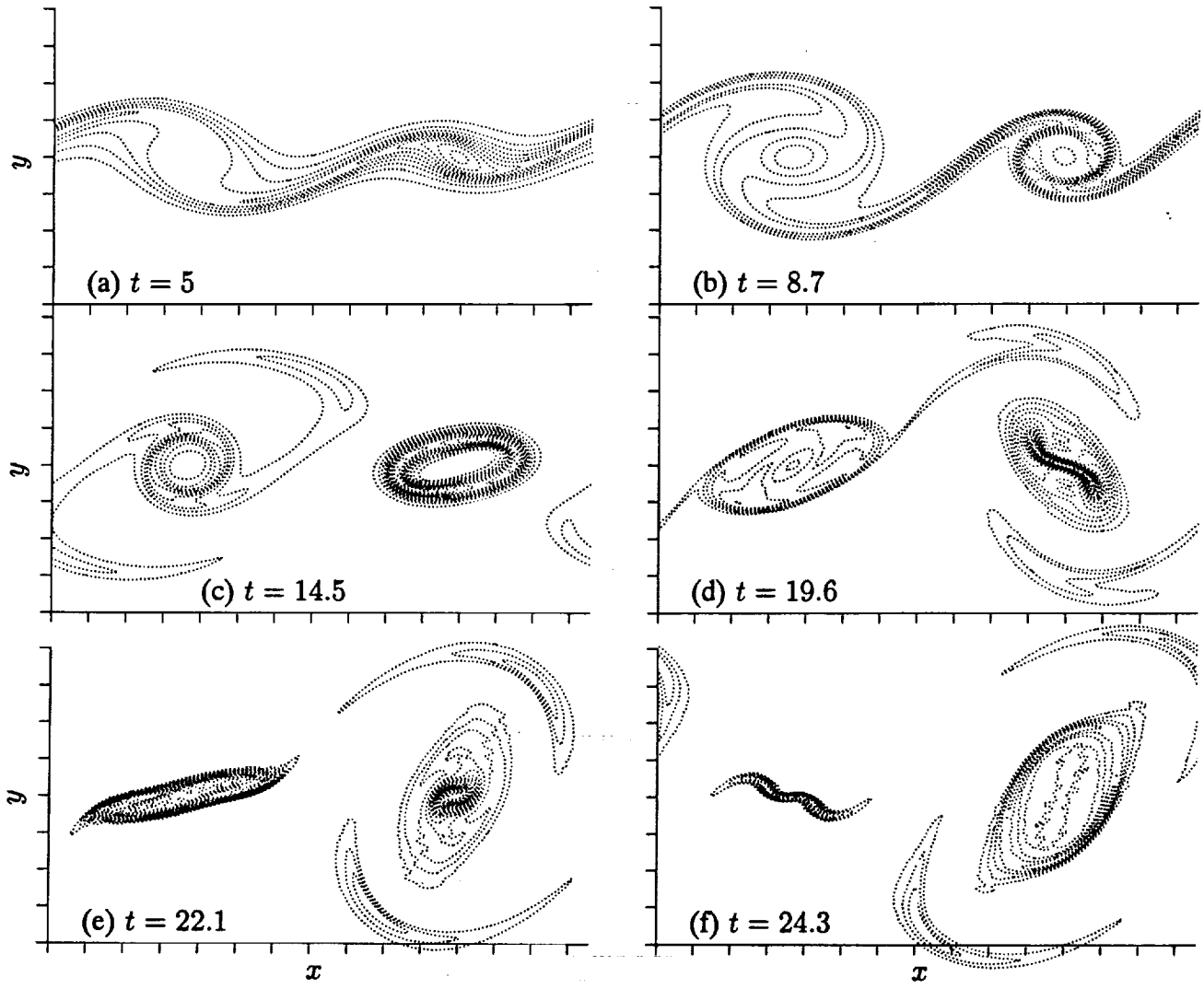

Figure 59. Contours of ω_z in the $z = 0$ BP of BULG0P. The contour increment is -0.3 except for the left roller in (f) where the contour increment is -2.0 (all ω_z in the right "roller" is thus weaker than the first contour level used for the left "roller"). Tic marks are at δ_ω^0 intervals.

The evolution of the rib circulation in the MP of BULG0P is shown in figure 60 (note that the rib circulations in both braid regions of the domain are equal in magnitude and opposite in sign for this case). Its behavior is qualitatively different from that of the other simulations described in this paper in that Γ_x changes sign at $t = 14.7$ and again at $t = 24.7$. As in the other simulations, Γ_x initially grows, reaching a value of 2.3 (6.5 times Γ_x^0) at $t = 11.7$. At this time (τ_{o0}), the first oversaturation described above occurs. Unlike the standard cases, the vorticity that reenters the braid regions is associated with rib vortices that are opposite in sign to the ribs already present in each braid region (again because the initial disturbance is subharmonic in x). Because of this, the circulation is reduced rather than augmented. By $t = 21.7$, Γ_x reaches a minimum of -3.3. At this point a second oversaturation occurs. As can be seen by tracking the origin of the "reentering vorticity" in figure 59(f), this second reentry of vorticity into the braid region contains wisp vorticity that connects rib vortices from *two* braid regions away. The associated ω_x is thus of the same sign as that present initially, and Γ_x begins to increase again.

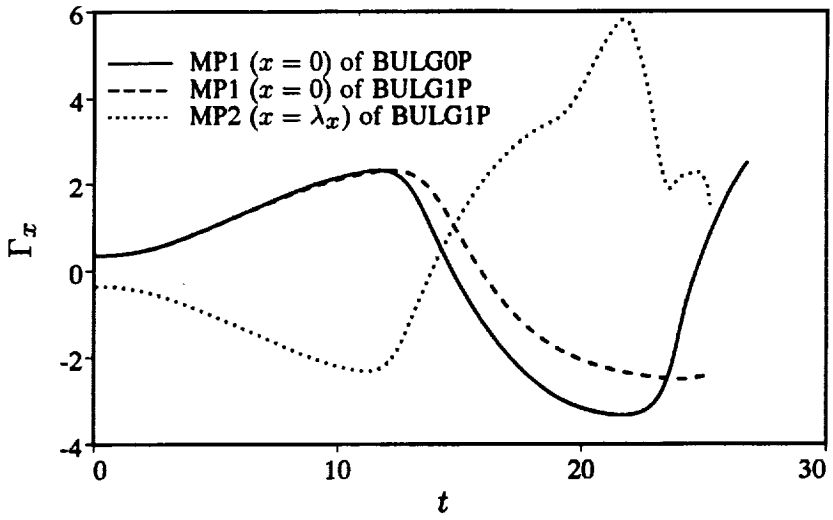

Figure 60. Time development of the mid-braid streamwise circulation Γ_x in BULG0P ($\Gamma_x(x = \lambda_x) = -\Gamma_x(x = 0)$) and BULG1P.

The reentry of opposite-signed ω_x into the MP can be seen directly in figure 61. At $t = 11.7$, Γ_x reaches a maximum and the rib vorticity is largely collapsed (fig. 61(b)). After τ_{o0}, ω_x that is opposite in sign to that of each rib vortex reenters the MP. By $t = 19.6$ (fig. 61(c)) four regions of such opposite-signed ω_x are present in each half of the spanwise domain. At $t = 24.3$ (after the second reentry) four more regions of ω_x, with the same sign as the original rib vortex, are present in the MP (fig. 61(d)). Note that, despite the changing sign of Γ_x, the original collapsed rib vortex retains its identity, with little change in circulation. It also appears that, by $t = 24.3$, a *reduction* in the spanwise rib-spacing scale has occurred. In particular, in figure 61(d) *three* pairs of roughly equal-spaced, roughly equal-strength counterrotating rib vortices are apparent where only one was present initially. This is a result of the ribs alternating in sign in the streamwise direction, as discussed above.

Similar to the case KINK1P described in section 9.1, a pairing, bulging case (BULG1P) was simulated. Again, because $A_{\frac{1}{2}0}$ is initially small, the pairing is delayed, and the flow changes very little until after τ_r ($A_{\frac{1}{2}0} > A_{10}$ for $t > 15.6$).

The evolutions of Γ_x^{MP1}, the value of Γ_x in the mid-braid region located at $x = 0$ (left boundary in fig. 59), and Γ_x^{MP2}, the mid-braid region located at $x = \lambda_x$ (the center of fig. 59), are shown in figure 60 for BULG1P. Until $\tau_r = 10.2$, the evolutions are similar to those of BULG0P. As expected, the pairing disturbance breaks the symmetry that ensures that $\Gamma_x^{\mathrm{MP1}} = -\Gamma_x^{\mathrm{MP2}}$. Because the pairing brings the two rollers closer together, reentry of vorticity into MP2 occurs sooner than (and reentry into MP1 occurs later than) in BULG0P. For the same reason, Γ_x^{MP1} and Γ_x^{MP2} decrease in magnitude later and earlier, respectively, compared to BULG0P. At later times Γ_x^{MP2} is in the core of the paired roller (no longer an MP); its behavior is irregular. The second change in sign of Γ_x^{MP1} is also delayed by the pairing.

Unlike in KINK1P, the paired roller in BULG1P does not resemble a two-dimensional paired roller. In fact, the BP ω_z contours at about $\tau_{p1} = 24.2$ are qualitatively similar to those of HIGH1P at τ_{p1} (compare fig. 62(a) with fig. 62(c)). Thus, even with the initial disturbances considered here, pairing in

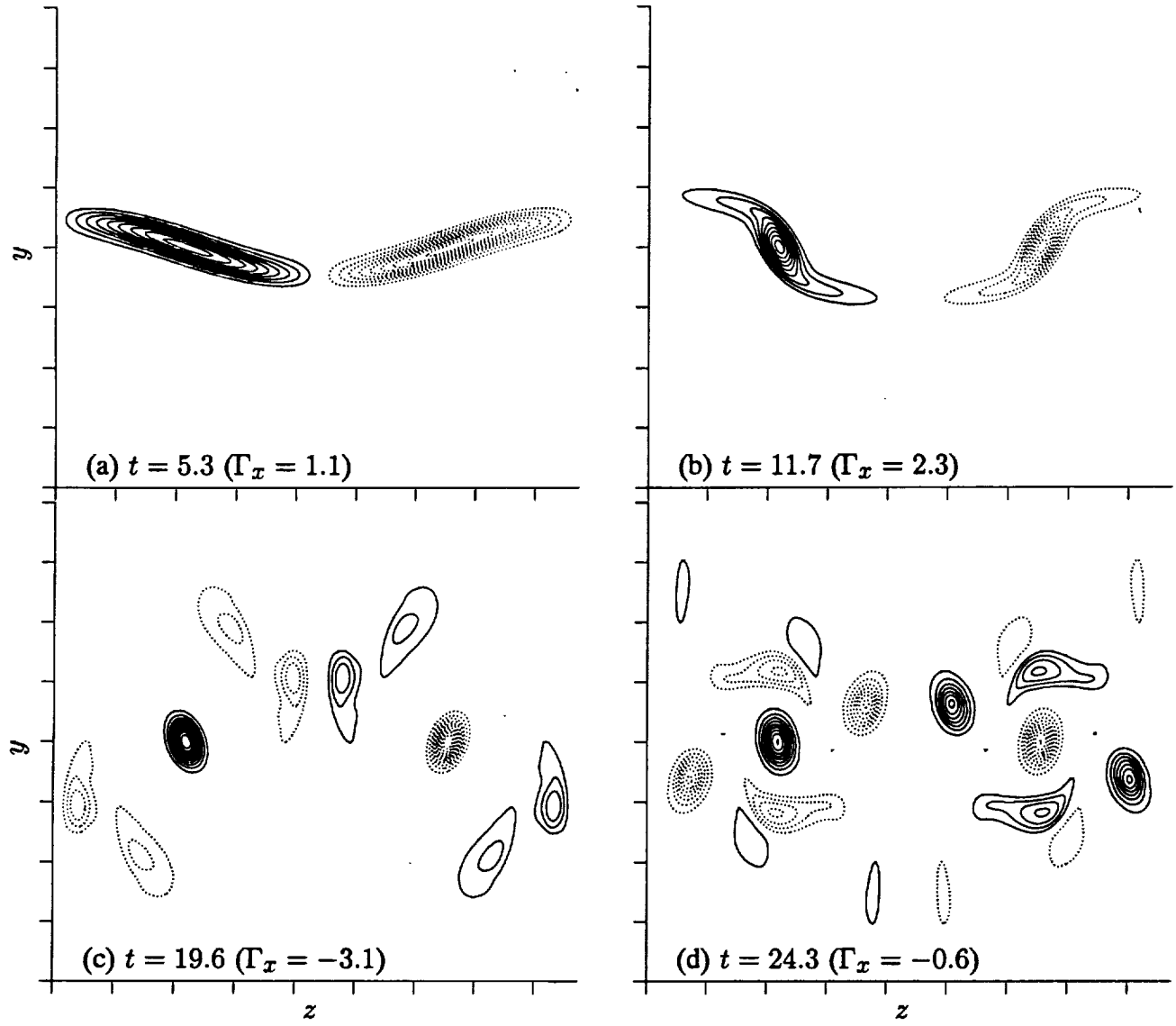

Figure 61. Contours of ω_x in the $x = 0$ MP of BULG0P. The contour increments are (a) ± 0.1, (b) ± 0.4,and (c,d) ± 0.8. Dotted contours indicate negative vorticity and tic marks are at δ_ω^0 intervals.

a flow with collapsed ribs can trigger transition. It should also be noted that the pairing has suppressed the formation of the second "hoop" structure observed in figure 59(f) and, to a large extent, the spanwise scale reduction (fig. 61).

The spanwise scale reduction observed in figure 61 suggests that initial disturbances with smaller spanwise wavelengths might be more unstable. To verify this, two more "bulging"-phased simulations were made (NBULG0P and NBULG1P), with the bulk of the three-dimensional energy placed in the $(\frac{1}{2}, \pm 1)$ modes, that is, in modes with half the spanwise wavelength of the cases described above. This results in two pairs of rib vortices in the computational domain. A smaller amount of energy was also put into the $(\frac{1}{2}, \pm\frac{1}{2})$ modes to create ribs of unequal strength (breaking the symmetry between the rib pairs). It should be noted that the presence of these two oblique subharmonic modes makes energy transfer into the two-dimensional subharmonic possible through nonlinear interactions. Nevertheless,

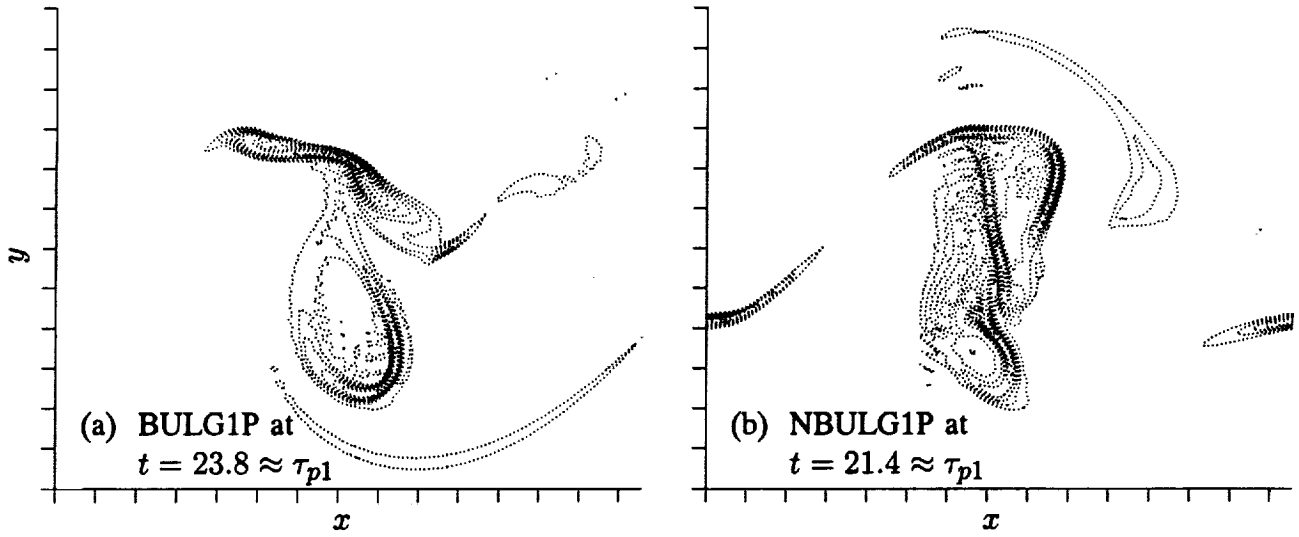

Figure 62. Contours of ω_z. The contour increments are (a) -0.5 and (b) -0.4. Tic marks are at δ_ω^0 intervals.

$A_{\frac{1}{2}0}$ is over an order of magnitude smaller than A_{10} and $A_{\frac{1}{2}1}$ throughout the evolution of NBULG0P, and pairing does not occur.

The evolution of these two flows is similar to the other "bulging"-phased cases described above. Sustained ribs (of unequal strength and therefore with different collapse times) form, and their sign alternates between successive rollers. They are first oblique and later S-shaped. The roller core again contains both signs of ω_x, and because of this, "hoops" develop. In these flows twice as many hoops form in the domain because of the reduced spanwise rib spacing (fig. 63). Details of the flow evolution, such as the timing of the hoops' appearance and collapse and the peak vorticity levels attained, are slightly different for these narrow rib-spacing cases. Despite this, NBULG1P (fig. 62(b)) qualitatively resembles BULG1P (fig. 62(a)) as well as the transitional cases of section 5.2.

10 SUMMARY AND DISCUSSION

The simulations described in the previous sections provide a detailed description of three-dimensional mixing layers undergoing pairings of the primary Kelvin-Helmholtz rollers and, in some cases, transition to turbulence. The early time evolution through the first Kelvin-Helmholtz roll-up was described in Part 1 (summarized here in the Appendix). In this section, the effects of pairing on three-dimensional mixing layers are summarized, and the results are compared with conclusions reached in earlier studies.

10.1 Pairing and Transition

Several important features of the evolution of three-dimensional mixing layers are governed by the development of the two-dimensional Kelvin-Helmholtz rollers and can therefore be understood in the context of a two-dimensional flow with a three-dimensional small disturbance. As pairing proceeds, two rollers corotate and eventually amalgamate into a larger, paired roller. During a pairing, the braid

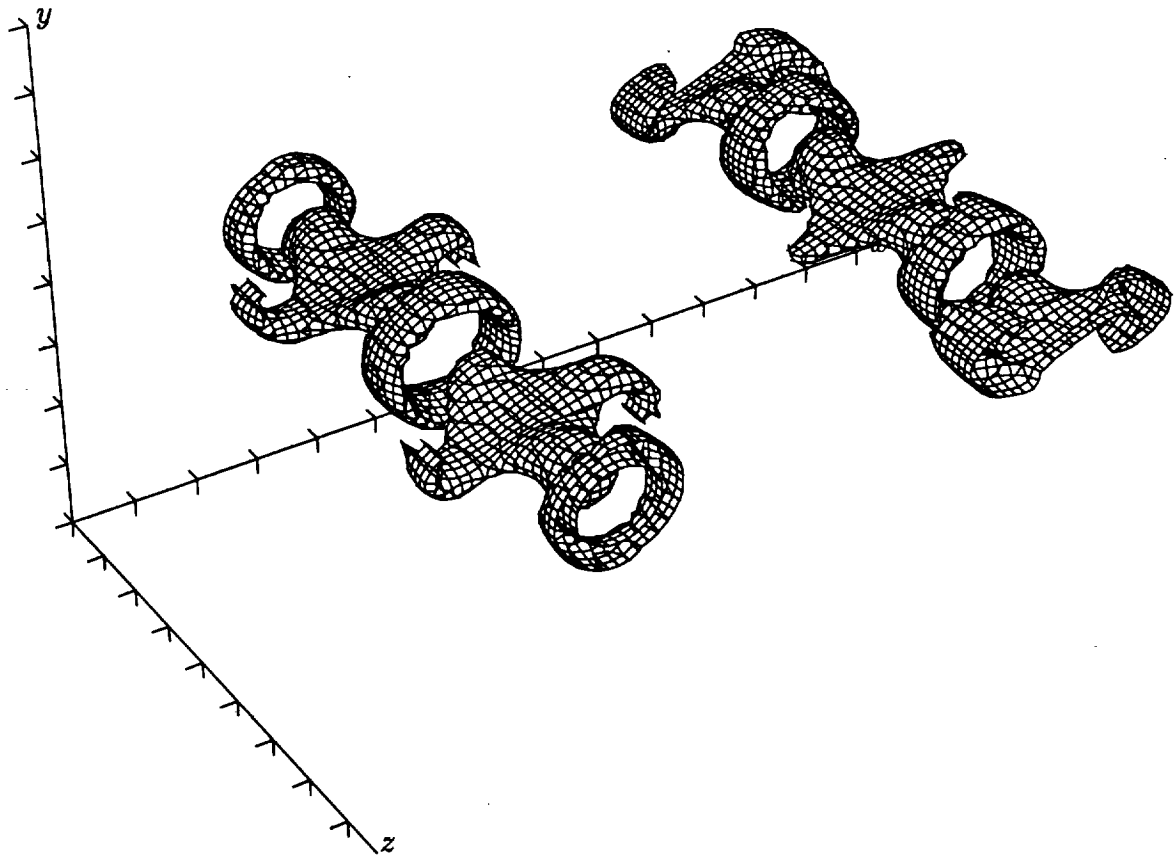

Figure 63. Surface of constant spanwise vorticity ($\omega_z = -2.0$) at $t = 11.6$ in NBULG0P (NBULG1P is very similar at this time). Tic marks are at δ_ω^0 intervals.

region between the pairing rollers (including the rib vortices in three-dimensional flows) is engulfed. The braid region on the other side of each roller survives and becomes a braid region between the paired rollers. By pulling the rollers away from the surviving braid region, pairing (if initiated soon enough) prevents "oversaturation" (described in Part 1) and the associated reentry of spanwise vorticity into the surviving braid region. Pairing therefore prevents (or delays) the rapid, apparently exponential, growth of three-dimensionality associated with oversaturation. As the two rollers are drawn together and begin to coalesce, spiral arms of vorticity are ejected from the paired roller. These spiral arms reenter the surviving braid region shortly after the pairing is completed. This reentry of vorticity results in a period of rapid growth of three-dimensionality, which is arrested as the spanwise vorticity is again drawn out of the braid region. Unlike oversaturation, the reentry of spanwise vorticity associated with the spiral arms cannot be suppressed by further pairings. Thus, after each pairing there is a period of three-dimensionality growth that results in an increase in three-dimensionality by an approximately constant factor for each pairing (see section 4.1). Once pairings have ceased, the final paired roller eventually oversaturates, as described in Part 1, with a resulting exponential growth of three-dimensionality.

The prevention of oversaturation by pairing is the reason that pairing inhibits the growth of three-dimensionality (Metcalfe et al., 1987; Huang and Ho, 1990). Oversaturation results in spanwise vorticity entering the braid region and remaining there. Three-dimensional perturbations then grow continuously. In contrast, continued pairings result in discrete periods of growth of three-dimensionality as each pairing throws spanwise vorticity into the surviving braid region. The time between pairings, and

therefore the time between these periods of growth, approximately doubles with each pairing. This results in algebraic long-term growth of three-dimensionality rather than the exponential growth that occurs during oversaturation.

If pairing is not initiated fast enough, oversaturation and its associated exponential growth of three-dimensionality can occur prior to the pairing. Because the growth of three-dimensionality during and after the pairing is similar for all pairings, delayed pairing results in more three-dimensionality. This is relevant to forced experimental mixing layers because forcing tends to suppress pairing.

The results of Part 1 suggested that the translative instability responsible for the growth of three-dimensionality in an oversaturated mixing layer is not associated with an isolated portion of the flow (i.e., braid region or core), since it produces continuous growth of both rib circulation and roller kinking. The growth of three-dimensionality in a mixing layer prior to oversaturation is also not limited to a particular region of the flow. This was determined by examining the evolution of three-dimensional perturbations through several pairings. The period of three-dimensionality growth that occurs after each pairing is initiated by the entry of the spiral arms of spanwise vorticity into the braid region. This allows the rib vortices to suddenly increase their circulation. Later, as the next pairing begins, the level of three-dimensionality in the core also grows. Finally, as the next pairing nears completion, the three-dimensional disturbances come into a rough equilibrium until the next spiral arms initiate another period of growth. Clearly, both the braid regions and the roller cores are involved in the growth of three-dimensionality, and the instability must be considered to be one of the flow as a whole.

It is also interesting to note that it is apparently impossible for a two-dimensional mixing layer to undergo a sequence of self-similar pairings (i.e., a pairing in which the paired roller is similar to the original unpaired rollers). At high Reynolds numbers, vorticity does not diffuse fast enough to maintain a self-similar configuration. Thus, with each pairing the region of vorticity concentration in the roller gets smaller relative to the distance between rollers.

Pairing in a weakly three-dimensional mixing layer is well described by the linear evolution of a three-dimensional perturbation, as discussed above. However, pairing in more strongly three-dimensional layers results in significant nonlinearities and, in some cases, the beginnings of the transition to turbulence. In section 5 the details of the initial portion of such a transition are described. In this case transition is triggered by a pairing in a flow that is significantly three-dimensional (i.e., contains strong "cups" and collapsed "ribs"), although still organized into a few large-scale structures. By the time the pairing is complete, the layer has become disorganized and the origins of many vortical structures can no longer be traced back to their organized prepairing counterparts. After the pairing, vortex stretching increases the complexity of the flow. Remnants of the original rib vortices, together with newly created vortices in the core, generate thin vortex sheets; these sheets are unstable and undergo higher-order roll-ups, further increasing the complexity of the flow by generating small scales.

When the transitioning flow described above undergoes a further pairing, an apparently fully turbulent mixing layer results. Such flows bear a strong resemblance to experimental turbulent mixing layers and show many characteristics of turbulent flows in general (see section 8). The level of the mixedness, parameter $\mathcal{M}$ (defined in eq. (19)), in these flows is about 0.18 higher than the corresponding level in flows that have not undergone transition. This increase is similar to the increase in mixedness observed experimentally (Konrad, 1976).

The pairing-induced transition described in section 5 has many characteristics in common with experimentally observed transition. The experiments of Huang and Ho (1990) also indicated that the timing of the transition was related to the occurrence of pairings and that the flow was fully turbulent by the completion of the second pairing. The small scales in their flow were found to first appear predominantly in the roller core at spanwise locations where ribs were located. This is consistent with the results presented here, which show significantly more small-scale structure in the roller core portion of the rib plane than elsewhere in the flow (fig. 41).

Other possible transition mechanisms (besides the pairing-induced one considered above) also exist. In particular, a few simulations described here and in Part 1 that do not undergo any pairings appear to be transitional. In such flows, transition results from either extremely large initial three-dimensional disturbances or from a long development in the oversaturated state. In the HIROLL flow of Part 1, the initial three-dimensional disturbance strength was four times that of the baseline ROLLUP case in Part 1 and of the HIGH1P simulation here (note that these flows have structures similar to those observed in experiments). This initial level of three-dimensionality is so high that significant nonlinear behavior results before the roll-up is complete. By the time the flow reaches oversaturation, it is apparently turbulent (Part 1, fig. 22), with thin vortex sheets undergoing higher-order roll-ups in the BP and with small-scale granular vorticity structures in the RP.

Transition, perhaps of a different character, can also result from long flow development in the oversaturated state. The PH$\frac{\pi}{4}$0P flow does not undergo any pairings, is begun from three-dimensional disturbances of only moderate strength, and yet is also apparently turbulent by $t = 30.0$ (fig. 49). In this flow, it is difficult to examine BP's for thin vortex sheets and higher-order roll-ups and RP's for small-scale granular vorticity structures, because the presence of spanwise subharmonics in this flow makes the BP's and RP's poorly defined (this is also the case for the TURB2P flow). For the strengths and relative phasings of the spanwise subharmonics used in this flow, the ribs move considerably from their initial locations in both the spanwise and cross-stream directions.

The flows described above all contain collapsed rib vortices prior to transition. The OBLOUT flow of Part 1 does not develop sustained collapsed ribs and therefore must become turbulent in a different manner or remain organized. Interestingly, vortex stretching does produce thin vortex sheets that undergo higher-order roll-ups in this flow. Even so, the flow is still largely organized as the flow oversaturates, and the three-dimensional amplitude A_{3D} is still much less than that of the two-dimensional modes A_{s0}. If transition is to occur in this flow, it seems that further development (past $t = 20.0$) in the oversaturated state is necessary.

10.2 Spanwise Scale Change

There has been some controversy regarding the evolution of the characteristic spanwise scale in mixing layers. From flow visualizations, Bernal and Roshko (1986) concluded that the initial "streak" (rib) spacing was formed by the first pairing and that this characteristic spanwise spacing was maintained through one or two additional pairings until the end of the mixing transition, when it increased. The rib locations also became uncoupled from the locations of the initial ribs at this point (these initial locations being determined by imperfections on, or upstream of, the splitter plate). In contrast to this, Huang and Ho (1990) determined that the dominant spanwise scale in their mixing layers doubled with each

pairing in a self-similar manner. This was determined by applying a maximum-entropy technique to spanwise profiles of the mean streamwise velocity and by taking the spanwise scale to be the location of the peak in the maximum-entropy spectra.

The results presented in this paper indicate that a doubling of the spanwise length scale does not occur after each pairing. In fact, in the limit of weak three-dimensional disturbances (where the linear analysis of section 4.2 applies), a doubling does not occur until after three or four pairings. This is not surprising since the two-dimensional base flow does not evolve self-similarly. As the magnitude of the three-dimensional disturbance is increased, however, scale change can proceed more rapidly.

In many of the flows considered here, the spacing of the rib vortices up to and beyond the first pairing is determined largely by the initial condition. When the ribs are nearly equally spaced and of nearly equal strength, their net induced motion on each other is small. It is thus not surprising that such flows exhibit little tendency to change spanwise scale. By using more irregular initial vorticity distributions, more significant changes in the rib locations can be realized (fig. 47). Such flows may appear to have a larger characteristic spanwise scale than in the initial condition, although the same number of rib vortices are present in the domain. At the Reynolds numbers considered here, viscous diffusion does not act fast enough to reduce the number of ribs in the domain.

The reentry of vorticity into the braid region (either during oversaturation or from the spiral arms) can also play an important role in the scale-change process. It provides a means to augment or reduce different rib circulations by different amounts. This greater variability in rib strength can, in turn, lead to greater net induced rib motion and apparent scale change. This process is illustrated in figure 48. Vorticity enters the braid region away from the centerline, "recollapses" into the existing rib vortices owing to the compressive component of the two-dimensional strain field, and results in stronger ribs in a more irregular pattern. This process repeats with the reentry of the spiral arms associated with the second pairing, although the recollapse process is much more disorganized.

In transitional flows, reentry of vorticity into the braid region results in complicated mid-braid vorticity distributions, and it is then difficult to define rib locations (these ribs may be quite different from their organized pretransition counterparts). Defining a characteristic spanwise scale can be difficult in these cases. Here we define Λ_z to be the spanwise wavelength associated with the Fourier amplitude $A_{s\beta}$ that is the largest. By this definition, the PH$\frac{\pi}{4}$0P flow undergoes a doubling of Λ_z at $t = 28.9$. Indeed, at $t = 30.0$, a mid-braid plane cut reveals one dominant structure (fig. 49). This structure, however, is not a single pair of organized ribs with twice the spacing of the initial rib vortex pairs, but rather an apparently turbulent blob of small-scale vortices.

Instead of using the Fourier amplitude $A_{s\beta}$ to define Λ_z, we could have used the amplitude $A_{0\beta}$. This definition more closely mimics the scale-change diagnostic of Huang and Ho (1990), who examined the time-averaged streamwise velocity as a function of z. Using this scale change measure, scale changes occur later than by the previous definition, especially for transitional cases. For example, for TURB2P the spanwise scale would double at $t = 49.1$ rather than quadruple at $\tau_{sc} = 32.0$. There is less difference in nontransitional cases (e.g., scale change at $t = 67.6$ versus 61.0 in WMID2P).

The search for a mechanism whereby organized ribs and rollers become organized ribs and rollers with twice the original streamwise and spanwise spacings after a pairing appears to be fruitless. Presumably such a process does not occur in mixing layers. Weak ribs remain close to their initial locations and do not change scale, and strong ribs lead to transition, resulting in a "statistical" scale change with disorganized structure. Even when the ribs are of intermediate strength, it does not appear that their number can be reduced prior to transition. Possible mechanisms for such a reduction identified in section 7.2 ultimately rely on viscous annihilation, a process that is slow at the Reynolds numbers considered here.

Several factors must be considered when comparing the results presented here with those of experiments. In flow-visualization experiments, it is not always clear that the visualization method is actually portraying the vorticity. Vortical structures may not always be well defined by their footprint in dye or smoke. In turbulent flows, the "streak spacing" observed in flow visualizations is probably not associated with organized rib vortices like those in pretransitional flows. In addition, even the more irregular initial streamwise vorticity distributions used here are probably more organized than those in most experiments. In particular, the initial conditions used here, even when strong spanwise subharmonics were used, all contained disturbances that were strongest at the domain centerline and that alternated in sign in the spanwise direction. Experiments have suggested the amalgamation of like-sign rib vortices prior to the development of a "stable configuration" consisting of pairs of opposite-sign rib vortices, e.g., Lasheras, Cho, and Maxworthy (1986); Bell and Mehta (1989). In addition, the contour-dynamics calculations of Pullin and Jacobs (1986) indicate that, at high Reynolds numbers, it is possible for a "wide" region of streamwise vorticity to collapse into several like-sign rib vortices, these vortices later undergoing their own pairing (see also Jacobs and Pullin, 1989). Thus apparent scale changes in experimental flow visualization may be different from the type discussed here.

In conclusion, the results presented here do not support the conclusion that scale changes are locked to pairings of the spanwise rollers; the ratio between the spanwise and streamwise length scales does not remain constant. In fact, the data of Huang and Ho (1990) do not provide completely convincing support for this conclusion either. First, they have observed this behavior through only two pairings of the spanwise rollers. Second, the doubling of the spanwise length scale after the first pairing is questionable in their data. The maximum-entropy spectrum in their figure 9(b) (first pairing) does indeed peak at twice the wavelength of the same quantity in their figure 9(a) (post roll-up); but, as they note, the peak at the original spacing is almost as large. In addition, this scale change is not really visible in their spanwise profiles of streamwise velocity at the first pairing. The spanwise profiles of streamwise velocity in their figure 5(a) *do* seem to indicate a quadrupling of the spanwise scale after the second pairing. However, since transition is largely completed by their second pairing, this observation is consistent with the current results and those of Bernal and Roshko (1986).

10.3 Helical Pairing

Pierrehumbert and Widnall (1982) have proposed that "helical" pairing, suggested by the experimental work of Chandrsuda et al. (1978), may be the result of oblique subharmonic disturbances. Such disturbances would tend to kink the Kelvin-Helmholtz rollers such that part of each roller would be closer to its downstream neighbor, while other portions would be closer to the roller upstream.

Pierrehumbert and Widnall felt that this configuration could lead to localized pairing at locations where the rollers were close, resulting in an apparently helical pattern.

The results presented in section 9.1 indicate that the presence of oblique subharmonic modes is not, by itself, enough to ensure localized pairing of the Kelvin-Helmholtz rollers, at least for the spanwise wavelengths considered here. It does result in kinked Kelvin-Helmholtz rollers, but these rollers do not pair at any spanwise location. The addition of a weak two-dimensional subharmonic disturbance leads to eventual pairing of the same two rollers along their entire span, but not to localized pairing. Similar results were obtained by Sandham and Reynolds (1989) for a compressible mixing layer. It appears that the disorganized mixing layer studied by Chandrsuda et al. (1978) may have been the result of inlet disturbances more complicated than a single pair of oblique subharmonic modes.

APPENDIX

RESULTS FROM PART 1

The presentation of many of the results in this paper assumes familiarity with the evolution of three-dimensional Kelvin-Helmholtz roll-ups as presented in Part 1. Here a summary of the results of Part 1 is presented. This summary includes both a brief description of the vortical structures that develop as the layer rolls up and definitions of terms and quantities given in Part 1 that are used in Part 2.

In Part 1 a "typical" roll-up evolution that resulted from the standard set of initial conditions used here (see section 2.2), as well as many other initial conditions, was identified. The typical Kelvin-Helmholtz roll-up produces the well-known spanwise vortices (rollers) and the familiar array of predominately streamwise rib vortices (ribs) that extend from below one roller to above its downstream neighbor. The rib vortices alternate in sign in the spanwise direction and are roughly aligned with the extensional strain in the region between the rollers (the braid region). The ribs are formed from vortex lines that are kinked in the streamwise direction and become stretched by the extensional strain in the braid region. In the core of the rollers, vortex lines become kinked in the opposite direction, resulting in streamwise vorticity with sign opposite that in the rib at the same spanwise location. The ribs and the oppositely signed streamwise vorticity in the roller produce a strain where the ribs pass over the top (or under the bottom) of the roller. This strain alternately (in the spanwise direction) stretches and compresses the spanwise vorticity at the top and bottom of the roller. This results in cup-shaped regions (cups) of intense spanwise vorticity in the roller, these cups being located between the rib vortices and alternating from the top to the bottom of the roller in the span (see fig. 10 of Part 1). The experiments of Nygaard and Glezer (1991) suggest that similar structures occur in experimental mixing layers. On the opposite side of the roller from each cup is a "wisp" of weaker spanwise vorticity (see fig. 15 of Part 1). This wisp contains the vortex lines that loop from one rib to its neighbor.

To a large extent, the strength of the cups and the degree of three-dimensionality in the mixing layer can be determined from the strength of the ribs. The best measure of rib strength is rib circulation, here denoted by Γ_x. It is defined as

$$\Gamma_x = \int_{y=-\infty}^{\infty} \int_{z=0}^{\lambda_z/2} \omega_x \, dz dy = - \int_{y=-\infty}^{\infty} v \, dy \Big|_{z=0}^{\lambda_z/2} \tag{A-1}$$

where $z = 0$ is taken to be one of the planes of symmetry defined in equation (12), that is, a BP (between-ribs plane). Throughout this paper the rib circulation is measured at x-locations corresponding to the MP (midbraid plane).[22] A superscript 0 and $*$ will be used to denote, respectively, the circulation at $t = 0$ and the circulation normalized by its value at $t = 0$. By manipulating the Navier-Stokes equations, the governing equation for Γ_x can be obtained (for simplicity, the inviscid case is considered here):

$$\frac{\partial \Gamma_x}{\partial t} = \int_{y=-\infty}^{\infty} (u\omega_z) \, dy \Big|_{z=0}^{\lambda_z/2} = \int_{y=-\infty}^{\infty} (u \frac{\partial v}{\partial x}) \, dy \Big|_{z=0}^{\lambda_z/2} \tag{A-2}$$

Equation (A-2) implies that there must be spanwise vorticity in the MP for Γ_x to grow. Indeed, in Part 1 it was observed that the rib circulation stopped growing as the spanwise vorticity was drawn out

[22] Γ_x^{MP} was used to denote the MP circulation in Part 1.

of the braid region by the forming roller. It was then precluded from further growth until some event (oversaturation in Part 1) brought spanwise vorticity back into the MP. This is of great importance in the pairing of three-dimensional mixing layers (see section 4).

The rib circulation is also important in determining whether the ribs collapse into compact, nearly axisymmetric vortices as described by Lin and Corcos (1984). In Part 1 it was found that the Lin and Corcos criterion was an accurate predictor of rib collapse in the mixing layer. A collapse parameter $\mathcal{L}$ was defined based on a curve fit to the curve in figure 9 of Lin and Corcos, resulting in the collapse criterion:

$$\mathcal{L} = \frac{\Gamma_x}{\nu^p (S\lambda_z^2)^{1-p}} > 13.1 \qquad \text{(A-3)}$$

where $p = 0.6825$ is the curve fit parameter and S is the maximum two-dimensional (i.e., averaged in z) principal strain rate in the MP. Collapse of the ribs is a nonlinear phenomenon, and it was shown in Part 1 to be one of the first three-dimensional nonlinearities to occur. It was also found that rib collapse was a prerequisite for the formation of strong cups, as described above.[23]

Finally, two further definitions from Part 1 are given here. One is that of the momentum thickness (δ_m) defined by

$$\delta_m = \frac{1}{4}\int_{-\infty}^{\infty}(1-\overline{U}^2)dy \qquad \text{(A-4)}$$

The other is that of the mid-braid vorticity ($-\omega_b$). For mixing layers with negative mean vorticity (like those considered here), ω_b is the minimum (most negative) of the spanwise-averaged spanwise vorticity in the MP. The mid-braid vorticity is an indicator of the amount of spanwise vorticity in the braid region and is a necessary ingredient for rib circulation growth, as mentioned above.

[23]Though cup formation is nonlinear, the mechanism leading to the strain that produces the cups is linear with respect to the two-dimensional evolving base flow (see section 5.3 of Part 1).

REFERENCES

Bell, J. H.; and Mehta, R. D.: Three-Dimensional Structure of a Plane Mixing Layer. AIAA Paper 89-0124, 1989.

Bernal, L. P.: The Coherent Structure of Turbulent Mixing Layers. Ph.D. Thesis, California Institute of Technology, 1981.

Bernal, L. P.; and Roshko, A.: Streamwise Vortex Structure in Plane Mixing Layers. J. Fluid Mech., vol. 170, 1986, pp. 499–525.

Breidenthal, R.: Response of Plane Shear Layers and Wakes to Strong Three-Dimensional Disturbances. Phys. Fluids, vol. 23, 1980, pp. 1929–1934.

Breidenthal, R.: Structure in Turbulent Mixing Layers and Wakes Using a Chemical Reaction. J. Fluid Mech., vol. 109, 1981, pp. 1–24.

Brown, G. L.; and Roshko, A.: The Effect of Density Difference on the Turbulent Mixing Layer. Turbulent Shear Flows, AGARD Conf. Proc., vol. 93, 1971, pp. 23-1–23-11.

Brown, G. L.; and Roshko, A.: On Density Effects and Large Structure in Turbulent Mixing layers. J. Fluid Mech., vol. 64, 1974, pp. 775–816.

Buell, J. C.; and Huerre, P.: Inflow/Outflow Boundary Conditions and Global Dynamics of Spatial Mixing Layers. Proc. 1988 Summer Program, Center for Turbulence Research, CTR-S88, Stanford, CA, 1988.

Buell, J. C.; and Mansour, N. N.: Asymmetric Effects in Three-Dimensional Spatially Developing Mixing Layers. Proc. Seventh Intl. Symp. on Turbulent Shear Flows, Stanford University, Stanford, CA, 1989, pp. 9.2.1–9.2.6.

Burke, S. P.; and Schumann, T. E. W.: Diffusion Flames. Ind. Eng. Chem., vol. 20, 1928, pp. 998–1004.

Chandrsuda, C.; Mehta, R. D.; Weir, A. D.; and Bradshaw, P.: Effect of Free-Stream Turbulence on Large Structure in Turbulent Mixing Layers. J. Fluid Mech., vol. 85, 1978, pp. 693–704.

Corcos, G. M.; and Lin, S. J.: The Mixing Layer: Deterministic Models of a Turbulent Flow. Part 2. The Origin of the Three-Dimensional Motion. J. Fluid Mech., vol. 139, 1984, pp. 67–95.

Dimotakis, P. E.; and Brown, G. L.: The Mixing Layer at High Reynolds Number: Large-Structure Dynamics and Entrainment. J. Fluid Mech., vol. 78, 1976, pp. 535–560.

Hernan, M. A.; and Jimenez, J.: Computer Analysis of a High-Speed Film of the Plane Turbulent Mixing Layer. J. Fluid Mech., vol. 119, 1982, pp. 323–345.

Ho, C.-M.; and Huang, L.-S.: Subharmonics and Vortex Merging in Mixing Layers. J. Fluid Mech., vol. 119, 1982, pp. 443–473.

Huang, L.-S.; and Ho, C.-M.: Small-Scale Transition in a Plane Mixing Layer. J. Fluid Mech., vol. 210, 1990, pp. 475–500.

Jacobs, P. A.; and Pullin, D. I.: Multiple-Contour-Dynamic Simulation of Eddy Scales in the Plane Shear Layer. J. Fluid Mech., vol. 199, 1989, pp. 89–124.

Jimenez, J.: A Spanwise Structure in the Plane Shear Layer. J. Fluid Mech., vol. 132, 1983, pp. 319–336.

Jimenez, J.; Cogollos, M.; and Bernal, L. P.: A Perspective View of the Plane Mixing Layer. J. Fluid Mech., vol. 152, 1985, pp. 125–143.

Konrad, J. H.: An Experimental Investigation of Mixing in Two-Dimensional Turbulent Shear Flows with Applications to Diffusion-Limited Chemical Reactions. Intern. Rep. CIT-8-PU, Calif. Inst. Technol., Pasadena, CA, 1976.

Koochesfahani, M. M.; and Dimotakis, P. E.: Mixing and Chemical Reactions in a Turbulent Liquid Mixing Layer. J. Fluid Mech., vol. 170, 1986, pp. 83–112.

Lasheras, J. C.; Cho, J. S.; and Maxworthy, T.: On the Origin and Evolution of Streamwise Vortical Structures in a Plane, Free Shear Layer. J. Fluid Mech., vol. 172, 1986, pp. 231–258.

Lasheras, J. C.; and Choi, H.: Three-Dimensional Instability of a Plane Free Shear Layer: an Experimental Study of the Formation and Evolution of Streamwise Vortices. J. Fluid Mech., vol. 189, 1988, pp. 53–86.

Lele, S. K.: Direct Numerical Simulation of Compressible Free Shear Flows. AIAA Paper 89-0374, 1989.

Lin, S. J.; and Corcos, G. M.: The Mixing Layer: Deterministic Models of a Turbulent Flow. Part 3. The Effect of Plane Strain on the Dynamics of Streamwise Vortices. J. Fluid Mech., vol. 141, 1984, pp. 139–178.

Lowery, P. S.; and Reynolds, W. C.: Numerical Simulation of a Spatially-Developing, Forced, Plane Mixing Layer. Dept. Mech. Engng. Rep. TF-26. Stanford University, Stanford, CA, 1986.

Martel, C.; Mora, E.; and Jimenez, J.: Small Scales Generation in 2-D Mixing Layers. Bull. Amer. Phys. Soc., vol. 34, 1989, p. 2268.

Metcalfe, R. W.; Orszag, S. A.; Brachet, M. E.; Menon, S.; and Riley, J. J.: Secondary Instability of a Temporally Growing Mixing Layer. J. Fluid Mech., vol. 184, 1987, pp. 207–243.

Monkewitz, P. A.: Subharmonic Resonance, Pairing and Shredding in the Mixing Layer. J. Fluid Mech., vol. 188, 1988, pp. 223–252.

Monkewitz, P. A.; and Huerre, P.: Influence of the Velocity Ratio on the Spatial Instability of Mixing Layers. Phys. Fluids, vol. 25, 1982, pp. 1137–1143.

Moore, D. W.; and Saffman, P. G.: The Density of Organized Vortices in a Turbulent Mixing Layer. J. Fluid Mech., vol. 69, 1975, pp. 465–473.

Moser, R. D.; and Rogers, M. M.: Mixing Transition and the Cascade to Small Scales in a Plane Mixing Layer. Phys. Fluids A, vol. 3, 1991, pp. 1128–1134.

Nygaard, K. J.; and Glezer, A.: Evolution of Streamwise Vortices and Generation of Small-Scale Motion in a Plane Mixing Layer. J. Fluid Mech., vol. 231, 1991, pp. 257–301.

Oster, D.; and Wygnanski, I.: The Forced Mixing Layer Between Parallel Streams. J. Fluid Mech., vol. 123, 1982, pp. 91–130.

Pierrehumbert, R. T.; and Widnall, S. E.: The Two- and Three-dimensional Instabilities of a Spatially Periodic Shear Layer. J. Fluid Mech., vol. 114, 1982, pp. 59–82.

Pullin, D. I.; and Jacobs, P. A.: Inviscid Evolution of Stretched Vortex Arrays. J. Fluid Mech., vol. 171, 1986, pp. 377–406.

Riley, J. J.; and Metcalfe R. W.: Direct Numerical Simulation of a Perturbed Turbulent Mixing Layer. AIAA Paper 80-0274, 1980.

Rogers, M. M.; and Moser, R. D.: The Three-Dimensional Evolution of a Plane Mixing Layer. Part 1. The Kelvin-Helmholtz Roll-Up. NASA TM-103856, 1991.

Rogers, M. M.; and Moser, R. D.: The Three-Dimensional Evolution of a Plane Mixing Layer: The Kelvin-Helmholtz Roll-Up. J. Fluid Mech., vol. 243, 1992, pp. 183–226.

Sandham, N. D.; and Reynolds, W. C.: A Numerical Investigation of the Compressible Mixing Layer. Dept. Mech. Engng. Rep. TF-45, Stanford University, Stanford, CA, 1989.

Spalart, P. R.; Moser, R. D.; and Rogers, M. M.: Spectral Methods for the Navier-Stokes Equations with One Infinite and Two Periodic Directions. J. Comp. Phys., vol. 96, 1991, pp. 297–324.

Stuart, J. T.: On Finite Amplitude Oscillations in Laminar Mixing Layers. J. Fluid Mech., vol. 29, 1967, pp. 417–440.

Thorpe, S. A.: A Method of Producing a Shear Flow in a Stratified Fluid. J. Fluid Mech., vol. 32, 1968, pp. 693–704.

Thorpe, S. A.: Experiments on the Instability of Stratified Shear Flows: Miscible Fluids. J. Fluid Mech., vol. 46, 1971, pp. 299–319.

Thorpe, S. A.: Experiments on Instability and Turbulence in a Stratified Shear Flow. J. Fluid Mech., vol. 61, 1973, pp. 731–751.

Thorpe, S. A.: Laboratory Observations of Secondary Structures in Kelvin-Helmholtz Billows and Consequences for Ocean Mixing. Geophys. Astrophys. Fluid Dynamics, vol. 34, 1985, pp. 175–199.

Toor, H. L.: Mass Transfer in Dilute Turbulent and Non-Turbulent Systems with Rapid Irreversible Reactions and Equal Diffusivities. A.I.Ch.E. Journal, vol. 8, 1962, pp. 70–78.

Turner, J. S.: Buoyancy Effects in Fluids. Cambridge University Press, 1973.

Winant, C. D.; and Browand, F. K.: Vortex Pairing: The Mechanism of Turbulent Mixing-Layer Growth at Moderate Reynolds Number. J. Fluid Mech., vol. 63, 1974, pp. 237–255.

Wygnanski, I.; Oster, D.; Fiedler, H.; and Dziomba, B.: On the Perseverance of a Quasi-Two-Dimensional Eddy-Structure in a Turbulent Mixing Layer. J. Fluid Mech., vol. 93, 1979, pp. 325–335.

Yang, Z.; and Karlsson, S. K. F.: Evolution of Coherent Structures in a Plane Shear Layer. Phys. Fluids A, vol. 3, 1991, pp. 2207-2219.

Zeldovich, Y. B.: On the Theory of Combustion of Initially Unmixed Gases. NACA TM-1296, 1951.

REPORT DOCUMENTATION PAGE

Form Approved
OMB No. 0704-0188

1. AGENCY USE ONLY *(Leave blank)*	2. REPORT DATE	3. REPORT TYPE AND DATES COVERED
	December 1992	Technical Memorandum

4. TITLE AND SUBTITLE

The Three-Dimensional Evolution of a Plane Mixing Layer
Part 2. Pairing and Transition to Turbulence

5. FUNDING NUMBERS

505-59-53

6. AUTHOR(S)

Robert D. Moser and Michael M. Rogers

7. PERFORMING ORGANIZATION NAME(S) AND ADDRESS(ES)

Ames Research Center
Moffett Field, CA 94035-1000

8. PERFORMING ORGANIZATION REPORT NUMBER

A-92068

9. SPONSORING/MONITORING AGENCY NAME(S) AND ADDRESS(ES)

National Aeronautics and Space Administration
Washington, DC 20546-0001

10. SPONSORING/MONITORING AGENCY REPORT NUMBER

NASA TM-103926

11. SUPPLEMENTARY NOTES

Point of Contact: Robert Moser, Ames Research Center, MS 202A-1, Moffett Field, CA 94035-1000, (415) 604-4733

12a. DISTRIBUTION/AVAILABILITY STATEMENT

Unclassified-Unlimited
Subject Category – 34

12b. DISTRIBUTION CODE

13. ABSTRACT *(Maximum 200 words)*

The evolution of three-dimensional temporally evolving plane mixing layers through as many as three pairings has been simulated numerically. Initial conditions for all simulations consisted of a few low-wavenumber disturbances, usually derived from linear stability theory, in addition to the mean velocity. Three-dimensional perturbations were used with amplitudes ranging from infinitesimal to large enough to trigger a rapid transition to turbulence. Pairing is found both to inhibit the growth of infinitesimal three-dimensional disturbances and to trigger the transition to turbulence in highly three-dimensional flows. The mechanisms responsible for the growth of three-dimensionality as well as the initial phases of the transition to turbulence are described. The transition to turbulence is accompanied by the formation of thin sheets of spanwise vorticity, which undergo a secondary rollup. Transition also produces an increase in the degree of scalar mixing, in agreement with experimental observations of mixing transition.

Simulations were also conducted to investigate changes in spanwise length scale that may occur in response to the change in streamwise length scale during a pairing. The linear mechanism for this process was found to be very slow, requiring roughly three pairings to complete a doubling of the spanwise scale. Stronger three-dimensionality can produce more rapid scale changes but is also likely to trigger transition to turbulence. No evidence was found for a change from an organized array of rib vortices at one spanwise scale to a similar array at a larger spanwise scale.

14. SUBJECT TERMS	15. NUMBER OF PAGES
Mixing layers	87
	16. PRICE CODE: A05

17. SECURITY CLASSIFICATION OF REPORT	18. SECURITY CLASSIFICATION OF THIS PAGE	19. SECURITY CLASSIFICATION OF ABSTRACT	20. LIMITATION OF ABSTRACT
Unclassified	Unclassified		